Acceleration of laser-injected electron beams in an electron-beam driven plasma wakefield accelerator

Dissertation

zur Erlangung des Doktorgrades
des Department Physik
der Universität Hamburg

vorgelegt von

Alexander Knetsch

aus Rio de Janeiro

Hamburg
2017

Gutachter der Dissertation:	Prof. Dr. Bernhard Hidding Prof. Dr. Brian Foster
Zusammensetzung der Prüfungskomission:	Prof. Dr. Robin Santra Prof. Dr. Gudrid Moortgat-Pick Prof. Dr. Bernhard Hidding Prof. Dr. Brian Foster Dr. Andreas Meyer
Datum der Disputation:	31.07.17
Vorsitzender des Prüfungsausschusses:	Prof. Dr. Robin Santra
Vorsitzender des Promotionsausschusses:	Prof. Dr. Wolfgang Hansen
Dekan des Fachbereichs Physik:	Prof. Dr. Heinrich Graener

Abstract

Plasma wakefields deliver accelerating fields that are approximately a 100 times higher than those in conventional radiofrequency or even superconducting radiofrequency cavities. This opens a transformative path towards novel, compact and potentially ubiquitous accelerators. These prospects, and the increasing demand for electron accelerator beamtime for various applications in natural, material and life sciences, motivate the research and development on novel plasma-based accelerator concepts. However, these electron beam sources need to be understood and controlled. The focus of this thesis is on electron beam-driven plasma wakefield acceleration (PWFA) and the controlled injection and acceleration of secondary electron bunches in the accelerating wake fields by means of a short-pulse near-infrared laser. Two laser-triggered injection methods are explored. The first one is the *Trojan Horse Injection*, which relies on very good alignment and timing control between electron beam and laser pulse and then promises electron bunches with hitherto unprecedented quality as regards emittance and brightness. The physics of electron injection in the Trojan Horse case is explored with a focus on the final longitudinal bunch length. Then a theoretical and numerical study is presented that examines the physics of Trojan Horse injection when performed in an expanding wake generated by a smooth density down-ramp. The benefits are radically decreased drive-electron bunch requirements and a unique bunch-length control that enables longitudinal electron-bunch shaping. The second laser-triggered injection method is the *Plasma Torch Injection*, which is a versatile, all-optical laser-plasma-based method capable to realize tunable density downramp injection. At the SLAC National Laboratory, the first proof-of-principle was achieved both for Trojan Horse and Plasma Torch injection. Setup details and results are reported in the experimental part of the thesis along with the commissioning of a novel laser-to-electron-beam synchronization diagnostic, which is based on the plasma recombination light.

These findings constitute significant progress as regards the key community goals of making plasma accelerators better controllable and generate tunable high-quality electron beams.

Zusammenfassung

Die beschleunigenden Felder in Plasmawellen sind um einen Faktor von etwa 100 höher, als die von derzeit verwendeten supraleitenden Beschleunigern. Dies erlaubt eine deutliche Reduktion von Beschleunigungsstrecke, was wiederum den Bau der kompakten Beschleunigern erlaubt. Eine solche Entwicklung wird dringend benötigt, wenn man die kontinuierlich steigende Nachfrage nach Strahlzeit an Beschleunigern und elektronenstrahlgetriebenen hochqualitativen Lichtquellen beobachtet. Ein elementarer Schritt in der Entwicklung der Plasmabeschleunignstechnologie ist die Kontrolle der in Plasmawellen erzeugten Elektronenstrahlen.

Diese Arbeit behandelt die Beschleunigung von Elektronenstrahlen in elektronenstrahlgetriebenen Plasmawelle, deren Injektion durch Femtosekunden-Infrarot-Laserpulse kontrolliert wird.

Zwei Injektionsmethoden konnten dabei experimentell zum ersten Mal realisiert werden: Die *Trojan Horse* Injektion und die *Plasma Torch* Injektion.

Bei der Trojan Horse Injektion handelt es sich um eine Ionisationsinjektionsmethode, bei der die Ionisation der Elektronen, die dann in der Plasmawelle beschleunigt werden, ausschliesslich durch den Laserpuls geschieht. Dadurch wird die Injektion unabhängig von den Feldern der Plasmawelle und die Eigenschaften der sekundären Elektronenstrahles können dezidiert beeinflusst werden. Das erfordert einerseits einen sehr exakten Aufbau und gute zeitliche Kontrolle des Lasers und des treibenden Elektronenstrahls. Andererseits jedoch können mit dieser Methode Elektronenstrahlen mit bisher unerreichter Emittanz produziert werden.

Im Theorie- und Simulationsteil dieser Arbeit wird der Mechanismus untersucht, der das Stromprofil des injizierten Elektronenstrahles bestimmt. Dieses Modell wird dann aufgenommen für eine numerische Studie zur Trojan Horse Injektion in einer sich ausdehnenden Plasmawelle auf einer Plasmadichterampe. Es wird gezeigt, dass durch Injektion auf einer Dichterampe die Anforderung an den Strom des treibenden Elektronenstrahls deutlich verringert werden kann. Über die Intensitätsverteilung des Lasers und den Gradienten der Dichterampe kann dann das Stromprofil des erzeugten Elektronenstrahles gezielt gesteuert werden, wobei die hohe transversale Strahlqualität, die der Trojan Horse Injektion zu Eigen ist, nicht verringert wird.

Die Plasma Torch Injektion ist eine Methode, die auf dem gezielten Einwirken auf die Phasengeschwindigkeit der Plasmawelle basiert und ist insofern vergleichbar mit der Dichterampeninjektion. Diese Arbeit beschreibt den ersten experimentellen Beweis der Trojan Horse und Plasma Torch Injektion, erbracht durch die E210 Kollaboration am SLAC National Laboratory.

Der Experimentalteil dieser Arbeit beschreibt Experimentaufbau, Kalibierungen und Datenanalyse zu beiden Methoden. Ausserdem wird die Analyse einer neuen, plasmabasierten Synchronisationsmethode zwischen Elektronenstrahl und Laserpuls präsentiert.

CONTENTS

1

INTRODUCTION

For decades now, particle accelerators have been one of the most valuable scientific tools for groundbreaking insight into microscopic structures. The very simplified reason is that with high energy comes high resolution. This is true for particle physics, where structures and particles are explored by means of collisions and for photon science, where complex structures like molecules, clusters, shockwaves etc. are probed. The dawn of photon science began when it was realized that synchrotron radiation, which limits the energy gain in circular accelerators, can be put to great use for the determination of structures. With the development of synchrotrons as a light source, photon science got connected with electron accelerator research and development. Nowadays a variety of light sources from electron accelerators is available. While classic synchrotron storage rings can provide comparatively broad-band radiation, the radiation from electrons oscillating in the alternating magnetic fields of wigglers and undulators is considered monochromatic. By utilizing tuned high-quality electron bunches in undulators, a resonant amplification of photons at a given wavelength can be achieved. These Free-Electron Lasers (FEL) can generate high-intensity sub-picosecond coherent light pulses, ranging from the infrared (IR) to the X-ray spectrum.

The demand for FEL beam time, both in the scientific community and in the industry is ever increasing. This is reflected by the increasing number of FEL light sources. Already existing FELs like LCLS or FLASH are being upgraded to LCLS 2 [1] and FLASH 2 [2]; in FLASH 2, a new linear accelerator (linac) is added to the still operational FLASH light source. Additionally, new FELs like the European XFEL [3] or the SwissFEL [4] were recently commissioned. The few tens of μm-long electron bunches required to power the FEL process need to be accelerated to energies in the GeV or multi-GeV range with small energy spread and momentum spread in order to reach the X-ray regime. Currently, such high energies demand up to several kilometers of accelerator infrastructure. The long acceleration length is determined by the accelerating structures. For example, the superconducting TESLA radiofrequency cavities [5], which are the core accelerator building blocks of XFEL and FLASH are built, are limited for theoretical reasons to $\approx 55\,\mathrm{MV/m}$ before quenching, i.e. leaving the super-conducting phase. Experimentally, $45.4\,\mathrm{MV/m}$ [6] has been reached so far. Increasing the accelerating fields and at the same time generating short, high-quality bunches is therefore key to decrease the infrastructure footprint and cost, which in turn can open up FEL-based research to smaller laboratories, not just large-scale research facilities.

Acceleration in plasma wakefields is a very promising candidate as it can generate accelerating fields on the order of $10\,\mathrm{GV/m}$. However, this promising acceleration technique needs

to be developed to provide high-quality electron beams. The Trojan Horse or underdense photocathode plasma wakefield acceleration [7] promises ultra-low emittance electron bunches in an electron-beam-driven plasma wakefield. In this scheme, an additional laser pulse is focused into the wake where it releases a secondary electron bunch, the witness bunch, inside the plasma wake. The method combines high-quality electron bunches with short acceleration lengths which make it a very promising candidate to make FEL-like radiation broadly available. The application of short low-emittance electron bunches is not limited to FEL applications only. It is also interesting for radiation generation from inverse Compton scattering or for applications in high-energy physics, where ultra-low emittance values are beneficial, because of the concomitant increase in luminosity. For all these reasons Trojan Horse Plasma Wakefield Acceleration is being investigated at several facilities. By the start of my work in 2014, the Trojan Horse was a concept which was merely described in simulations and had yet to be experimentally shown. Part of this thesis describes the route to the proof-of-principle of Trojan Horse injection.

The thesis is separated into 8 main chapters. Chapter 1 is the introduction. Chapter 2 lays out the theoretical basis for understanding the physical phenomena studied in this work in the area of plasma physics and Plasma Wakefield Acceleration (PWFA). Section 2.8.3 describes the principle of Plasma Torch Injection and is based on simulation studies for which the author[1] calculated plasma density profiles. These studies led to the publications [8, 9]. In section 2.8.6 dark-current-avoidance strategies in a Trojan Horse Injection experiment are presented by means of simulations. The section is also based on a publication [10] the author contributed to with calculations of the trapping potential. In chapter 3, the author presents his derivation of the longitudinal current formation of the injected electron bunch in the case of the Trojan Horse PWFA. This is done by combining the known concepts of tunnel ionization shown in section 2.3 with the wake-electric-field scaling laws presented in section 2.4 and the trapping condition calculated in section 2.7. The presented method allows to calculate the longitudinal current structure from laser and plasma properties[2]. The results from chapter 3 are important to understand the content of chapter 4, where the author examines the Trojan Horse Injection in an expanding plasma wake. Wake expansion and the corresponding wake phase-velocity reduction is achieved by a smooth plasma-density transition. The conclusions of the investigations are a decreased minimum drive-bunch current, a novel method to control the longitudinal witness-bunch shape which has a ultra-low emittance and a low slice-energy spread. The author's analysis performed for the content presented in chapter 4 can also be found in reference [12]. Details of the experimental work done in the course of the author's doctorate can be found in the chapters 5-8. The experiments were prepared and conducted with colleagues from the E210 collaboration, which includes members of the University of California (UCLA), University of Strathclyde and the University of Hamburg and other institutions. The experiments were performed at the *Facility for Advanced Accelerator Experimental Tests* (FA-

1 For simplicity, "the author" from now on refers to the author of this thesis.

2 A simulation study completing the picture numerically can be found in the master thesis by G. Hurtig [11]

CET) at the SLAC National Laboratory. A detailed description of the experimental conditions available at FACET is given in chapter 5. Chapter 6 shows preparatory calculations and plans concerning the optics specific to the E210 experiment. An important part of the experimental campaign was to establish and quantify the synchronization between the laser pulse and the electron beam, which is described in chapter 7. An Electro-Optical Sampling (EOS) timing diagnostic was set up to fulfill the timing measurement needs of the experiment. Thanks to the high accuracy of the EOS described in section 7.2, a novel synchronization method based on plasma recombination light was explored and developed in detail as described in section 7.3. The experimental evidence for Plasma Torch was adduced as described in section 8.2 and the result of the experimental evidence of Trojan Horse Injection can be found in section 8.3. The plasma-based synchronization and the electron injection results will form parts of publications currently in preparation. Then, chapter 9 summarizes the results presented so far in this work. Chapter 10 gives a brief overview of possible future developments connected to the topics of this thesis. For the near-term prospects, the author presents a numerical study concerning the applicability of the Plasma Torch and Trojan Horse Injection at the FLASHForward facility.

2

THEORETICAL FOUNDATION

The purpose of this chapter is to describe the physics involved in the acceleration of electron beams in the fields of a plasma wake in general and in particular for the specific case in which the injection of electrons in such a wake is controlled by a laser pulse. In order to understand the physical concepts, one first needs to define the fundamental electrodynamics, and then add the plasma, laser and particle beam physics elements which are crucial to this work. This leads to a quantitative description of the plasma wakefield and the injection and acceleration of electrons in it.

2.1 ELECTROMAGNETIC FOUNDATION

The basis of electrodynamics is given by the Maxwell equations [13, 14]. These are here expressed in the *International System of Units* (SI) and have the form

$$\vec{\nabla} \cdot \vec{E} = \frac{\rho}{\epsilon_0} \tag{2.1}$$

$$\vec{\nabla} \cdot \vec{B} = 0 \tag{2.2}$$

$$\vec{\nabla} \times \vec{E} = -\frac{\partial \vec{B}}{\partial t} \tag{2.3}$$

$$\vec{\nabla} \times \vec{B} = \mu_0 \vec{j} + \mu_0 \epsilon_0 \frac{\partial \vec{E}}{\partial t}. \tag{2.4}$$

The Maxwell equations describe the fundamental relation between the electric field $\vec{E}$, the magnetic field $\vec{B}$, the charge density

$$\rho_\mathrm{e} = n q_\mathrm{e} \tag{2.5}$$

and the current density

$$\vec{j} = q_\mathrm{e} n \vec{v}. \tag{2.6}$$

ρ_e and $\vec{j}$ can be expressed as functions of the particle density n for resting or moving charge distributions at velocity $\vec{v}$ and with fundamental (electron) charge

$$q_\mathrm{e} = 1.60217 \times 10^{-19}\,\mathrm{C}. \tag{2.7}$$

The constants ϵ_0 and μ_0 are the vacuum dielectric constant and the vacuum permeability with values given in SI units:

$$\epsilon_0 = 8.8541878 \times 10^{-12}\,\mathrm{C/Vm}, \tag{2.8}$$

$$\mu_0 = 1.2566371 \times 10^{-6}\,\mathrm{Vs/Am}. \tag{2.9}$$

They are connected to the speed of light in vacuum

$$c = 299,792,458\,\mathrm{m/s} \tag{2.10}$$

via the relation $c = 1/\sqrt{\mu_0 \epsilon_0}$.
The electric and magnetic fields can also be expressed in terms of the scalar potential Φ and the vector potential $\vec{A}$. The scalar potential can be calculated with the help of Poisson's equation

$$\nabla^2 \Phi = \frac{\rho}{\epsilon}. \tag{2.11}$$

The vector potential is defined via the magnetic field

$$\vec{B} = \vec{\nabla} \times \vec{A}. \tag{2.12}$$

After inserting equation 2.12 into Faraday's law 2.3, the relation between the electric field, vector potential and a scalar potential is found to be

$$\vec{E} = -\vec{\nabla}\Phi - \frac{\partial \vec{A}}{\partial t}. \tag{2.13}$$

Plugging Ampères Equation 2.4 into the vector identity

$$\vec{\nabla} \cdot (\vec{\nabla} \times \vec{B}) = 0 \tag{2.14}$$

gives the expression

$$\vec{\nabla} \cdot \left(\mu_0 \vec{j} + \mu_0 \epsilon_0 \frac{\partial \vec{E}}{\partial t} \right) = 0. \tag{2.15}$$

Evaluating this equation with the definitions for $\vec{j}$ and ρ we obtain the *continuity equation*

$$\frac{\partial \rho_\mathrm{e}}{\partial t} + \vec{\nabla} \cdot (\rho_\mathrm{e} \vec{v}) = 0. \tag{2.16}$$

The continuity equation states charge conservation in a system with currents. A single charged particle such as an electron with a mass of

$$m_\mathrm{e} = 9.10938291 \times 10^{-31}\,\mathrm{kg} \tag{2.17}$$

is deflected and accelerated by the electromagnetic fields as described by the *Lorentz equation*

$$\vec{F} = \frac{d\vec{p}}{dt} = \frac{d(\gamma m_\mathrm{e} \vec{v})}{dt} = q(\vec{E} + \frac{\vec{v}}{c} \times \vec{B}), \tag{2.18}$$

where $\gamma = \frac{1}{\sqrt{1-\frac{v^2}{c^2}}}$ is the relativistic gamma factor.

There are several definitions of a plasma, but one of the most appealing that we will follow in this work can be found in the classic textbook by Francis F. Chen: "A plasma is a quasineutral gas of charged and neutral particles[1] which exhibits collective behavior" [15]. This collective behavior is dominated by the electromagnetic interaction of the charged particles described by the Maxwell Equations 2.1-2.4.

Debye Shielding

The concept of *quasi-neutrality* as mentioned in the plasma definition arises from the tendency of the ions and electrons to shield each other over macroscopic distances inside the plasma. This can be illustrated best by calculating the response of the plasma at a temperature T to a point-like positive net charge Q. The electrostatic potential $U(\rho)$ caused by this charge leads to a re-arrangement of the charged particles surrounding it. Since the plasma is at finite temperature T, the resulting density distribution converges to a Boltzmann distribution in the radial direction ρ

$$n_e(\rho) = n_e e^{q_e U(\rho)/(k_B T)} \tag{2.19}$$

for the electrons and

$$n_i(\rho) = n_i e^{-q_e U(\rho)/(k_B T)} \tag{2.20}$$

for the ions around the positive net charge, where k_B is the Boltzmann constant .
Considering Poisson's law 2.11 in one dimension gives

$$\epsilon_0 \frac{\partial^2 U(\rho)}{\partial \rho^2} = q_e(n_e - n_i). \tag{2.21}$$

The expressions for the charge-density distributions are inserted and $n_e = n_i$ is assumed so that

$$\epsilon_0 \frac{\partial^2 U}{\partial \rho^2} = q_e n_e (e^{q_e U/(k_B T)} - e^{-q_e U/(k_B T)}). \tag{2.22}$$

For thermal energies $k_B T \ll q_e U$, a Taylor expansion gives

$$\epsilon_0 \frac{\partial^2 U}{\partial \rho^2} \approx q_e n_e (1 + \frac{q_e^2 n_e}{\epsilon_0 k_B T} U - 1 + \frac{q_e^2 n_e}{\epsilon_0 k_B T} U + \ldots) \tag{2.23}$$

$$\approx \frac{2 q_e^2 n_e}{k_B T} U. \tag{2.24}$$

The solution of the differential equation is the effective potential of the net positive charge and the surrounding attracted charges. It has the form

$$U = U_0 \exp(-\rho/\lambda_D) \tag{2.25}$$

1 Regarding the gas types we will conveniently assume them to be electrons, ions and neutral atoms and comment that other particles as well can fit the definition of a plasma, but such exotic compositions are beyond the scope of this work.

with the information about the range of the shielded Coulomb field embodied in the *Debye Radius*

$$\lambda_{\mathrm{D}} = \sqrt{\frac{\epsilon_0 k_{\mathrm{B}} T}{2 n_{\mathrm{e}} q_{\mathrm{e}}^2}}. \tag{2.26}$$

We can see that a plasma sphere with a radial length $L \gg \lambda_{\mathrm{D}}$ has its Coulomb fields shielded and appears to be charge-neutral to an outside observer.

The Plasma Frequency

An electron-density variation with respect to the ionic density n_{i} is equivalent to a net charge-density displacement. This leads to a strong electric field acting upon both ions and electrons[2], as a restoring force that evokes a harmonic oscillation in charge density at the characteristic frequency of the plasma. Since the ion mass m_{i} is large compared to the electron mass m_{e}, the electronic response is much quicker, which is why these plasma oscillations are dominated by the electrons, while the ions can be considered stationary.
Starting from the Poisson equation 2.11, the electric field from a charge separation between the electron density n_{e} and the ion density n_{i} with an ionization level Z_{i} can be calculated as

$$\epsilon_0 \vec{\nabla} \vec{E} = q_{\mathrm{e}} (Z_{\mathrm{i}} n_{\mathrm{i}} - n_{\mathrm{e}}). \tag{2.27}$$

A small electron-density perturbation δn is assumed so that n_{e} is substituted with $n_{\mathrm{e}} \to n_{\mathrm{e}} + \delta n$. The condition $Z_{\mathrm{i}} n_{\mathrm{i}} = n_{\mathrm{e}}$ leads to the expression

$$\epsilon_0 \vec{\nabla} \vec{E} = q_{\mathrm{e}} \delta n. \tag{2.28}$$

Taking the time derivative of the continuity equation 2.16 and inserting the equation of motion in an electric field $\frac{\partial \vec{j}}{\partial t} = \frac{q_{\mathrm{e}}^2 n_{\mathrm{e}}}{m_{\mathrm{e}}} \vec{E}$ gives

$$\frac{\partial^2 \rho_e}{\partial t^2} + \frac{n_{\mathrm{e}} q_{\mathrm{e}}^2}{m_{\mathrm{e}}} \vec{\nabla} \vec{E} = 0. \tag{2.29}$$

Equation 2.29 can be combined with equation 2.28 to the differential equation

$$\frac{\partial^2 \delta n}{\partial t^2} + \frac{n_{\mathrm{e}} q_{\mathrm{e}}^2}{\epsilon_0 m_{\mathrm{e}}} \delta n = 0, \tag{2.30}$$

where the relation $\rho_e = q_{\mathrm{e}} \delta n$ is used. The solution to this differential equation is a harmonic oscillation in density

$$\delta n(t) = \delta n_0 \cos(\omega_{\mathrm{p}} t). \tag{2.31}$$

The characteristic frequency of this oscillation

$$\omega_{\mathrm{p}} = \sqrt{\frac{n_{\mathrm{e}} q_{\mathrm{e}}^2}{\epsilon_0 m_{\mathrm{e}}}} \tag{2.32}$$

2 A plasma can of course also consist of several species of ions at a variety of different ionization levels. Such a case does not alter the physics fundamental to the concept of the plasma frequency.

is called the *plasma frequency* and is one of the most important parameters in plasma physics. In the context of plasma accelerators, it is convenient also to consider the wavelength associated with the plasma oscillations, the *plasma wavelength*

$$\lambda_\mathrm{p} = 2\pi \frac{c}{\omega_\mathrm{p}}. \tag{2.33}$$

In the context of plasma wakefield accelerators, the plasma wavelength gives the rough longitudinal length of a plasma wake, as we will see in section 2.4. Typical values for example for a plasma density $n_\mathrm{e} = 1 \times 10^{17}\,\mathrm{cm}^{-3}$ are

$$\omega_\mathrm{p} \approx 56400 \sqrt{n_\mathrm{e}[\mathrm{cm}^{-3}]}\,\mathrm{Hz} \approx 1.8 \times 10^{13}\,\mathrm{Hz} \tag{2.34}$$

$$\lambda_\mathrm{p} \approx 105.6 / \sqrt{n_\mathrm{e}[10^{17}\mathrm{cm}^{-3}]}\,\mu\mathrm{m} = 105.6\,\mu\mathrm{m}. \tag{2.35}$$

Electromagnetic Waves in Plasmas

The Debye shielding assumes a thermalized plasma and is not the correct physical concept to describe the reaction of a plasma to a rapid change in charge on a femtosecond timescale. The more appropriate figure of merit is to look directly at the propagation of electromagnetic waves in plasmas which is deduced following Mulser and Bauer [16].
The electromagnetic wave propagation is calculated by transforming the Maxwell equations into the differential equation

$$\vec{\nabla} \times \vec{\nabla} \times \vec{E} + \frac{\partial^2 \vec{E}}{c^2 \partial t^2} = -\frac{1}{\epsilon_0 c^2} \frac{\partial \vec{j}}{\partial t}. \tag{2.36}$$

In a plasma, the current density is nonzero, but only electronic flow velocity $\vec{v}_\mathrm{e}$ needs to be taken into account for the high frequencies we are considering in this work so that

$$\vec{j} = -q_\mathrm{e} n_\mathrm{e} \vec{v}_\mathrm{e}. \tag{2.37}$$

Equation 2.36 can be solved with an exponential ansatz for a linear wave propagating in the x direction at angular frequency ω

$$\vec{E} = \vec{E}_0 e^{(ikx - i\omega t)}. \tag{2.38}$$

Plugging the ansatz into the differential equation 2.36 gives

$$\vec{\nabla} \times \vec{\nabla} \times \vec{E} - k^2 \eta^2 \vec{E} = \frac{v_\mathrm{g} v_\mathrm{ph}}{c^2} \tag{2.39}$$

with the group velocity $v_\mathrm{g} = \frac{\partial \omega}{\partial k}$ and the phase velocity $v_\mathrm{ph} = \frac{\omega}{k}$. The index of refraction in an absorption-free plasma is

$$\eta = \sqrt{1 - \frac{\omega_\mathrm{p}^2}{\omega^2}}. \tag{2.40}$$

Equation 2.40 can be interpreted as a criterion for the propagation of the disturbance. For $\omega_p > \omega$, the refractive index η becomes imaginary, which is physically equivalent to a reflection of the wave, with the measure of the penetration depth being the *skin depth*

$$k_p^{-1} = \frac{c}{\sqrt{\omega_p^2 - \omega^2}} \overset{\omega_p \gg \omega}{\rightarrow} \frac{c}{\omega_p}. \tag{2.41}$$

From equation 2.40 one can see that the transition from reflection to transparency occurs at the cutoff frequency

$$\omega_p = \omega. \tag{2.42}$$

By plugging in the expression for ω_p from equation 2.32, one can define the electron density of the transition point

$$n_e^{\text{crit.}} = \frac{\epsilon_0 m_e \omega^2}{q_e^2}, \tag{2.43}$$

the *critical density*. A plasma at a lower electron density than the critical density is transparent for the light and is called *underdense* with respect to the light frequency, whereas at higher electron densities it is called *overdense*.
As an example we consider the central wavelength of a Titanium-Sapphire (Ti:Sa) laser, $\lambda = 800\,\text{nm}$. For such a laser system, the critical density in equation 2.43 is $n_{\text{crit.}} = 1.7 \times 10^{21}\,\text{cm}^{-3}$. In the following, we will only consider Ti:Sa laser systems and electron densities smaller than $1 \times 10^{19}\,\text{cm}^{-3}$. We can therefore in the context of this work safely assume that the plasma is transparent for laser light.

2.3 PLASMA GENERATION

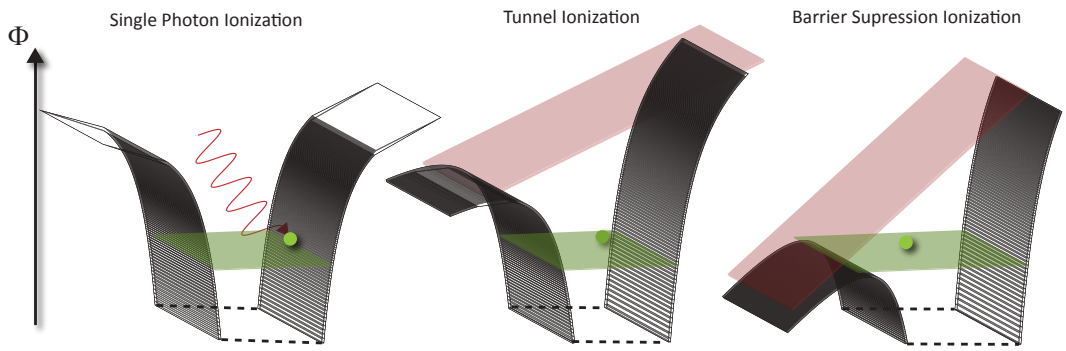

Figure 2.1: Visualization of different ionization regimes. Short-wavelength photons can excite electrons (green) to leave the atomic potential (l.h.s). Long-wavelength electric fields bend the potentials so that tunneling becomes more probable (center), until the potential is deformed to the barrier-suppression ionization regime (r.h.s).

When sufficiently intense, sub-picosecond laser pulses ionize gas to plasma. The underlying physics can be broadly divided into three different regimes: the single-photon or Multi-photon

Ionization (MPI); Tunnel Ionization (TI); and Barrier Suppression Ionization (BSI). MPI describes the absorption of one or several photons simultaneously by a bound electron such that the combined energy $\sum \hbar\omega_{\mathrm{Laser}}$ exceeds the electron's binding energy in the atomic potential and the electron is released into the continuum.

TI and BSI on the other hand describe an ionization that occurs due to the deformation of the potential, which means that the electron is released on a time scale over which the electric field of the laser can be assumed to be constant.

A handy parameter to distinguish between the multi-photon and tunneling ionization regime is the Keldysh parameter [17, 18, 19]

$$\gamma_{\mathrm{K}} = \sqrt{\frac{\xi_{\mathrm{ion}}}{2U_p}}. \tag{2.44}$$

The parameter is the ratio between the binding energy ξ_{ion} of an electron in an atomic potential and the ponderomotive potential

$$U_{\mathrm{p}} = \frac{q_{\mathrm{e}}^2 E^2}{4 m_{\mathrm{e}} \omega_{\mathrm{L}}} \tag{2.45}$$

which is the mean quiver energy of an electron in the electric field of the laser with frequency ω_{L}. γ_{K} was orignially called the "adiabaticity parameter" and compares the tunneling time of an electron in the Coulomb field of a hydrogen atom to the laser period. For a Keldysh parameter $\gamma_{\mathrm{K}} \ll 1$, the laser period is much larger than the tunneling time and TI is the dominating effect. In the case of $\gamma_{\mathrm{K}} \gg 1$ the opposite is true and MPI prevails.

The Yudin-Ivanov (YI) model describes the ionization behavior ranging from the pure tunnel ionization regime to the multi-photon regime and is divided into approximated solutions for different γ_{K}. In reference[20], solutions for $\gamma_{\mathrm{K}} \ll 1$, $\gamma_{\mathrm{K}} \approx 1$, $\gamma_{\mathrm{K}} \leq 2$ and $\gamma_{\mathrm{K}} \gg 1$ are presented.

Ammosov, Delone and Krainov have extended the tunnel ionization probability of electrons in a hydrogen atom to arbitrary atoms[3] and formulated the ADK model [22]. They calculated that for atoms with the principal quantum number $n^* \gg 1$, the orbital quantum number l and its projection m, the tunneling ionization probability for an electron with a binding energy ξ_{ion} being excited by a laser with peak electric field E is

$$w = C_{n^* l^*}^2 \left(\frac{3E}{\pi E_0}\right)^{\frac{}{}} \xi_{\mathrm{ion}} \frac{(2l+1)(l+|m|))!}{2^{|m|}|m|!(l-|m|)!} \left(\frac{2E_0}{E}\right)^{2n^*-|m|-1}. \tag{2.46}$$

where $n^* = Z_{\mathrm{i}}/\sqrt{2E}$, Z_{i} is the ionization level and $E_0 = \sqrt{2E}$. $C_{n^* l^*} = (\frac{2q_{\mathrm{e}}}{n^*})^{n^*}/\sqrt{2\pi n^*}$. In contrast to the YI model, the ADK model does not calculate the instantaneous ionization probability but the average ionization rate over one laser oscillation. However, it has been shown that the ionization rate between the laser cycles, as calculated by the ADK model, is in good agreement with the results from YI calculations if $\gamma_{\mathrm{K}} < 1$ [23].

3 A good review of TI theories can be found in reference [21]. In the appendix, it is argued that the ADK model is, in fact, merely a non-essential incremental description.

In the parameter regime of the ADK model, the laser-electric field is small compared to the ionic Coulomb field and the problem can be treated with perturbation theory. With stronger laser-electric fields this is not possible anymore. The critical electric field that divides TI and BSI is defined as the field for which the electron may escape the Coulomb potential classically [24, 25] and can be approximated to [26]

$$E_{\text{crit.}} \approx (\sqrt{2}-1)\left(\frac{\xi[\text{eV}]}{27.2\,\text{eV}}\right)^{3/2} 5.14\times 10^{11}\,\text{V/m}. \tag{2.47}$$

Bruhwiler et al. [26] have developed an approximate equation for the ionization rate which is optimized for numerical simulations such as Particle-In-Cell (PIC) simulation codes (see section 2.5). The approximate ADK ionization rate is

$$W_{\text{ADK}} = 1.52\times 10^{15}\frac{4^{n^*_{\text{eff}}}\xi_{\text{ion}}[\text{eV}]}{n^*_{\text{eff}}\Gamma(2n^*_{\text{eff}})}\left(20.5\frac{\xi^{3/2}_{\text{ion}}[\text{eV}]}{E[\text{GV/m}]}\right)^{2n^*_{\text{eff}}-1}\times\exp\left(-6.83\frac{\xi^{3/2}_{\text{ion}}[\text{eV}]}{E[\text{GV/m}]}\right)\ \text{s}^{-1} \tag{2.48}$$

for an atom or a molecule being ionized to the ionization level Z_{i} with its ionization energy ξ_{ion}[4] and the effective principal quantum number $n^*_{\text{eff}} \approx 3.69Z/\xi_{\text{ion}}$. Γ is the Gamma function. One has to keep in mind that equation 2.48 is only valid for electric fields below $E_{\text{crit.}}$. For higher electric fields, the ionization probability turns over and decreases again. This is obviously not physical and can lead to misleading results.

In this work, we consider ionization with laser intensities up to $10^{16}\,\text{W/cm}^2$ at a wavelength of $\lambda_{\text{Las}} = 800\,\text{nm}$, which corresponds to a $\gamma_{\text{K}} < 1$ regime. Therefore, Tunneling Ionization as described with the Ammosov-Delone-Krainov (ADK) model is a sufficiently good model.

The Ionization Gap

In the physically valid range of electric field strength for Tunnel Ionization, the ionization rate increases extremely rapidly. The consequence is that the difference between no ionization and full ionization of a certain ionization level is determined by only slight changes in electric field strength. This behavior can be seen in the graph 2.2, where the ionization rate is logarithmically plotted against the electric field. The onset of the rapid increase in ionization rate varies from element to element, which defines an ionization threshold electric field, that is specific to an element and ionization level. This can be used to shape the plasma density. By controlling the peak intensity of a short-pulse laser in a gas mixture with different ionization threshold values, distinct ionization of one low ionization threshold (LIT) component is permitted while the other high ionization threshold (HIT) component remains un-ionized. The ionization rates of lithium and helium e.g. qualify well as HIT and LIT components, with a large gap in ionization rates, but lithium, which vaporizes at 1603 K [28], requires external heating to become gaseous, which adds substantial complexity to an experimental setup. A good alternative that does not require

4 An extensive list of ionization energies can be found in [27].

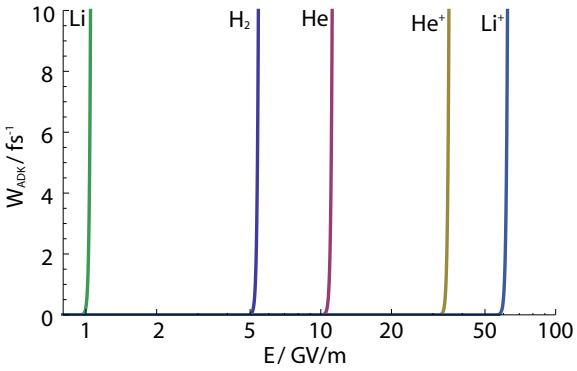

Figure 2.2: Tunnel ionization rate plotted against electric field strength in a log-lin plot for lithium, hydrogen and helium.

any heating is the combination of hydrogen and helium, a mix therefore used extensively in the context of this work.

Plasma density profiles from laser ionization

For a gas with a plasma density n_0 at full ionization, the ionization ratio at a given point in space in the lab frame is obtained by integrating the ionization rates over time such that the time-dependent ionization ratio is

$$\frac{n_e(t)}{n_0} = 1 - \exp\Big(-\int_{\infty}^{t} W_{\mathrm{ADK}}(t')dt'\Big). \tag{2.49}$$

We assume a laser pulse linearly polarized in a direction perpendicular to the propagation direction with pulse length τ. The electric field can be approximated by the envelope of the laser electric field to

$$E_\perp(t) = E_0 \exp(-\frac{t^2}{2\tau^2}), \tag{2.50}$$

since in the ADK theory the average over electric-field oscillations is taken. The complete envelope field distribution of a Gaussian laser in TEM_{00} mode is

$$E_\perp(r,z,t) = E_0 \frac{w_0}{w(z)} \exp(-\frac{r^2}{w(z)^2}) \exp(-\frac{t^2}{2\tau^2}) \tag{2.51}$$

in a cylindrical coordinate system, where $w(z) = w_0(1 + (\frac{z}{z_0})^2)^{1/2}$ is the beam waist at longitudinal position z and $z_0 = \pi w_0^2/\lambda$ is the Rayleigh length, the distance from the laser focus after which the laser spot size increases by a factor of $\sqrt{2}$. Now the complete ADK ionization integral is

$$n_e(r,z,t) = n_0\Big(1 - \exp\Big(-\int_{\infty}^{t} W_{\mathrm{ADK}}(E_\perp(r,z,t'))dt'\Big)\Big). \tag{2.52}$$

Figure 2.3 shows a cut through the r,z plane of the ionization ratio n/n_0 of laser-ionized He according to equation 2.52 at $t \gg \tau$. Sharp density transitions are visible transverse to the

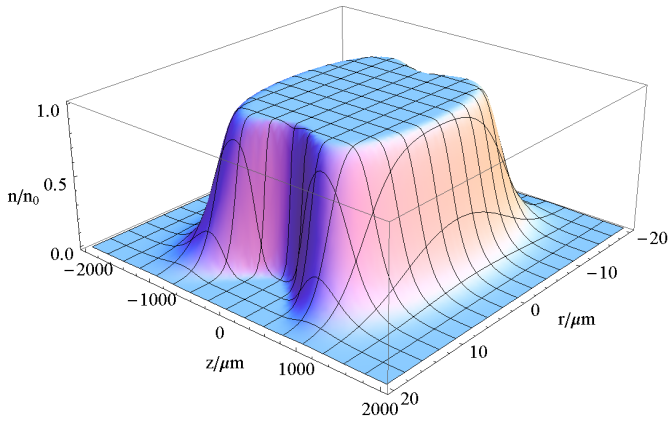

Figure 2.3: Cut through rz-plane of ionization ratio due to ionization of helium gas by a 1 mJ Gaussian laser pulse with waist $w_0 = 10\,\mu\text{m}$ and $\tau = 70\,\text{fs}$ FWHM pulse length, calculated from ADK theory.

laser pulse propagation direction z. This detail will become important in section 2.8.3 and in the experimental part of the thesis, since such sharp transitions are a convenient tool to precisely define pre-ionized plasma shapes that allow for the injection of electrons into plasma wakes.

Broadly speaking, there are currently two major approaches for the excitation of plasma wakes in order to harness them for electron acceleration, the Laser-driven WakeField Acceleration (LWFA) and particle-driven Plasma-WakeField Acceleration (PWFA). In LWFA, a high-intensity laser pulse with a typical duration of tens of fs [5] ionizes a gas to plasma and drives the wake, while in PWFA a high-current electron-beam is the driver[6] in an electron-beam ionized plasma or a pre-ionized plasma, depending on the application and the gases used as a plasma source. PWFA has a variety of advantages over LWFA, such as longer acceleration length and phase velocity near the speed of light, which enables advanced acceleration techniques such as the Trojan Horse injection. A good comparison between both methods can be found in reference [36].
Since this work only concentrates on simulations and experiments with electron-beam-driven PWFA, the theory will also only treat PWFA in depth.

The Quasi-static Approximation

Wakefields in plasmas are generated by a *driver*, which can be a laser pulse, or a charged particle beam, propagating through the plasma and seeding an electron density perturbation. The restoring forces natural to plasmas respond to this perturbation, which leads to a periodic density perturbation following the driver, comparable to waves trailing a boat on water. Hence, the wake shows a periodicity depending on the plasma environment and propagates at a phase velocity v_ϕ equal to the driver velocity

$$v_\phi = v_{\text{driver}}. \tag{2.53}$$

It is common and convenient to make a Galilean Transformation of the coordinate system from the lab-frame to a frame that moves along with the drive beam and the wake, the so-called *co-moving frame*. The transverse coordinates x and y are not changed by this transformation and z and t are expressed in a new co-ordinate

$$\xi = z - v_{\text{driver}} t, \tag{2.54}$$

which for drive-beams with $\gamma \gg 1$ can be approximated to

$$\xi = z - ct. \tag{2.55}$$

For the transformation into the co-moving frame, even though it moves with c, no Lorentz-transformation into the rest frame of the electron beam has taken place, so that all fields and

5 In the repertoire of laser-driven acceleration schemes there is also the plasma beat-wave accelerator that combines two ns-laser pulses at different wave length in order to resonantly excite a wake [29, 30, 31], or a single ns laser pulse breaks up into several beam-lets, exciting plasma wakes as in the self-modulated laser wakefield accelerator (SMLWFA)[32]. A good overview of laser-driven plasma-acceleration methods can be found in reference [33].

6 Other charged particles as drivers are also focus of current research such as protons[34] or positrons [35].

length scales are still described in the lab frame. This means that a function F that only varies in ξ, requires that

$$\frac{\partial F}{\partial t} = -c\frac{\partial F}{\partial z} \; \forall F(\xi). \tag{2.56}$$

The *Quasi-static Approximation* states that this is true for all functions relevant to the described physics, which in our case is the wake formation and acceleration in these wakes.

Plasma Wakefields in the linear regime

For the derivation of the linear wakefields, we will follow the calculations as presented in reference [37]. We assume that an electron bunch propagates through a plasma of electron density n_e at $v_b \approx c$ and with a beam density

$$n_b(\xi, r) \ll n_e. \tag{2.57}$$

This electron bunch acts upon the background plasma as a driver of a small plasma density perturbation $n_e = n_0 + n_1$ to which the plasma responds. Comparable to the mathematics for the derivation of equation 2.32, this perturbative approach allows for a linearization of the continuity equation 2.16 to

$$-c\frac{\partial n_1}{\partial \xi} + n_e \nabla \vec{v} = 0 \tag{2.58}$$

and respectively a linearization of the equation of motion to

$$-c\frac{\partial \vec{v}}{\partial \xi} = \frac{q_e}{m_e c}\vec{E}. \tag{2.59}$$

Combined with Gauss's law, this set of equations become

$$c^2\frac{\partial^2 n_1}{\partial \xi^2} = c\frac{\partial}{\partial \xi}(n_e \nabla \vec{v}) \tag{2.60}$$

$$\approx n_e \frac{\partial(\nabla \vec{v})}{\partial \xi} \tag{2.61}$$

$$= \frac{q_e^2 n_e^2}{\epsilon_0 m_e}(n_1 + n_b) \tag{2.62}$$

Now inserting Gauss's law results in the expression

$$\frac{\partial^2}{\partial \xi^2} n_1(\xi, r) + \left(\frac{\omega_p}{c}\right)^2 n_1(\xi, r) = -\left(\frac{\omega_p}{c}\right)^2 n_b(\xi, r). \tag{2.63}$$

Formula 2.63 gives the differential equation to calculate the plasma density response to a drive electron beam in the limit of $n_b \ll n_e$ and $v_b \approx c$. To facilitate a solution it can be assumed that the source term n_b is separable in r and z and confined to $r < r_{max}$ and $\xi < 0$ such that

$$\left(\frac{\partial^2}{\partial \xi^2} + k_p^2\right) n_1 = -n_b k_p^2 f(r) g(\xi). \tag{2.64}$$

The solution to this differential equation is

$$n_1 = n_\mathrm{b} f(r)\, \underbrace{k_\mathrm{p} \int_\xi^\infty d\xi' g(\xi') \sin(k_\mathrm{p}(\xi' - \xi))}_{G(\xi)}\,. \tag{2.65}$$

From the plasma density wake trailing the driver, n_1, one can now derive the fields generated by the wake, the *wake fields*. The longitudinal fields are [38]

$$E_z = E_\mathrm{WB} G(\xi)\, \underbrace{k_\mathrm{p}^2 \left(\int_0^r dr' r' f(r) I_0(k_\mathrm{p} r') K_0(k_\mathrm{p} r) + \int_r^\infty dr' r' f(r) I_0(k_\mathrm{p} r) K_0(k_\mathrm{p} r') \right)}_{F(\xi)} \tag{2.66}$$

$$= E_\mathrm{WB} G(\xi) F(\xi) \tag{2.67}$$

where K_0 and I_0 are the zeroth-order Bessel functions. The wake fields are proportional to

$$E_\mathrm{WB} = c m_\mathrm{e} \omega_\mathrm{p} / q_\mathrm{e} \simeq 96 \sqrt{n_\mathrm{e}(\mathrm{cm}^{-3})}\,\mathrm{V/m}, \tag{2.68}$$

which is the cold plasma wave-breaking limit. It was calculated by Tajima and Dawson in 1979 [29] and marks the maximum field strength that can be supported by a plasma described by fluid dynamics.

The radial fields $W_\mathrm{r} = E_\mathrm{r} - cB_\theta$ can be obtained by applying the *Panofsky-Wenzel Theorem* [39]. This theorem describes the transverse kick obtained by a charged test particle in an accelerating structure with transverse boundaries as e.g. in radiofrequency (RF) cavities. Rosenzweig describes in his book [40], how the Panofsky-Wenzel Theorem is applied to wake fields in plasma. The formulas of the theorem then become

$$\frac{\partial W_z}{\partial r} = \frac{\partial W_\perp}{\partial \xi} \tag{2.69}$$

$$\frac{\partial E_z}{\partial r} = \frac{\partial (E_r - cB_\theta)}{\partial \xi}. \tag{2.70}$$

The description laid out so far for the linear regime is limited to electron bunches at an electron density that is low with respect to the surrounding plasma density. For dense driver bunches, the radial fields become strong enough to radially expel all electrons in a defined volume that are then attracted back on axis by the restoring forces of the plasma, forming an electron-free ion channel trailing the driver bunch. This highly nonlinear regime is called the *blowout regime*. A good parameter to distinguish between linear and strongly nonlinear regime in PWFA is the ratio between the number of drive-beam electrons N_b and the number of plasma electrons in a cube with an edge length of the skin depth k_p [41, 42], which is

$$\widetilde{Q} = \frac{N_\mathrm{b} k_\mathrm{p}^{-3}}{n_\mathrm{e}}. \tag{2.71}$$

For values of $\widetilde{Q} \ll 1$ a linear wake is excited, and for $\widetilde{Q} \gg 1$ the wake is strongly nonlinear and in the blowout regime. The wake in the blowout regime undergoes a strong wave breaking, which means that the plasma electrons expelled by the drive beam propagate along crossing trajectories wrapping around the ion channel. As a consequence, a thin sheath of high electron density forms around the ion channel with smallest radius trajectory r_b[43]. During propagation along the blowout sheath, the electrons are accelerated by the ion channel and can reach energies as high as a few MeV at the vertex at the back of the wake. Electrons at such high energies are relativistic and could easily be injected into the wake, but the high phase velocity in PWFA of $v_\phi \approx c$ mostly inhibits trajectories that inject electrons into an accelerating phase of the wake. Ways to enable injection by means of wave breaking are discussed in section 2.7. In the blowout regime, due to the electron-free ion channel, the longitudinal electric field E_z does not depend on the radial component. Therefore, one can conclude from the Panofsky-Wenzel Theorem [39] that

$$\frac{\partial E_z}{\partial r} = \frac{\partial (E_r - cB_\theta)}{\partial \xi} = 0 \tag{2.72}$$

which predicts homogeneous focusing forces over the entire length of the blowout. The fields inside the blowout can be approximated as

$$E_\mathrm{z} \approx \frac{k_\mathrm{p} E_\mathrm{WB}}{2} \xi \tag{2.73}$$

$$E_\mathrm{r} \approx \frac{k_\mathrm{p} E_\mathrm{WB}}{4} r \tag{2.74}$$

$$B_\theta \approx -\frac{k_\mathrm{p} E_\mathrm{WB}}{4c} r \tag{2.75}$$

$$E_\mathrm{r} - cB_\theta \approx \frac{k_\mathrm{p} E_\mathrm{WB}}{2} r. \tag{2.76}$$

These scalings are very advantageous for the acceleration of secondary electron bunches inside the plasma wake. The linear radial focusing fields keep electron bunches compressed inside the blowout and therefore preserve their transverse spread in size and momentum (see definition of emittance in section 2.6). A comparison with 3D Particle-In-Cell simulations is presented in

figure 2.4 and figure 2.5 and show a good agreement with the presented scalings . The length of the blowout is approximately the plasma wavelength $\lambda_\mathrm{p} = 333\,\mu\mathrm{m}$ at the given plasma density of $1 \times 10^{16}\,\mathrm{cm}^{-3}$. The black line in figure 2.4 (a) is a linear cut through the accelerating field E_z in the center of the blowout. The red line compares this on-axis accelerating field to the prediction from equation 2.74. The independence of longitudinal fields on the radial position can be seen from the color-coded slice through the simulated accelerating fields, as well as from the transversely drawn cut (b).

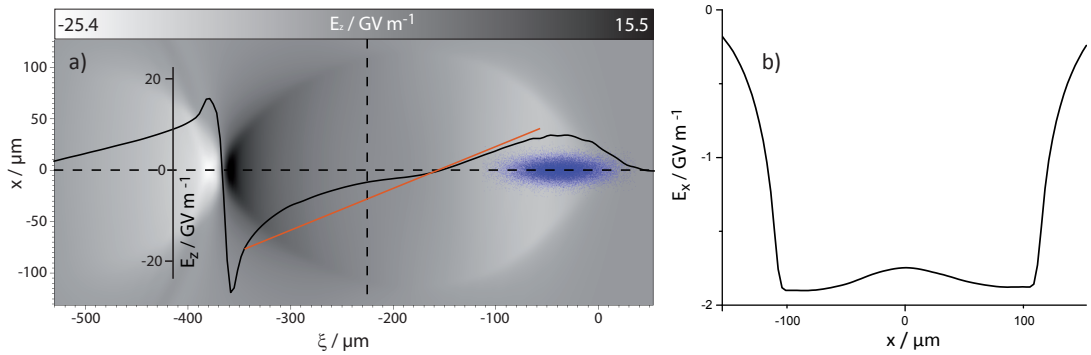

Figure 2.4: Slice through the on-axis transverse plane of the longitudinal electric fields E_z in a plasma wake excited by a 3 nC FACET-like drive beam in the blowout regime simulated with the particle-in-cell code VSim at a plasma density of $n_\mathrm{e} = 1 \times 10^{16}\,\mathrm{cm}^{-3}$. The longitudinal on-axis cut shows a typical linear dependence compared to the linear approximation (red) from equation 2.74 with a nonlinear increasing accelerating field at the vertex (a). The positions of the macro-particles (see section 2.5) of the 3 nC drive-bunch are projected onto the x-plane and plotted with reduced transparency for better visibility of the wake field. The transverse cut through the longitudinal fields at the position of the vertical dashed line in (a) is plotted in (b) and is approximately constant in the central region around $x = 0$.

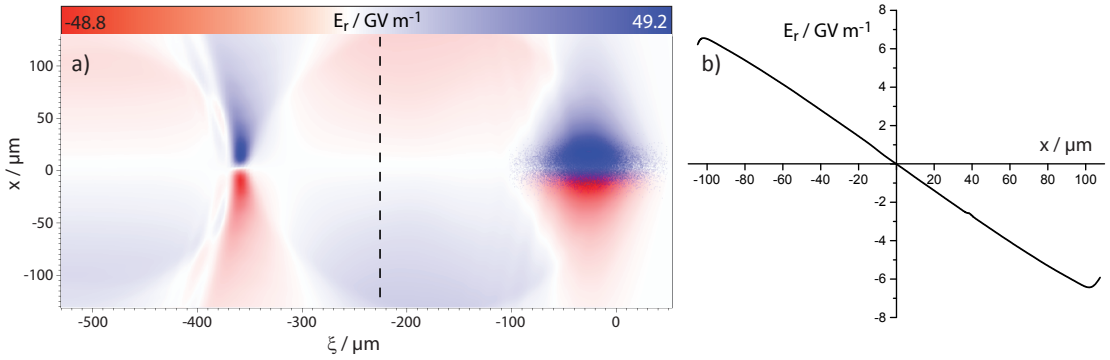

Figure 2.5: Slice through the on-axis transverse plane of the radial electric fields E_z in a plasma wake excited by a 3 nC FACET-like drive-beam in the blowout regime simulated with the particle-in-cell code VSim at a plasma density of $n_e = 1 \times 10^{16}\,\mathrm{cm}^{-3}$. A cut through the field along the dashed line shows a typical linear dependence (b). The positions of the macro-particles of the 3 nC drive-bunch are projected onto the x-plane and plotted with reduced transparency for better visibility of the wake field.

2.5 PARTICLE-IN-CELL SIMULATIONS WITH VSIM

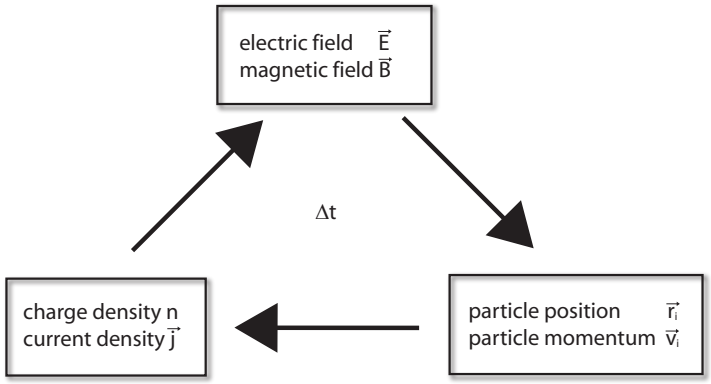

Figure 2.6: Particle-In-Cell algorithm.

Currently the most accurate description of the physics of PWFA in the blowout regime is given by Particle-In-Cell (PIC) simulations. Simulating particles and particle acceleration in plasma is an essential part of the plasma acceleration research field since its roots in the 1980s [29, 44]. The PIC code applied for the simulations shown in this work is VSim by TECH-X, the successor of the VORPAL PIC code[45]. The PIC algorithm relies generally on discretizing the space into a grid with electric and magnetic field values as well as currents and densities assigned to it and calculating the particle's response to its self-consistent fields. Not every single parti-

cle is simulated. Instead the particles are packed into macro particles that behave like single particles but are statistically evaluated according to their weight. In one simulation period the algorithm can be separated into different steps drawn out in a flow-chart in figure 2.6. First, VSim deposits macro particles according to given charge and current distributions. For PWFA simulations, this means mostly the deposition of plasma electron and ion macroparticles and driver-beam electron macro particles, the *BeamElectrons*. Ion macroparticles can also be neglected. In that case, the simulation background is effectively positive so that a lack of electrons naturally means a positive net charge. The BeamElectrons of the driver beam should not be initiated inside the plasma, because this leads to an erratic calculation of the drive-beam fields. Instead, in the simulations shown in this work, BeamElectrons are initiated in vacuum and then enter a plasma density upramp after some propagation distance in vacuum, which may differ among the simulation runs. Macro particles are not only added at the beginning of the simulation. Computation packages can be switched on or off to calculate ionization. In VSim, tunnel ionization and collision ionization can be utilized. In this work, only the tunnel ionization packages were used[7].

From the macro-particle distribution, charge density and current can be calculated, from which the field solver to solve Maxwell's equations. The electric and magnetic fields are arranged in a Yee mesh [46, 47], in which the electric fields are located on the grid edges and magnetic fields on the grid faces; they are calculated with the Finite-Difference Time-Domain (FDTD) method [46]. To minimize approximation errors, the electric and magnetic fields are calculated with the leap-frog algorithm, which means that their computation is staggered in time. The simulation box in VSim can be chosen to move along with the electron bunch, so that the simulation uses less computing time. The transverse boundaries consist of a so-called *matched absorbing layer* [47], an isotropic perfectly matched layer [48] that acts as an absorbing boundary condition. After solving the Maxwell's equations, the solution to the equation of motion is calculated. Then, the macro particles are re-located aaccording to their new momenta and positions in this time step. Macro particles outside the boundary of the co-moving simulation box are excluded from the simulation. The grid size and time steps must be chosen such that the spatial and temporal scale of the physics involved is still resolved. This means for example that in order to simulate the propagation of a laser pulse that drives a plasma wake as for a LWFA simulation, the laser oscillation with a typical length of 800 nm needs to be resolved. If, on the other hand, the purpose of a laser pulse is only to ionize gas, it can be approximated in the envelope equation 2.51, which is computationally more economical, because the grid can be broader than the laser wavelength. The minimum necessary requirement to ensure that the solutions obtained by the field solver converge is the Courant criterion [49]

$$\sqrt{(\Delta x)^2 + (\Delta y)^2 + (\Delta z)^2} > c\Delta t, \tag{2.77}$$

which gives a relation between temporal and spatial resolution. With the VSim 3D PIC code it is possible to reliably calculate the physics involved in PWFA, such as is done for reference [50].

7 For calculations sensitive to collision ionization the collision ionization packages will be applied in future work.

In the previous sections, we examined the physics of the beam-driven plasma-wake excitation. The ultimate goal as presented in this work is to advantageously make use of the wake fields in order to inject and accelerate high-quality secondary electron beams, conventionally called "witness beams" or "witness bunches".

In this section we will explain the basic electron-beam behavior in an accelerator and from that determine the most important parameters.

Single electron dynamics

The analysis of the single-particle dynamics in an accelerator beamline by definition leaves out any interaction with other charges. This means that, for now, any space-charge effects are ignored and the trajectory in spatial and momentum space is considered as a mere response to the beam optics. The equations of motion for an electron in external fields are

$$\frac{dW}{dt} = \frac{d}{dt}\gamma m_e c^2 = \vec{v}\cdot\vec{F}, \tag{2.78}$$

$$\vec{F} = \frac{d\vec{p}}{dt} = \frac{d}{dt}\gamma m_e \vec{v} = q_e(\vec{E} + \frac{\vec{v}}{c}\times\vec{B}) \tag{2.79}$$

from which the evolution in momentum and position of an electron can be calculated. The 6D space spanned by these spatial and momentum coordinates is called *phase space*. Here, z is the direction of acceleration. The coordinates x and y are the directions transverse to the acceleration. If given, y is pointing up. The two projected sub-spaces transverse to z are called transverse phase spaces or *trace spaces*. At a point in time, a particle in an accelerator is completely described by its phase space vector

$$\Phi = \begin{pmatrix} x \\ x' \\ y \\ y' \\ z \\ \delta \end{pmatrix} \tag{2.80}$$

with the transverse momenta $x' = \frac{p_x}{p_z}, y' = \frac{p_y}{p_z}$ and the deviation $\delta = \frac{\delta p_z}{p_z}$ from the nominal momentum[8] p_z. Any beam optics in an accelerator, even drift sections, change the phase-space vector of a particle. Similar to the mathematics of paraxial optics, these changes can be developed in a Taylor expansion [52]

$$\Phi_i^1 = \hat{R}_{ij}\Phi_j^0 + \hat{T}_{ijk}\Phi_j^0\Phi_k^0 + \dots, \tag{2.81}$$

8 A good description of linear beam optics can be found in the books written by Wiedemann [51] or Rosenzweig [40].

where 0 denotes the original state and 1 the state after the transformation. We assume that all changes are small compared to the original values or can be expressed as a series of linear transformations. Higher orders can be omitted so that the transformation is approximated to

$$\Phi^1 = \hat{R}_{ij}\Phi^0$$

$$\begin{pmatrix} x_1 \\ x_1' \\ y_1 \\ y_1' \\ z_1 \\ \delta_1 \end{pmatrix} = \begin{pmatrix} R_{11} & R_{12} & R_{13} & R_{14} & R_{15} & R_{16} \\ R_{21} & R_{22} & R_{23} & R_{24} & R_{25} & R_{26} \\ R_{31} & R_{32} & R_{33} & R_{34} & R_{35} & R_{36} \\ R_{41} & R_{42} & R_{43} & R_{44} & R_{45} & R_{46} \\ R_{51} & R_{52} & R_{53} & R_{54} & R_{55} & R_{56} \\ R_{61} & R_{62} & R_{63} & R_{64} & R_{65} & R_{66} \end{pmatrix} \begin{pmatrix} x_0 \\ x_0' \\ y_0 \\ y_0' \\ z_0 \\ \delta_0 \end{pmatrix}. \tag{2.82}$$

The transformation matrix

$$\hat{R}_{ij} = \frac{\partial \Phi_i^1}{\partial \Phi_j^0} \tag{2.83}$$

connects input and output parameters and is the Jacobian of this transformation. As such it requires $\det(\hat{R}) = 1$, which also means that only the changes due to conservative forces are described by equation 2.82. Later in this work, the matrix component R_{56} will become important. It connects an input deviation from design longitudinal momentum δ the to a deviation in longitudinal position

$$z_1 = R_{56}\delta_0. \tag{2.84}$$

Matrix element R_{56} is also an important parameter when considering the compression of electron bunches, as it describes how the bunch length is altered when propagating through a dispersive section of the accelerator such as dipoles, or combinations of dipoles such as doglegs or chicanes. In section 7.1 this is used to estimate the timing jitter of an electron bunch with respect to the nominal energy.

The Liouville Theorem

When considering an entire bunch of electrons it is useful to describe it as a smooth distribution $f(\vec{r}, \vec{p})$ in spatial ($\vec{r}$) and momentum ($\vec{p}$) coordinates. The distribution is normalized so that

$$\int_{-\infty}^{\infty} f(\vec{r}, \vec{p}) d\vec{r} d\vec{p} = 1. \tag{2.85}$$

The *Liouville Theorem* states that if only conservative forces are applied to the bunch, the total phase volume occupied by the distribution stays constant. This is mathematically equivalent to any transformation that maintains condition 2.85, which can be expressed by Jacobian transformations of the kind described by equation 2.82. Of course $\hat{R}$ does not need to act upon the entire 6D-Phase space. In fact, it is common to reduce the analysis and describe only changes in the trace space as the planes are mathematically independent and some beam-optical devices, as e.g. dipoles do not change both trace-space planes .

In order to obtain a measure of the actual phase-space volume, the statistical moments of the distribution can be determined by evaluating the integral

$$< x^n >= \int_{-\infty}^{\infty} f(\vec{r},\vec{p}) x^n dx. \tag{2.86}$$

Courant and Snyder in their summary paper [53] set the standard for defining the phase-space volume in the trace space with an elliptical equation for its boundary

$$\gamma < x^2 > +2\alpha < x >< x' > +\beta < x'^2 >= \epsilon. \tag{2.87}$$

The coefficients

$$\alpha = \frac{< xx' >}{\epsilon}, \beta = \frac{< x^2 >}{\epsilon}, \gamma = \frac{< x'^2 >}{\epsilon} \tag{2.88}$$

are the so called *Courant-Snyder coefficients* with $x' = \frac{p_x}{p_z}$ being the ratio between the transverse momentum p_x and the longitudinal momentmum p_z. The ellipse constant ϵ is the trace-space emittance. A distribution function $f(\vec{r},\vec{p})$, as defined with equation 2.85, is considered to be a smooth 6D-Gaussian function, with the rms trace-space values determining its borders as sketched in figure 2.7. The *rms trace-space emittance* is defined as [54]

$$\epsilon_{\mathrm{tr,rms}} = \sqrt{< x^2 >< x'^2 > - < xx' >^2}. \tag{2.89}$$

This can additionally be normalized to the *normalized rms trace-space emittance* into the form

$$\epsilon_{\mathrm{n,tr,rms}} = \gamma \epsilon_{\mathrm{tr,rms}} \tag{2.90}$$

$$= \frac{p_z}{m_e c} \sqrt{< x^2 >< x'^2 > - < xx' >^2}. \tag{2.91}$$

In this representation, its value stays constant under acceleration. We will mostly work with definition 2.91 when considering emittance. The emittance is an important value, as it is invariant under conservative transformations, and thus an important figure of merit for electron-beam quality in general. In particle accelerators the rms transverse beam size is

$$\sigma_x = \sqrt{\beta(z)\epsilon_{\mathrm{tr,rms}}} \tag{2.92}$$

at a given position z in the accelerator. The beta function $\beta(z)$ is determined by the beam emittance and the focusing strength of the beam-optics $k(z)$ connected by the differential equation

$$\beta''(z) + 2k^2(z)\beta(z) - \frac{2}{\beta(z)} = 0. \tag{2.93}$$

With no external force applied on the bunch, the differential equation 2.93 transforms to

$$\beta''(z) - \frac{2}{\beta(z)} = 0 \tag{2.94}$$

with the solution

$$\beta(z) = \beta^* + \frac{(z - z_0)^2}{\beta^*} \tag{2.95}$$

around a focal point z_0. Evaluating this solution with equation 2.92, the transverse electron-beam size increases from the waist spot size, σ_{r0}, like

$$\sigma_r(z) = \sigma_{r0}\sqrt{1+\left(\frac{z}{\beta^*}\right)}. \tag{2.96}$$

$\beta^* = \sigma_{x0}^2/\epsilon_{\mathrm{tr,rms}}$ is a measure of the focal length and is dependent on the trace-space emittance and the focusing. In the course of this work, the acceleration of electron bunches is simulated

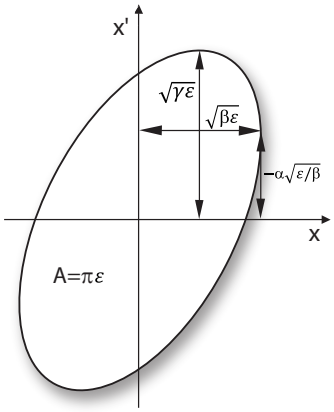

Figure 2.7: Illustration of the trace-space ellipse and its connection to the Courant Snyder coefficients.

with PIC codes in which the phase space is not a continuous distribution, but represented by the properties of macro-particles. For a discrete distribution, the definition of the emittance needs to be adjusted. Floettmann [54] suggested taking sums over n electron macro particles in the form

$$< x^2 > = \frac{1}{n}\sum_{i=1}^{n} x_i^2 - \frac{1}{n^2}\Big(\sum_{i=1}^{n} x_i\Big)^2 \tag{2.97}$$

$$< x' > = \frac{1}{n}\sum_{i=1}^{n}\Big(\frac{p_{x,i}}{p_{z,i}}\Big)^2 - \frac{1}{n^2}\Big(\sum_{i=1}^{n}\frac{p_{x,i}}{p_{z,i}}\Big)^2 \tag{2.98}$$

$$< xx' > = \Big(\frac{1}{n}\sum_{i=1}^{n} x_i\frac{p_{x,i}}{p_{z,i}} - \frac{1}{n^2}\sum_{i=1}^{n} x_i\sum_{j=1}^{n}\frac{p_{x,i}}{p_{z,j}}\Big)^2. \tag{2.99}$$

Emittance by definition describes a normalized particle distribution. It is therefore insensitive to the total charge of a particle bunch. To evaluate the efficiency of the bunch in terms of photon-source or scattering applications, however, it is important to also consider the bunch charge. For that the *Brightness* is a better parameter. The 6-dimensional normalized brightness is defined as [55]

$$B_{\mathrm{n,6D}} = \frac{Q_{\mathrm{b}}}{\epsilon_x\epsilon_y\epsilon_z}. \tag{2.100}$$

It depends not only on the transverse emittances, but also on the longitudinal phase-space volume $\epsilon_z = c\sigma_z(\Delta E/E)$, influenced by the relative energy spread $\frac{\Delta E}{E}$. In this work we will mostly consider the 4-dimensional peak brightness, defined as

$$B_{\mathrm{n,4D}} = 2\frac{I_\mathrm{p}}{\epsilon_x \epsilon_y}, \tag{2.101}$$

where the current is evaluated as peak current I_p and the emittances are the full-bunch trace-space emittances.

2.7 ELECTRON TRAPPING IN PLASMA ACCELERATORS

The wakefield in the blowout regime will now be applied to describe the trapping of electrons, where the condition for trapping is that electrons inside the wake reach the wake's phase velocity. The derivation follows reference [56].
From the Lorentz-force equation 2.18, the Hamiltonian for a single particle electron in an external potential

$$H = \gamma m c^2 + q_\mathrm{e}\Phi \tag{2.102}$$

can be derived. Taking the temporal derivative of the Hamiltonian we get

$$\begin{aligned}
\frac{dH}{dt} &= \frac{d}{dt}(\gamma m_e c^2) + \frac{d}{dt}(q\Phi) && (2.103)\\
&= \vec{v}\frac{d\vec{p}}{dt} + \frac{d}{dt}(q\Phi) && (2.104)\\
&= q\vec{v}(-\nabla\Phi - \frac{\partial\vec{A}}{\partial t}) + \frac{\vec{v}\times\vec{B}}{c} + \frac{d}{dt}(q\Phi) && (2.105)\\
&= q(\frac{d}{dt}\Phi - \vec{v}\vec{\nabla}\Phi - \vec{v}\frac{\partial\vec{A}}{\partial t}) && (2.106)\\
&= q(\frac{\partial\Phi}{\partial t} - \vec{v}\frac{\partial\vec{A}}{\partial t}) && (2.107)
\end{aligned}$$

Assuming that the wakefields are quasi-static during the trapping process, then for any function $f(\vec{r}, z - v_\phi t)$

$$(\frac{\partial}{\partial t} + v_\phi\frac{\partial}{\partial z})f(\vec{r}, z - v_\phi t) = 0. \tag{2.108}$$

This is also true for the Hamiltonian, so that it can be written as

$$\begin{aligned}
\frac{d}{dt}H &= q(\frac{\partial\Phi}{\partial t} - \vec{v}\frac{\partial\vec{A}}{\partial t})\\
&= -qv_\phi(\frac{\partial\Phi}{\partial z} - \vec{v}\frac{\partial\vec{A}}{\partial z}).
\end{aligned}$$

Since $H - v_\phi P_z = \text{const.}$ the following transformations can be done:

$$H - v_\phi P_z = \text{const.} \tag{2.109}$$

$$\gamma mc^2 + \Phi - v_\phi p_z - v_\phi q A_z = \text{const.} \tag{2.110}$$

$$\gamma + \frac{q\Phi}{mc^2} - v_\phi \frac{p_z}{mc^2} = \text{const.} \tag{2.111}$$

$$\gamma - v_\phi \frac{p_z}{mc^2} - \underbrace{\frac{q}{mc^2}(\Phi - v_\phi A_z)}_{\bar{\Psi}} = \text{const.} \tag{2.112}$$

$\bar{\Psi}$ is the trapping potential, which moves with a phase velocity v_ϕ with respect to the laboratory frame. It is valid both for small and for relativistic velocities. With the trapping potential, one can calculate if an electron inside the plasma wake will be successfully injected and accelerated or not i.e. if an electron will be able to catch up with the wake's velocity during the propagation of the wake or whether it will slip out of the potential. From the previous calculations, a general formula can be determined:

$$\Delta\bar{\Psi} = \bar{\Psi}_\mathrm{i} - \bar{\Psi}_\mathrm{f} = \gamma_\mathrm{f} - \gamma_\mathrm{i} - \gamma_f \frac{v_\phi v_\mathrm{f}}{c^2} + \gamma_\mathrm{i} \frac{v_\phi v_\mathrm{i}}{c^2}. \tag{2.113}$$

To apply this derivation for predictions of the electron trapping behavior in the plasma wake, it is necessary to define a trapping condition. An obvious and conventional choice is that an electron should catch up with the wake's velocity so that $v_\mathrm{f} = v_\phi$. Equation 2.113 consequently simplifies to the trapping condition

$$\Delta\bar{\Psi} \leq \gamma_\phi - \gamma_\mathrm{i} - \gamma_\phi \frac{v_\phi^2}{c^2} + \gamma_\mathrm{i} \frac{v_\phi v_\mathrm{i}}{c^2} \tag{2.114}$$

$$\leq \gamma_\phi \underbrace{(1 - \frac{v_\phi^2}{c^2})}_{=\gamma_\phi^{-2}} - \gamma_\mathrm{i}(1 - \frac{v_\phi v_\mathrm{i}}{c^2}) \tag{2.115}$$

$$\leq \gamma_\phi^{-1} - \gamma_\mathrm{i}(1 - \frac{v_\phi v_\mathrm{i}}{c^2}). \tag{2.116}$$

Equation 2.116 can be used to define a 3-dimensional volume with the fundamental property that electrons released inside this volume fulfill the necessary condition to be trapped inside the wake. This volume will be referred to as the *trapping region*.
Equation 2.116 is now further separated into different physical cases that are examined below.

Phase velocity at speed of light, electron injected at rest

In this case, the plasma wake travels with a phase velocity near to the speed of light, which is the case for beam-driven scenarios with high-γ driver beams ($v_\phi \approx c$), and electrons starting inside the wake initially at rest ($v_\mathrm{i} \approx 0$). Here, equation 2.116 simplifies to

$$\Delta\bar{\Psi} \leq \cancelto{0}{\gamma_\phi^{-1}} - 1 \tag{2.117}$$

$$\leq -1. \tag{2.118}$$

Examples of this case are the underdense photocathode, or Trojan Horse injection [7], or wakefield-induced ionization injection [57].

Phase velocity at speed of light, electron injected with $v \neq 0$

In external injection schemes, the electrons are already pre-accelerated when they are injected into the wake so that the trapping condition becomes

$$\Delta\bar{\Psi} \leq -\gamma_i(1 - \frac{v_i v_\phi}{c^2}) \tag{2.119}$$

$$\leq -\gamma_i(1 - \frac{v_i}{c}). \tag{2.120}$$

Phase velocity smaller that speed of light, electron injected at rest

This case is given for example in ionization injection in LWFA [58, 59] or beam-driven ionization injection schemes in which the wake's phase velocity is retarded such as the Downramp-assisted Trojan Horse (DTH) [12], on which this work specially focuses. In the latter case, strictly speaking in equation 2.102 $\frac{dH}{dt} \neq 0$, but in the special case that $\frac{dH}{dt} \approx 0$ during the injection process of the electrons, the trapping condition equation

$$\Delta\bar{\Psi} \leq \gamma_\phi(1 - \frac{v_\phi^2}{c^2}) - 1 = \gamma_\phi^{-1} - 1 \tag{2.121}$$

can still be applied.

Superluminal wakefield

Physical situations in which the wake or at least part of the wake moves with a phase velocity faster than the speed of light can be imagined. This is the case for example when a beam-driven wake traverses an electron-density upramp. From previous derivations, it seems obvious that trapping electrons in such a superluminal wakefield is not possible, as γ_ϕ^{-1} becomes complex for $v_\phi > c$. However, if this condition is only transient, as in the case with a short density upramp, the phase velocity will return to c immediately after the transition. In this case, trapping can be possible nevertheless.

2.7.1 *The Trapping Position*

Assuming that the longitudinal wakefield $\frac{\partial E_z}{\partial r} = 0$ for a sufficiently large radius and that the witness-bunch electrons are released approximately in the radial center of the wake, where the transverse focusing fields are weakest, the trapping behavior can be described by only

considering the accelerating electric field E_z. As described with equation 2.74, the accelerating field can be approximated to

$$E_z(\xi) = \frac{1}{2}\widetilde{E}_0 k_p \xi, \tag{2.122}$$

where the origin of the coordinate system is shifted such that $\xi = 0$ is at the zero crossing of the electric field. Since the total length of the plasma wake is $\approx \lambda_p$, equation 2.122 is only valid within the boundaries $[-\lambda_p/2, \lambda_p/2]$. $\widetilde{E}_0$ is the gradient of the accelerating field. It can be identified with the cold plasma wave-breaking limit E_{WB} in equation 2.68, but can also differ from it by a constant factor, depending on the drive-bunch properties [60]. Integrating equation 2.122 with respect to ξ gives the wake potential

$$U_z(\xi) = \frac{1}{4}\widetilde{E}_0 k_p \xi^2. \tag{2.123}$$

The trapping condition for an electron released at rest in a wake with $v_\phi \approx c$ is given by equation 2.118 to

$$\bar{\Psi}_i - \bar{\Psi}_f = -1, \tag{2.124}$$

where $\bar{\Psi}_i$ is the trapping potential at the release position ξ_i of the electron bunch and $\bar{\Psi}_f$ is the trapping potential at the final position ξ_f after the trapping. We identify $\bar{\Psi}(\xi) = \frac{q_e}{m_e c^2} U_z(\xi)$ and insert equation 2.123:

$$U_z(\xi_i) - U_z(\xi_f) = -\frac{m_e c^2}{q_e} \tag{2.125}$$

$$\xi_i^2 - \xi_f^2 = -\underbrace{\frac{4 m_e c^2}{\widetilde{E}_0 k_p q_e}}_{\alpha_t} \tag{2.126}$$

$$\xi_f = \pm\sqrt{\xi_i^2 + \alpha_t}. \tag{2.127}$$

In principle, ξ_f can have positive or negative values, but causality implies that only trapping positions at the back of the wake, i.e. negative solutions, can be realized. One can see from equation 2.127 that release and trapping position are not linearly connected. Hence, depending on the gradient of the electric field, the released bunch compresses during the trapping, an effect that is called *velocity bunching* which is analogous to the technique known in classical accelerators.

2.7.2 *Velocity Bunching*

In references [61, 62] bunch compression from velocity bunching is described in detail and the compression efficiency $\frac{\delta\xi_i}{\delta\xi_f}$ is evaluated for a sinusoidal accelerating field. In this work, the

calculation is applied to the linearized blowout electric fields. We combine equation 2.123 and equation 2.113 to obtain

$$U_z(\xi_i) - U_z(\xi_f) = \frac{m_e c^2}{q_e}\left(\gamma_\phi^{-1} - \gamma_i(1 - \frac{v_\phi v_i}{c^2})\right) \tag{2.128}$$

$$\xi_i^2 - \xi_f^2 = \frac{4m_e c^2}{\widetilde{E}_0 k_p q_e}\left(\gamma_\phi^{-1} - \gamma_i(1 - \frac{v_\phi v_i}{c^2})\right). \tag{2.129}$$

Re-arranging equation 2.129 with $\alpha_t = \frac{4m_e c^2}{\widetilde{E}_0 k_p q_e}$ and $v = c\sqrt{1-\gamma^{-2}}$ leads to the expression

$$\xi_f = -\sqrt{-\alpha_t\left(\gamma_\phi^{-1} - \gamma_i + \gamma_i\sqrt{(1-\gamma_\phi^{-2})(1-\gamma_i^{-2})}\right) + \xi_i^2} \tag{2.130}$$

$$= -\sqrt{A_t(\gamma_\phi, \gamma_i) + \xi_i^2}. \tag{2.131}$$

We define the function

$$A_t(\gamma_\phi, \gamma_i) = -\alpha_t\left(\gamma_\phi^{-1} - \gamma_i + \gamma_i\sqrt{(1-\gamma_\phi^{-2})(1-\gamma_i^{-2})}\right), \tag{2.132}$$

taking care of the dependence on the velocity gamma factor and the gamma factor of the injected initial electron bunch. A spread in initial release position $\delta\xi_i$ then leads to a spread in trapping position $\delta\xi_f$ so that

$$\xi_f + \delta\xi_f = -\sqrt{A_t + (\xi_i + \delta\xi_i)^2} \tag{2.133}$$

The compression factor is the ratio between the initial and the final position spread

$$C = |\frac{\delta\xi_i}{\delta\xi_f}| \tag{2.134}$$

$$= \frac{\delta\xi_i}{\sqrt{A_t + (\xi_i + \delta\xi_i)^2} + \xi_f} \tag{2.135}$$

$$= \left(\sqrt{\frac{A_t}{\delta\xi_i^2} + (\frac{\xi_i}{\delta\xi_i} + 1)^2} - \frac{\sqrt{A_t + \xi_i^2}}{\delta\xi_i}\right)^{-1}. \tag{2.136}$$

The compression is dependent on the initial bunch release positions and plasma density. As an example, equation 2.136 is plotted against release position ξ_i in figure 2.8. The result shows the advantageous release position at the zero-crossing of the accelerating field.

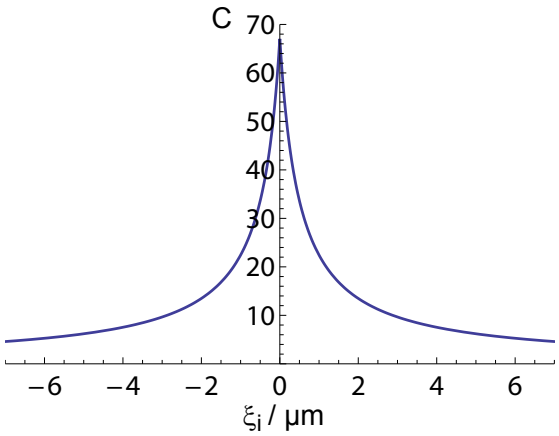

Figure 2.8: Equation 2.136 plotted as an example with $\gamma_\mathrm{i} = 1$, $\gamma_\mathrm{f} = 40000$, $n_\mathrm{e} = 1.7 \times 10^{17}\,\mathrm{cm}^{-3}$ and $\delta\xi_\mathrm{i} = 1\,\mu\mathrm{m}$.

2.8 ACCELERATION IN PLASMA WAKEFIELDS

The strong accelerating fields in PWFA can be utilized for acceleration in a variety of ways. Some basic principles of PWFA and an overview over acceleration and injection methods is presented in the following.

The Transformer Ratio

The transformer ratio

$$R_\mathrm{trans} = \frac{E^+_\mathrm{max}}{E^-_\mathrm{max}} \tag{2.137}$$

in PWFA is defined as the ratio of the maximum accelerating electric field behind the driving bunch, E^+_max, to the maximum decelerating electric field E^-_max acting upon drive-beam electrons. The transformer ratio is a value that can be obtained comparatively easily in an experiment when assuming that the acceleration length for the witness beam and deceleration length for the drive beam are equal and that the witness beam is accelerated at the peak accelerating field. Then the transformer ratio can be observed in the electron energy spectrum as the maximum energy gain of the witness beam divided by the maximum energy loss of the drive beam. In that sense, the transformer ratio is a measure of the efficiency with which the drive electron beam transfers energy to the witness electron beam. For a Gaussian driver bunch in the linear regime with rms sizes σ_r, σ_z, the peak accelerating field for narrow drive beams with radial rms size $k_\mathrm{p}\sigma_r < 1$ depends on the product $k_\mathrm{p}\sigma_z$ and has its maximum for the resonance condition $k_\mathrm{p}\sigma_z = \sqrt{2}$ [38]. In [63] it is calculated and simulated that in the linear regime the transformer ratio is limited to $R_\mathrm{trans} \leq 2$. However, for asymmetric drive-beam current profiles, it can reach up to $R_\mathrm{trans} \approx 6$ by applying a triangularly shaped drive-beam current [64].

Beam loading

For sufficiently high witness-bunch charge densities, the space-charge field generated by the witness bunch opposes the wakefield, so that it effectively reduces the accelerating field experienced by the witness bunch electrons. This, on one hand, decreases the transformer ratio due to lower accelerating fields, but on the other hand, flattens the fields so that the energy spread is reduced. This effect is called *Beam loading*.

Betatron oscillations

The transverse bunch size of the driver electron bunch behaves in vacuum according to paraxial optics as described by equation 2.96. As soon as the electron bunch enters the plasma, the transverse forces felt by the driver bunch are altered. In the blowout regime, the ion-channel focusing forces increase the bunch emittance. The rms beam radius r can be calculated with equation [65]

$$\frac{d^2r}{dz^2} + \frac{1}{\gamma_b}\frac{dr}{dz} + k^2 r = \frac{\epsilon_{n,rms}^2}{\gamma_b^2 r^3}. \tag{2.138}$$

The solution to equation 2.138 is an oscillatory trajectory and is said to be *Betatron Oscillation*. For a 3-dimensional electron bunch, different slices of the bunch can oscillate out of phase with each other, which can lead to an increase in emittance. Transverse bunch compression from betatron oscillations in the drive bunch normally leads to higher electric fields and a deeper wake potential, as can be seen from simulations. In an equilibrium state, no oscillation in transverse bunch size takes place. The equilibrium beam radius is calculated in [66] to be

$$R_{eq} = \left(8\frac{\epsilon_{n,rms}^2 c^2}{\gamma_b \omega_p^2}\right)^{1/4}. \tag{2.139}$$

An electron bunch that fulfills this criterion is called *transversely matched*. In the case that the electron bunch not only drives a wake but also ionizes the gas to plasma, a drive-beam electron population at the tail of the bunch propagates in plasma and the population at the head of the bunch propagates in the gas not yet ionized by the electron beam's field. The latter population propagates as in a vacuum and is not further focussed. Therefore, it diverges much faster than the rest of the bunch. This effect is known as *Head Erosion*[67] and can limit the acceleration length. The impact of Head Erosion can be reduced by pre-ionizing the plasma e.g. with a laser or a gas discharge [68].

2.8.1 *External Injection - Double Bunch Acceleration*

External injection is one of the least complex PWFA setups and is also the method that has been demonstrated much earlier than other methods. The basic idea is that a plasma wake is set up by one electron beam and other electrons - either from the same electron beam or a

trailing electron beam - are accelerated if they are in the right phase with respect to the wake. Figure 2.9 shows a sketch of a "driver/witness" PWFA in the blowout regime. The first experi-

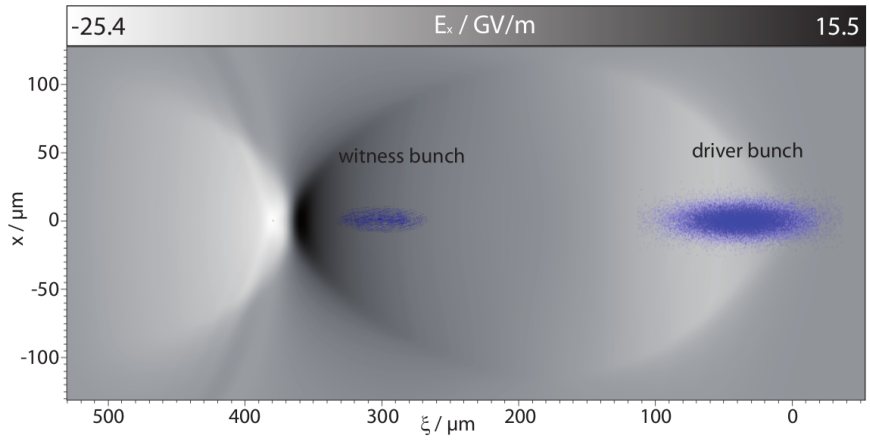

Figure 2.9: Sketch of a double-bunch acceleration. The driver electron beam excites a plasma wake, here in the blowout regime and continuously looses energy due to the decelerating fields, while the electrons of the witness beam that follow in the accelerating field gain energy.

mental realization of a PWFA was established in 1988 at the Argonne Advanced Accelerator Test Facility (AATF) [69]. With a method previously successfully applied to measure the wake fields in accelerating structures, a $2-3\,\mathrm{nC}$ electron beam with an rms bunch length of $2.4\,\mathrm{mm}$ was used to drive a wake in a $33\,\mathrm{cm}$ long plasma with density of the order of $10^{13}\,\mathrm{cm}^{-3}$. The driving bunch was followed by a low-charge witness beam whose delay was varied in order to scan the wakefield. The oscillating nature of the wakefield was well measured, with a maximum accelerating gradient of $1.6\,\mathrm{MV/m}$. With a higher driver beam charge of $4\,\mathrm{nC}$ [70], it was later possible to show a non-linear wake with an accelerating field of $5.3\,\mathrm{MeV/m}$.

In 2006 at the Final Focus Test Beam Facility (FFTB) at the Stanford Linear Accelerator Center (SLAC), the blowout regime was finally reached as described in [50]. A $42\,\mathrm{GeV}$ electron beam with a spot size of $10\,\mu\mathrm{m}$ and rms bunch length of $\approx 15\,\mu\mathrm{m}$ propagated through a $85\,\mathrm{cm}$ Li vapor generated in an oven. The shorter, high-current bunch now allowed acceleration in a much higher plasma density of $2.7\times10^{17}\,\mathrm{cm}^{-3}$ in the blowout regime. The extremely high wakefield gradient of $52\,\mathrm{GV/m}$ effectively accelerated part of the electron beam to up to $85\,\mathrm{GeV}$.

The Facility for Advanced Accelerator Experimental Tests (FACET) [71] is the successor facility to the FFTB for plasma acceleration. Several double bunch experiments have been successfully conducted there. At FACET, the double bunches are produced by accelerating one long chirped electron bunch all the way to the final chicane. Inside the chicane, the bunch is rotated and chopped into two bunches by a mask [72]. This method has the advantage that the transport of the beam along the LINAC is only required for one bunch. Efficiency and beam-loading effects were studied in a double bunch experiment as reported by Litos et al. [73].

Double-bunch acceleration is not limited to electrons. It can also be done with an electron driver accelerating positrons or a positron driver accelerating positrons. Recently at FACET a double-bunch PWFA of positrons in a positron-driven wake was demonstrated by shaping the transverse plasma shape to a hollow channel, which effectively avoids any transverse fields that would otherwise defocus the positrons [74].

2.8.2 *Density Downramp Injection*

As mentioned before, in the case of a constant plasma density, the phase velocity of the plasma wake in PWFA is equal to the velocity of the driving electron bunch $v_\phi = v_{\text{bunch}}$, which is normally close to the speed of light. This feature of PWFA makes dephasing, when the witness bunch catches up with the drive bunch in the co-moving frame due to velocity differences between the bunches, practically negligible. However, it also makes the injection of electrons from the plasma into the wake more difficult, because the electrons need to approach a relativistic velocity when entering an accelerating phase of the wake. The injection can be facilitated by lowering the phase velocity. This is e.g. achieved when the driving bunch passes a density downramp. Since the plasma wavelength λ_p (eq. 2.33), which is the characteristic scale of the longitudinal blowout length, depends on the plasma density, the blowout must expand in a density downramp and contract in an density upramp. The phase position of the wake is

$$\phi = k_\text{p}\xi \propto \sqrt{n_\text{e}(z)} \tag{2.140}$$

in the co-moving frame with $\xi = z - ct$ and the electron density $n_\text{e}(z)$ decreases with z, but is constant in t.

The phase velocity in a density gradient is

$$v_\phi(\xi, z) = -c\frac{\frac{\partial\phi}{\partial(ct)}}{\frac{\partial\phi}{\partial z}} = -\frac{\frac{\partial(k_\text{p}\xi)}{\partial t}}{\frac{\partial(k_\text{p}\xi)}{\partial z}} \tag{2.141}$$

$$= -\frac{(\cancelto{0}{\frac{\partial k_\text{p}}{\partial t}}\xi + \frac{\partial\xi}{\partial t}k_\text{p})}{\frac{\partial k_\text{p}}{\partial z}\xi + \frac{\partial x}{\partial z}k_\text{p}} \tag{2.142}$$

$$= \frac{ck_\text{p}}{k_\text{p}\frac{1}{2n_\text{e}}\frac{\partial n_\text{e}}{\partial z}\xi + k_\text{p}} \tag{2.143}$$

$$= \frac{c}{\frac{1}{2n_\text{e}}\frac{\partial n_\text{e}}{\partial z}\xi + 1} \tag{2.144}$$

Bulanov et al.[75] studied injection of electrons into the second plasma wake, trailing the drive bunch, where they assumed the density downramp to be longer than the plasma wavelength λ_p. Injection into the first trailing plasma wake in PWFA from sharp density transitions, with a downramp shorter than λ_p, has been studied by Suk et al.[76]. With a 1D Hamiltonian analysis and simulations they found that for a linear density downramp with a scale length $L_\text{s} = \frac{n_\text{e}}{\partial n_\text{e}/\partial z}$, an injection criterion is

$$k_\text{p}L_\text{s} < 1. \tag{2.145}$$

In [77], England et al. refined this description by applying wave-breaking as a trapping criterion. They also observed in simulations that electrons from the high-density region were trapped in the wake fields.

The above considerations do not take account of the highly nonlinear blowout regime in which wave breaking and trajectory crossing of sheath electrons occur naturally, even for a flat plasma density profile. This means that in the blowout regime, even for rather smooth density gradients, trapping of sheath electrons is much more easily achievable. Grebenyuk et al. investigated the density downramp injection capabilities specific for the electron drive beam at the FLASHForward facility [78]. They showed successful injection in PIC simulations for a drive beam of 2.5 kA peak current and at $k_p L_s \approx 3.3$ [79] and little dependence of witness-bunch properties on downramp length variation when keeping the density gradient constant.

The interplay between drive-beam current, sheath-electron energy at the vortex and wake potential determines the trapped charge and witness bunch properties in this regime and is the subject of ongoing research.

Experimental realization of injection due to a density downramp has been successfully applied in laser-driven wakefield acceleration [80, 81, 82] . The first experimental realization in PWFA with an optically generated plasma density spike is demonstrated later in this thesis. The concept is described in the next section; experimental results can be found in chapter 5.

2.8.3 *Plasma Torch Injection*

In laser-driven plasma-wakefield acceleration schemes, density gradients are normally generated hydrodynamically for example with razor blades or knife edges as gas-flow obstacles that are positioned on top of gas jets [83, 84, 85]. This hydrodynamic approach is required because of the specific electric-field and laser-intensity parameters in typical LWFA. Because the laser excites the plasma wake by its ponderomotive force, which scales $F \propto I \propto E^2$, it needs to be very intense to drive a plasma wake and the laser-electric fields are so high that they fully ionize the gas in most cases. An effective plasma density shape can therefore not straightforwardly be produced by generating a plasma density profile with a preionization laser and a gas density downramp is necessary.

In PWFA, the transverse force scales with $F \propto E$, so that the electron beam needs much lower electric fields in order to drive a plasma wake. Ionization of a gas due to the driving electron beam can be avoided with negligible effect on the wake, which is why in PWFA, electron density gradients can be generated by locally controlling the ionization level of the plasma.

Our alternative approach is the optical generation of a plasma density spike, also called a *Plasma Torch* [8, 9] as the means to inject an electron bunch. We make use of the ionization gap explained in the chapter 2.3 to use a HIT and LIT medium for distinct plasma shaping by applying two laser arms with different levels of intensity. There are a number of possible gas

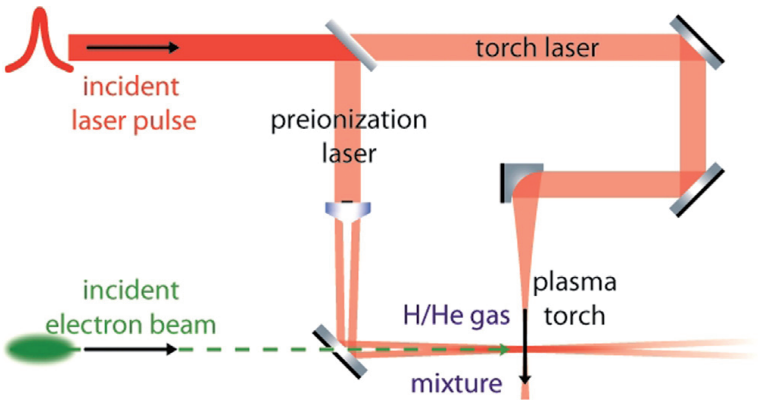

Figure 2.10: Sketch of a Plasma Torch injection setup taken from reference [9]. A pre-ionization laser arm generates a plasma on the electron-beam axis, ionizing only the H_2 of the H_2/He gas. A second injection laser arm ionizes a small density spike on axis by ionizing He in a confined volume with sharp density edges.

mixtures that can be used to ensure a sufficiently large ionization gap. In this work, we will only focus on the combination of helium as HIT and hydrogen as LIT medium (see figure 2.2). The plasma electron density shape and profile is determined by the laser pulses that ionize gas prior to the arrival of the driving electron bunch. This shape is generated over timescales down to few femtoseconds – the duration of the laser pulses – but it then is present over timescales eventually determined by the plasma recombination time, which is typically on the order of a few ns. Therefore, picosecond control over the relative time of arrival between the electron beam and the laser pulses is already sufficient to ensure that the electron bunch propagates through the desired density profile.

Figure 2.10 shows a sketch of the proposed setup [9]. A pre-ionization laser pulse ionizes a long plasma column and only ionizes the hydrogen gas to a homogeneous plasma along the electron-beam orbit. A second laser is focused down perpendicular to the beam propagation axis with higher intensity than the pre-ionization laser to ensure full He ionization in a confined volume. Both laser arms need to ionize the gas prior to the arrival of the electron bunch. Due to the exponential dependence between ionization rate and electric field, density downramps on the order of 10 μm length can be formed and picosecond-timing control ensures these profiles persist until the electron beam arrives. The gradients can be tuned very easily by changing the relative density of hydrogen and helium.

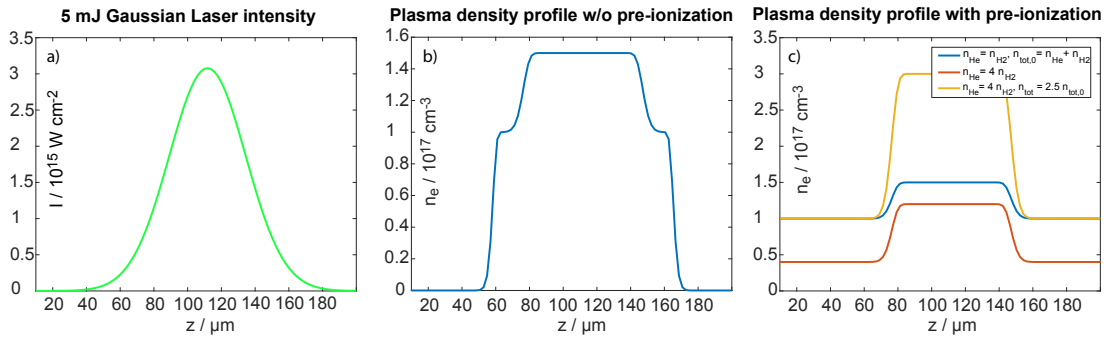

Figure 2.11: Part a) shows the calculated focal intensity distribution of a Gaussian laser pulse with 5 mJ energy, a pulse length of 20 fs FWHM and at 800 nm wavelength. The corresponding plasma density profile, calculated with ADK rates in a 1:1 H_2:He gas mixture, without pre-ionization is shown in part b). Image c) shows the plasma-density profile in the case of pre-ionized hydrogen at different gas properties. A plasma density profile for a H_2 to He gas mixture ratio of 1:1 (blue), 1:3 (red) and 1:4 at a total gas density increased by a factor of 2.5 (yellow) is plotted. The blue graph in part c) shows the same density and ratio as part b).

Figure 2.11 shows an example of possible plasma density spikes and control by relative and absolute HIT and LIT densities. The focal intensity distribution of a 5 mJ, 20 fs, 800 nm laser pulse and the corresponding density profiles are shown. Figure 2.11 b) shows the laser transverse density distribution calculated from tunnel ionization (eq. 2.52) in the case that there is no pre-ionization laser and assuming that the injection laser ionizes hydrogen as well as helium. The outer wings in the distribution are caused by the lower ionization threshold for hydrogen. In this example, both gases have the same molecular gas density and the total molecular gas density is $n_{\mathrm{tot}} = n_{\mathrm{H2}} + n_{\mathrm{He}} = 1 \times 10^{17}\,\mathrm{cm}^{-3}$.

Figure 2.11 c) shows how the density profile can be controlled in the case of two lasers, by changing the total gas density and the ratio between the molecular density of the gas components. The pre-ionization laser is assumed to fully ionize hydrogen and not to ionize the helium gas. If one starts with the density profile shown by the blue plot and wants to increase the density of the upper plateau while leaving the rest of the plasma density constant, changing the gas mixture only is insufficient. Changing from the 1:1 gas mixture (blue) to a 1:4 ratio between molecular hydrogen and helium at the same total gas density (red) leads to a decreased plasma density of the lower plateau before and after the plasma density spike. The total gas density needs to be increased by a factor of 2.5 to bring the lower-plateau plasma density back to $1 \times 10^{17}\mathrm{cm}^{-3}$. With these two parameters, the gas density and mixture ratio, the plateau plasma densities can be arbitrarily adjusted without changing the laser, which leaves the possibility to change the form of the downramp independently by modifying the laser properties.

In order to use the gas densities to control the ramp gradients, it is a necessity that the HIT and LIT media are not the same gas or that the HIT medium does not have a lower ionization energy

that is smaller than or equal to the ionization energy of the LIT medium. For example, Li and H_2 are two distinct gases, and the transition $Li^+ \rightarrow Li^{2+}$ has a large ionization gap, but the ionization energy for the transition $Li \rightarrow Li^+$ is even lower than for hydrogen. Therefore, the pre-ionization laser, if at the right energy to ionize hydrogen, will always additionally ionize the first level of Li and an independent density gradient regulation as previously described is no longer possible. In [8] and [9], the option of a Plasma Torch Injection for an electron bunch for the experiments described in chapter 5 was explored. Assuming a driver bunch with an energy of $W = 23\,\mathrm{GeV}$, an rms bunch length of $\sigma_z = 27\,\mu\mathrm{m}$ and a radial rms size of $\sigma_r = 8.5\,\mu\mathrm{m}$, the charge was varied between $Q = 1\,\mathrm{nC}$ and $Q = 3\,\mathrm{nC}$. The emittance was set to $\epsilon_\mathrm{n} = 2.25 \times 10^{-6}\,\mathrm{mrad}$. Three cases were studied:

1. Gaseous H_2 only, no preionization laser.
2. Gaseous H_2/He mixture, no preionization laser.
3. Fully ionized H_2, He ionized locally by the injection laser.

Cases 1 and 2 rely on ionization by the drive bunch. In these cases, injection occurs due to a sudden shift in wake phase velocity, which is caused by two effects. The first is from the plasma density transition because the drive bunch is not capable of fully ionizing a large column of gas to a plasma in case 1 and does not ionize He at all for case 2 so that the effective electron-beam-ionized plasma density is smaller than the density in the plasma torch volume. The second effect that causes a wake phase-velocity shift is the fact that in the plasma spike, the wake forms in plasma that does not need to be generated by the electron bunch. The bunch ionization in the gaseous environment shifts the ξ onset position of the wake upstream; this sudden shift also acts as a transitory phase-velocity decrease which allows for the injection of sheath electrons[9]. With a $3\,\mathrm{nC}$ drive bunch for case 1 and 2, injection of up to $530\,\mathrm{pC}$ was observed with an approximately linear relationship between torch plateau plasma density and injected charge. Simulations of case 3 generated the witness bunches with lowest emittance ($2.6 \times 10^{-6}\,\mathrm{mrad}$) and even for $Q = 1\,\mathrm{nC}$ drive-bunch charge, a total charge of $Q_\mathrm{W} = 260\,\mathrm{pC}$ could be accelerated.

2.8.4 *Ionization Injection*

In all previously outlined injection types, electrons to be accelerated in the wake are at a non-zero velocity when injected, which is an advantage as regards the requirements on the wake-field and the driver bunch, because injection is possible with shallower wake potentials (see section 2.7). Ionization injected electrons are in a bound state of an atom or molecule until they are released from this state into the continuum inside the wake. This means that the electrons are effectively at rest when being released into the plasma wake. A successful trapping of these electrons either requires the potential of the plasma wake to be deep or the electrons to be released at the right phase in the potential minimum.

9 This also means a superluminal phase velocity at the onset of the density spike.

The plasma in which the wake is excited needs to be only partially ionized, ideally with an ionized low-ionization-threshold (LIT) and a gaseous high-ionization-threshold (HIT) medium. Here, LIT and HIT can be taken from one and the same gas medium by making use of different ionization levels, as long as they are separated by a sufficiently large ionization gap as described in section 2.3. If, however, HIT and LIT are different gases such as H_2 and He, their gas density ratio becomes a useful additional degree of freedom to control the injected charge. Experimentally in reference [86], ionization injection was shown in a Rb oven. The electric field from the head of the electron beam was used to ionize $\mathrm{Rb} \rightarrow \mathrm{Rb}^{+}$, while the field from the tail of the drive beam overlapped with the wake electric fields. The sum of both fields was strong enough to further ionize $\mathrm{Rb}^{+} \rightarrow \mathrm{Rb}^{2+}$ inside the trapping region (see section 2.7). However, the injection can also occur in the back of the wake. In [87] and [57] a setup was examined both in theory and simulation where only the back of the wake had sufficiently high fields to ionize the HIT medium. It was shown that the combined requirements for trapping, i.e. the overlap between the ionization region and the trapping region, confine the possible parameter space of the electron source which enables the generation of electron bunches with low emittances of $\epsilon_x = 1.5\,\mu\mathrm{m}$. In order to maintain the high quality of the witness bunches, the injection was assumed to be limited to a small region of H2/He mixture by controlling the flow of a gas cell [57]. The ionization does not need to be triggered by the wake- or beam-electric fields. The witness-bunch electrons can also be released inside the wake by laser-induced ionization which leads to a decoupling of wake formation and injection process. Li et al. proposed to perform the ionization injection with two transverse colliding laser pulses [88]. Both pulses should overlap in the transverse center of the plasma wake such that only at this position is the electric field high enough to release electrons. Wan et al. [89] analyzed the injection by two colliding co-linear laser pulses. Injecting the witness bunch by ionizing with one co-propagating laser pulse is the Trojan Horse injection. A method that this work has a strong focus on and that is described in the next section.

2.8.5 *Trojan Horse Injection*

The underdense plasma photocathode mechanism or Trojan Horse injection is one of the most intriguing injection techniques. It was proposed in 2012 by Hidding et al. [7, 36] and has subsequently gained substantial scientific interest due to the very low achievable emittance values of order of a few $\epsilon_{\mathrm{rms}} \approx 10^{-9}\,\mathrm{mrad}$ and extremely good peak brightness of order of $B \approx 10^{19}\,\mathrm{Am}^{-2}\mathrm{rad}^{-2}$. In this method, neither the wake nor the beam-electric fields are sufficient to ionize the HIT medium, which constitutes a path towards reliable dark-current-free operation. Instead, triggering the ionization injection is the task of an additional short laser pulse trailing the driving electron beam. Given full control over laser-to-electron-beam alignment and synchronization, it is possible to ionize and release electrons wherever required in the wake. It was shown in figure 2.8 that a release in the potential minimum, i.e. the zero-crossing of the longitudinal electric wakefield, is particularly advantageous for high brightness because the bunch compression is maximal at this position.

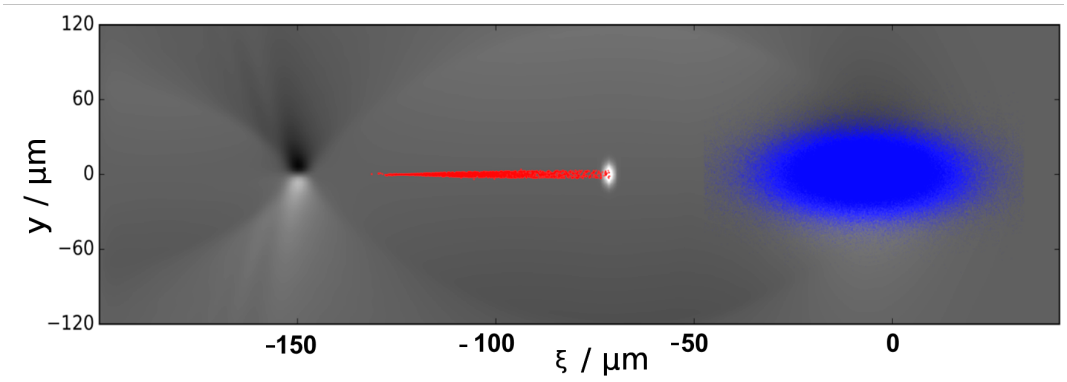

Figure 2.12: Underdense Photocathode during injection. The drive electron bunch (blue) excites a wake in the blowout regime. A short laser pulse (white peak in electric field sum) co-propagates with the electron beam, focused onto the beam axis and at the correct timing to release electrons (red) in the center of the wake. Witness-bunch electrons (red) move back with respect to the plasma wake in the co-moving frame while they are accelerated to relativistic speed and accumulate at the back of the wake.

The witness-bunch emittance is influenced by a variety of factors. One normally assumes that the momentum of the electron at the moment of its release is the same as the momentum of the originating ion. In experiments, the temperature of the gas is typically $T \approx 10^2 - 10^3\,\mathrm{K}$, which means the temperature of the HIT medium contributes little to the final emittance when compared to other factors and is negligible [90]. The electron release by the laser can be separated into two regimes depending on the laser properties: a weakly ionizing regime in which electrons are released over the length of the laser pulse barely exceeding the ionization threshold, and a strongly ionizing regime in which electrons are only released at the ionization

front of the laser pulse and approach full ionization. Further simulations and calculations in this work will only concentrate on the strongly ionizing regime.

Schroeder et al. [90] calculated that the laser does not influence the initial emittance, i.e. the thermal emittance, in the plane orthogonal to the laser polarization. The quiver motion of the electrons in the laser field only changes the thermal emittance in the polarization plane. However, in the limit of

$$\frac{k_\beta w_0}{2} \gg a_0 \tag{2.146}$$

with the matched betatron wave number $k_\beta = \omega_\mathrm{p}/(\sqrt{2\gamma}c)$, the thermal emittance coming from transverse momentum obtained in the laser field is small compared to the emittance coming from the transverse spatial distribution of the ionized electrons. If condition 2.146 holds, the contribution to the thermal emittacne coming from the quiver motion in the polarization plane of the laser can also be neglected and the emittance becomes symmetric in x and y.

In the case of Trojan Horse injection, the laser intensity can be small compared to the case of a laser-triggered ionization injection in a laser-driven plasma wake [91]. Therefore, a normalized laser amplitude of $a_0 \approx 0.02$ is already sufficient to ionize e.g. He to He^+.

For values typical to Trojan Horse simulations of $w_0 = 6\,\mu\mathrm{m}$ and a plasma wavelength of $1 \times 10^{17}\,\mathrm{cm}^{-3}$, condition 2.146 is met even for $\gamma = 1$ with $\frac{k_\beta w_0}{2} \approx 0.13 > 0.02$.

The initial emittance, in this case, is dominated by the transverse spatial distribution of the released electrons and depends on the laser wavelength λ and the ionization potential ξ_ion with the scaling

$$\epsilon \propto k_\beta w_0^2 a_0 \xi_{ion}^{-3/2} \lambda^{-1}. \tag{2.147}$$

For the evolution of the emittance during the acceleration, one has to consider the influence of *phase mixing*. In the Trojan Horse injection scheme, the individual electrons which form the witness bunch are not released at the same time. Instead, electrons are added to the witness bunch continuously until the laser is diffracted and does not ionize anymore. Electrons released first start to gain energy first and also start to rotate in the transverse phase space earlier than electrons released last. This spread in betatron phase leads to an increased emittance.

Xu et al. calculated that the emittance then decreases again because the electrons released first are at higher energy and rotate slower than the electrons released last [92]. This effect is called transverse phase mixing. After trapping, the witness bunch has a finite bunch length which goes along with a spread in accelerating field E_z. This spread leads to an energy spread which in turn decreases the spread of the betatron phases again. Consequently, this so-called longitudinal phase mixing causes the emittance to gradually grow again, after decreasing first due to transverse phase mixing [92].

The initial spread in betatron phase can be reduced by decreasing the propagation length of the laser over which it releases electrons. This can be achieved by controlling the focusing of the different wavelengths of the laser spectrum, a method which is known as simultaneous spatial and temporal focusing (SSTF) [93].

A detailed theoretical study, supported by PIC simulation parameter scans by Xi et al. [94] compared a description of Trojan Horse injection for different ionization models, the Ammosov-Deloine-Krainov (ADK) and the Yudin-Ivanov (YI) ionization theory in the weakly ionizing regime. The electrons were then numerically propagated by solving the equation of motion in the field of the laser and the plasma wakefield, obtained from PIC simulations. It was also discovered that the witness-beam emittance and brightness is insensitive to pulse length, but that emittance increases with w_0 and intensity. The results were in a good agreement between the emittance calculated with the YI and the ADK model for a Keldysh parameter in the range $\gamma_K = 0.77 - 0.59$ was found. The YI model becomes important when injection with e.g. a frequency-doubled Ti:Sa laser pulse with a wavelength of $400,\mathrm{nm}$ because in this $\gamma_K > 1$-regime multi-photon ionization is the predominating ionization process.

2.8.6 *Dark Current Mitigation*

Trojan Horse PWFA is a highly controllable ionization injection method due to the decoupled wakefields and injection-laser fields and allows for the generation of witness beams with uniquely low emittance values and excellent control over injection. The ionization gap between H_2 and He and a plasma wake potential deep enough to trap the released electrons from rest are core requirements. This requires a sufficiently strong excitation of the plasma wake which in turn requires a sufficiently high-current drive-bunch to excite the plasma wake. However, if the electric field is too high, He is ionized which can lead to injected charge from less decoupled ionization injection methods such as described in section 2.8.4.

In analogy to conventional photocathodes, any kind of charge injected by a method other than the intended one is referred to as *dark current*. In this work, the two intended methods of injection are plasma photocathodes in the form of the Plasma Torch or the Trojan Horse method.

Dark current can result from unwanted ionization injection mainly at two hot spots: ionization by the drive-beam electric fields or by wakefields. The electric fields in these hot spots may exceed the HIT level and hence liberate electrons. Fortunately, a further condition for this charge to become dark current is that it needs to be trapped, i.e. it must be released in the right phase with a trapping potential $\bar{\Psi} < -1$. This section addresses how to avoid dark current following the results from reference [10].

As mentioned in section 2.4, the wake electric fields in the blowout regime scale with the wave-breaking electric fields

$$E_{WB} = \frac{c m_e \omega_p}{q_e} \propto \sqrt{n_e} \propto \lambda_p. \tag{2.148}$$

This implies that the effects of wake-induced ionization injection can be mitigated by lower plasma densities or longer plasma wavelengths, which in turn also lowers the accelerating

fields as well as the slope of the electric field within the plasma wake.
The electric field of a point charge in its rest frame in the radial direction $\vec{\rho}$ is

$$\vec{E} = \frac{q_e}{4\pi\epsilon_0|\vec{\rho}|^3}\vec{\rho}. \tag{2.149}$$

If moving at relativistic speed v in the z-direction, the fields longitudinal to the propagation axis are squeezed due to relativistic length contraction, so that the fields as observed in both the lab frame and the co-moving frame become [95]

$$\vec{E} = \frac{q_e}{4\pi\epsilon_0|\vec{\rho}|^3}\frac{\gamma\vec{\rho}}{(x^2+y^2+\gamma^2z^2)^{3/2}}. \tag{2.150}$$

For highly relativistic charges at $\gamma \gg 1$, the electric fields are squeezed to such an extent that they become increasingly transverse, which means that the electric field of a highly relativistic electron bunch of rms bunch length σ_z and transverse rms size σ_r is longitudinally compressed in the laboratory frame with strong transverse electric fields with maximum value

$$E_{\max}(r) = \frac{Q}{2\pi^{3/2}\epsilon_0\sigma_z r}\left(1 - e^{-r^2/(2\sigma_r^2)}\right). \tag{2.151}$$

From this equation it can be deduced that a viable strategy to decrease the electric field is either to reduce bunch charge, to increase bunch length or to increase the radial bunch size σ_r. Since the electron bunch performs betatron oscillations (see section 2.8), its transverse size depends on plasma density, emittance and inital transverse bunch size. It should be noted that changing the drive-bunch current will also have a profound effect on the wakefield strength, which means that to some extent the reduction of driver hot spot and wake hot spot can be approached via driver-beam parameter changes.

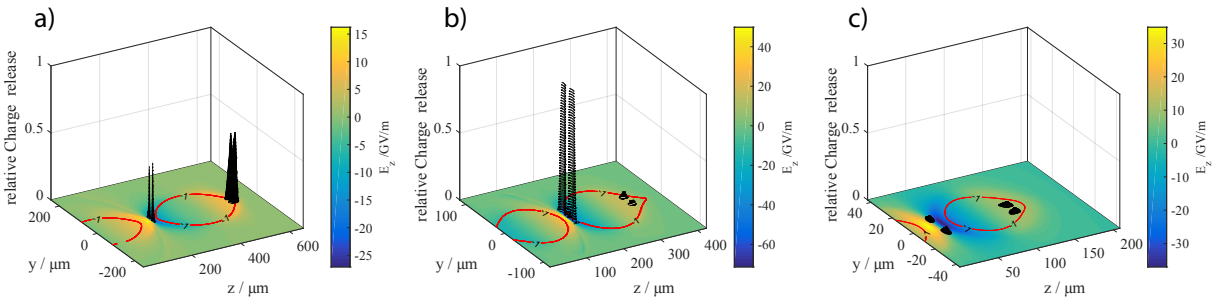

Figure 2.13: Charge release calculated from ADK rates for different simulation parameters. a) Drive beam charge $Q = 3\,\mathrm{nC}$, $\lambda_p = 333\,\mu\mathrm{m}$, $\sigma_z = 25\,\mu\mathrm{m}$, $\sigma_r = 7\,\mu\mathrm{m}$. b) $Q = 3\,\mathrm{nC}$, $\lambda_p = 149\,\mu\mathrm{m}$, $\sigma_z = 25\,\mu\mathrm{m}$ $\sigma_r = 7\,\mu\mathrm{m}$ c) $Q = 1.1\,\mathrm{nC}$, $\lambda_p = 100\,\mu\mathrm{m}$, $\sigma_z = \sigma_r = 14.1\,\mu\mathrm{m}$. Images are generated by the author from simulation data carried out for reference [10].

The reduction of hot spots by altering the plasma wavelength and the electron bunch properties are presented in figure 2.13. The three images show snapshots of PIC simulations with a transverse cut through the longitudinal electric field E_z (color coded). The limit of the trapping region is drawn as a red line and the longitudinal derivative of the ionization rate normalized

by the final ionization ratio as black peaks, calculated from ADK rates (see equation 2.49). The assumed gas mixture consists of fully ionized hydrogen plasma with gaseous He at half the hydrogen gas density. Figure 2.13 b) shows the simulation of a 3 nC FACET-like driver bunch with sizes $\sigma_r = 25\,\mu\mathrm{m}$ and $\sigma_z = 7\,\mu\mathrm{m}$ driving a plasma wake in the blowout regime in a plasma of wavelength $\lambda_p = 149\,\mu\mathrm{m}$. Here, the drive beam ionizes He, but the predominant He-ionization is due to the fields at the back of the wake. However, the ionization at the back of the wake in this simulation begins at the border of the trapping region. Figure 2.13 a) shows the situation for the same drive beam, but at $\lambda_p = 333\,\mu\mathrm{m}$. The wake-induced ionization is greatly diminished, but the driver ionizes more strongly due to more efficient drive-beam pinching in the transverse focusing fields. Figure 2.13 c) demonstrates the effect of a drive-beam charge decreased to $Q = 1.1$ nC with a round beam of $\sigma_r = \sigma_z = 14.4\,\mu\mathrm{m}$. Dark Current from electron-bunch-induced ionization injection as well as from wake-induced ionization injection is very low. Such an environment is a good starting point for Trojan Horse PWFA as it ensures a clean witness-bunch formation, which of course comes at the cost of a reduced available accelerating field. How the underdense photocathode can be applied even for comparatively weak driver bunches is treated in chapter 4.

3

TRAPPING BEHAVIOR FOR THE TROJAN HORSE PWFA ELECTRON INJECTION

We saw in section 2.7.1 that the length and position of the released electron bunch as well as the accelerating gradient play a significant role in establishing an effective velocity bunching. In the Trojan Horse injection concept, the wakefield formation is completely decoupled from the witness-bunch injection. This makes it in principle possible to inject electrons at a phase and transverse wake position of choice. We want to examine now what kind of initial and final electron bunch distributions we can expect. Hence, one needs to combine the 1D ionization physics from section 2.3 with the 1D trapping theory from section 2.7. The parameters that determine the current profile of the witness bunch are then important to understand the results presented in chapter 4.

3.1 BUNCH COMPRESSION

The transverse release position of the witness-bunch electrons can and often should be chosen to be situated in the transverse center of the blowout where the focusing forces are symmetric. From the Panowsky-Wenzel Theorem (equation 2.70) it can be concluded that the accelerating field is constant in the radial direction and the focusing force is constant in the longitudinal direction, as seen in figure 2.5 and 2.4. Hence, for an electron-bunch release in a volume which is small compared to the size of the plasma wake and situated in the radial center of the wake, a 1D treatment of the longitudinal witness-bunch formation is sufficiently accurate. Figure 3.1 demonstrates the time-dependent ionization ratio in He during the propagation of a 100 fs long laser pulse with peak intensity $1 \times 10^{15} \frac{\mathrm{W}}{\mathrm{cm}^2}$, according to equation 2.52. The ionization front (red) is clearly visible as a rapid increase of the ionization ratio.

The calculations are carried out with the electric field of the laser assumed in the envelope equation 2.51. In the strongly ionizing regime considered here, in which the laser ionizes a large percentage of the gas, the form of the ionization front calculated by a fully resolved laser pulse is in good agreement with the result applying the envelope equation.

The form of the ionization front is also in good agreement with experimental data: in reference [96], the structure of the ionization front of short-pulse lasers in He has been measured with single-shot supercontinuum spectral interferometry by using a well-known chirped low-intensity probe laser pulse co-propagating with the ionizing laser pulse. Interferometry of the spectrally dispersed probe pulse then revealed the length of the ionization front. These results

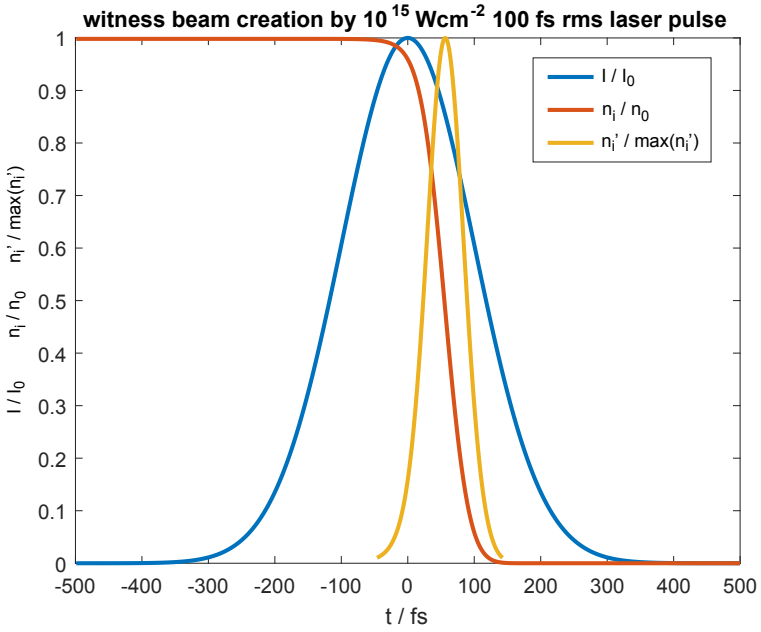

Figure 3.1: Ionization front (red) and derivative of ionization front (yellow), i.e. the initial witness bunch current distribution, from an 100 fs rms ultra-short laser pulse with peak intensity of $I_0 = 10^{15}\,\mathrm{W/cm^2}$. All graphs are normalized to their maximum value to emphasize their longitudinal/temporal relation.

have demonstrated a very good agreement with the ionization front as predicted by the ADK formalism.

The form of the ionization front given by equation 2.49 is very important to the process of the witness-bunch generation. From the derivative of the ionization ratio one can calculate the form of the initial witness-bunch electron distribution during the release. The initial electron release distribution in the co-moving frame at given position in cylindrical coordinates r, z is

$$f_\mathrm{i}(\xi, r, z) = -\frac{d}{d\xi}\frac{n_\mathrm{e}(\xi, r, z)}{n_0} \tag{3.1}$$

$$= -\frac{d}{d\xi}\left(1 - \exp\left(-\int_\infty^\xi W_\mathrm{ADK}(E_\perp(\xi', r, z,))d\xi'\right)\right) \tag{3.2}$$

$$= \frac{d}{d\xi}\exp\left(-\int_\infty^\xi W_\mathrm{ADK}(E_\perp(\xi', r, z))d\xi'\right). \tag{3.3}$$

Here, the electric field of the laser pulse is assumed to have linear polarization, i.e. perpendicular to the propagation direction z.

When analyzing the ionization behavior as shown in figure 3.1, two details of the ionization front are important to notice:

- The length of the ionization front and hence the initial release is much shorter than the actual laser pulse.
- The center of the released electron distribution does not need to coincide with the peak of the laser-pulse intensity profile.

In order to calculate a final witness-bunch distribution from the initial release distribution, the trapping formalism as described in section 2.7 needs to be applied. Equation 2.127 can be reorganized to

$$\xi_i = \sqrt{\xi_f^2 + \alpha_t}. \tag{3.4}$$

This gives the relation between the initial release position ξ_i and the final trapping position ξ_f of an electron released at rest in the co-moving frame for an accelerating field approximated to be linear. Causality only allow solutions with $\xi_\mathrm{f} < 0$. Therefore, ξ_f has negative solutions only, which means that trapping can only occur at the back of the wake.

We will now treat the trapping of a distribution of charge instead of a single electron. This finding can than be used to calculate the longitudinal compression of a released electron bunch during the trapping. For that we consider the initial release distribution as a one-dimensional Gaussian distribution

$$f_\mathrm{i}(\xi) = \frac{1}{\sigma_\xi\sqrt{2\pi}} e^{-\frac{(\xi+\delta_\xi)^2}{2\sigma_\xi^2}} \tag{3.5}$$

with rms width σ_ξ. This is a good approximation, as can be seen in figure 3.1. The distribution should be normalized to

$$\int_{-\infty}^{\infty} f_\mathrm{i}(\xi) d\xi \stackrel{!}{=} 1. \tag{3.6}$$

Equation 3.5 is now the initial released electron beam and can, by applying equation 2.127, be used to calculate the trapped electron beam distribution

$$f_\mathrm{f}(\xi) = f(\xi_\mathrm{i}(\xi_\mathrm{f}))\left|\frac{\partial\xi_\mathrm{f}}{\partial\xi_\mathrm{i}}\right| \tag{3.7}$$

$$= \frac{1}{\sigma_\xi\sqrt{2\pi}} e^{-\frac{(\xi_\mathrm{i}+\delta_\xi)^2}{2\sigma_\xi^2}} \left|\frac{\xi_\mathrm{i}}{\sqrt{\xi_\mathrm{i}^2+\alpha_\mathrm{t}}}\right| \tag{3.8}$$

$$= \frac{1}{\sigma_\xi\sqrt{2\pi}} e^{-\frac{(\sqrt{\xi_\mathrm{f}^2-\alpha_\mathrm{t}}+\delta_\xi)^2}{2\sigma_\xi^2}} \left|\frac{\sqrt{\xi_\mathrm{f}^2-\alpha_\mathrm{t}}}{\sqrt{\xi_\mathrm{f}^2-\alpha_\mathrm{t}+\alpha_\mathrm{t}}}\right| \tag{3.9}$$

$$= \frac{1}{\sigma_\xi\sqrt{2\pi}} e^{-\frac{(\sqrt{\xi_\mathrm{f}^2-\alpha_\mathrm{t}}+\delta_\xi)^2}{2\sigma_\xi^2}} \left|\frac{\sqrt{\xi_\mathrm{f}^2-\alpha_\mathrm{t}}}{\xi_\mathrm{f}}\right| \tag{3.10}$$

$$= \frac{1}{\sigma_\xi\sqrt{2\pi}} e^{-\frac{(\sqrt{\xi_\mathrm{f}^2-\alpha_\mathrm{t}}+\delta_\xi)^2}{2\sigma_\xi^2}} \left|\sqrt{1-\frac{\alpha_\mathrm{t}}{\xi_\mathrm{f}^2}}\right|. \tag{3.11}$$

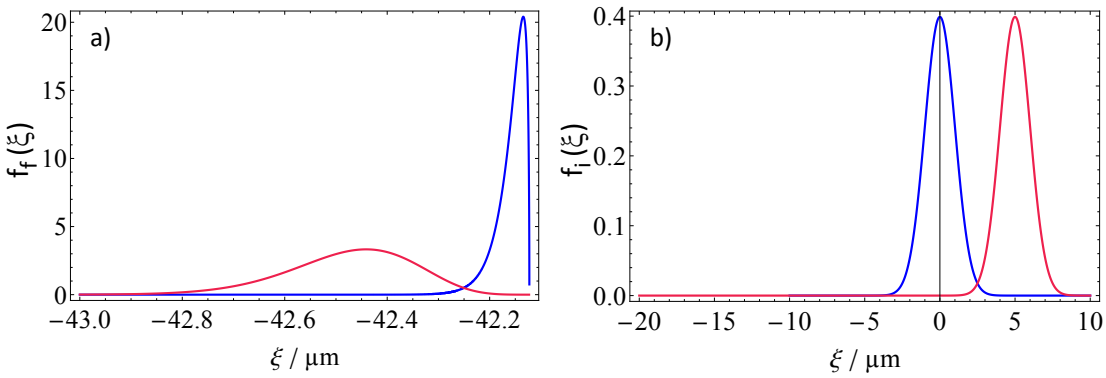

Figure 3.2: Trapped longitudinal electron density distribution (a) calculated with equation 3.11 for an initial release density distribution (b) in the wake zero-crossing (blue) and with a 5 μm offset (red) for a plasma density of $n_e = 1 \times 10^{17}\,\mathrm{cm}^{-3}$. The release distributions shown in b) are identical and differ only in the longitudinal offset.

This solution also requires the normalization

$$\int_{-\infty}^{0} f_f(\xi) d\xi \stackrel{!}{=} 1 \tag{3.12}$$

to ensure the conservation of charge from release to trapping. In contrast to the normalization of equation 3.6, equation 3.12 is integrated from $-\infty$ to 0 because trapping is only possible at positions $\xi_f < 0$. An example of equation 3.11 can be seen in figure 3.2. The calculations illustrate the effect of velocity bunching in ionization injection. The strongest compression is achieved if the electron bunch is released at the potential minimum, which is at the zero crossing of the accelerating electric field as illustrated in figure 2.8. An elegant way to produce such a bunch of released electrons is to use a laser pulse focused at this zero-crossing point, since no wakefield-ionized electrons are produced in this region of zero electric field. This can be achieved with the Trojan Horse Injection method.

The bunch compression depending on the release position is illustrated with 3D PIC simulation results shown in figure 3.3. A 2 nC drive beam with bunch dimensions $\sigma_r = 17.7\,\mu$m and $\sigma_z = 40\,\mu$m drives a wake in a plasma density of $n_e = 4.6 \times 10^{15}\,\mathrm{cm}^{-3}$, which corresponds to a plasma wavelength of $\lambda_p \approx 500\,\mu$m. The laser-pulse length is $\tau = 20$ fs with a focal waist of $w_0 = 6\,\mu$m and a peak intensity of $I_0 = 7 \times 10^{14}\,\mathrm{Wcm}^{-2}$. The current profile of the trapped witness bunches for different injection phases is plotted (dashed lines) and compared to the analytic model (thick lines). The analytic model fits best for a release at $\xi_i = 0\,\mu$m and $\xi_i = -29\,\mu$m. The analytic model shows a slightly different trapping position for the release position $\xi_i = -50\,\mu$m because the accelerating field in the simulation increases more rapidly at the back of the wake than in the linear approximation (see figure 2.4). The initial release

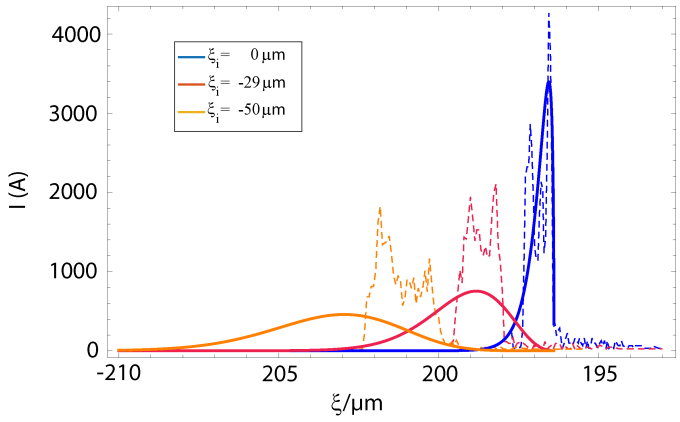

Figure 3.3: 3D PIC simulation of a compressed witness-bunch longitudinal current distribution after Trojan Horse Injection (dashed lines) compared with analytic model (thick lines). Position $\xi_i = 0\,\mu m$ (blue) corresponds to a release at the potential minimum. The fluctuations are caused by resolution effects in the simulation.

bunch length is set to $\sigma_\xi = 8\,\mu m$ and was used as a free parameter to best fit the simulation data. However, evaluating equation 3.3 gives a value of only $\sigma_\xi = 2.5\,\mu m$.

This disparity can be explained by considering the complete propagation of a 3D resolved laser-pulse during the injection process.

During the focusing of the ionization laser in direction z, its intensity increases, which causes the ionization front to change in length $\sigma_{\tilde{\xi}}$ and position with respect to the laser pulse intensity maximum $\delta_{\tilde{\xi}}$. Moreover, both parameters can also change in transverse direction r because the intensity is highest in the radial center of the Gaussian laser. These variations in intensity increase the release length of the witness bunch in the plasma wake and consequently increase the bunch length of the trapped bunch which leads to a decreased peak current.

However, At low laser intensities, which occur transversely outside the axis at position r, and before and after the laser focus in the lab frame the HIT medium is not ionized anymore so that no charge is contributed to the witness bunch. This section summarizes these effects that influence the length of the trapped witness bunch.

The injection-laser intensity distribution in cylindrical coordinates is

$$I_0^{\text{temp.}}(r,z) = I_0 \frac{w_0^2}{w(z)^2} \exp(-2\frac{r^2}{w(z)^2}), \tag{3.13}$$

where $w(z)$ is the laser spot size (see also equation 2.51). For every temporal peak intensity, equation 3.3 calculates an initial release distribution $f_{\text{i}}(\tilde{\xi},r,z,t)$ with a release length $\sigma_{\tilde{\xi}}$ and offset $\delta_{\tilde{\xi}}$. To obtain the full witness-bunch current distribution, the integral

$$f_{\text{i}}(\tilde{\xi}) = 2\pi \int_0^\infty r dr \int_0^\infty dz f_{\text{i}}(\tilde{\xi},r,z) \tag{3.14}$$

needs to be evaluated, where $f_{\text{i}}(\tilde{\xi},r,z)$ is weighted by the final ionization ratio $\lim_{\tilde{\xi}\to\infty} \frac{n_{\text{e}}(\tilde{\xi})}{n_0}$ after the passage of the laser pulse. Figure 3.4 shows the result of the numerical analysis of the ionization front, ionizing He to He^+. The laser pulse is assumed to be Gaussian with a wavelength of 800 nm. The contour plot shows the longitudinal rms length of the ionization front as calculated with equation 3.3 as a function of the laser pulse length and temporal peak intensity (a). The calculation of the contour plot (a) does not take into account the fact that the intensities do not necessarily lead to full ionization, which explains the increasing values towards low intensities and long pulse lengths in the weakly ionizing regime. In this regime, the ionization front is not a sharp sigmoid function, but instead, there is continuous ionization over the length of the laser pulse, leading to a large initial witness-bunch phase distribution. Contour plot (b) shows how intensity and pulse length influence the longitudinal offset $\delta_{\tilde{\xi}}$ of the witness beam release peak with respect to the laser-pulse center. As long as the offset is constant for all the released charge, this does not contribute to an additional broadening of the initial bunch distribution; however, a correct analysis should consider the focusing and defocusing as well as the transverse intensity distribution of the laser pulse. In order to translate that into meaningful information on witness-bunch formation, the contributing intensities at a given pulse length need to be weighted by the final witness-bunch charge contributed to by each intensity value. This is plotted in red in the contour plot in figure 3.4 a) and b). A 800 nm laser

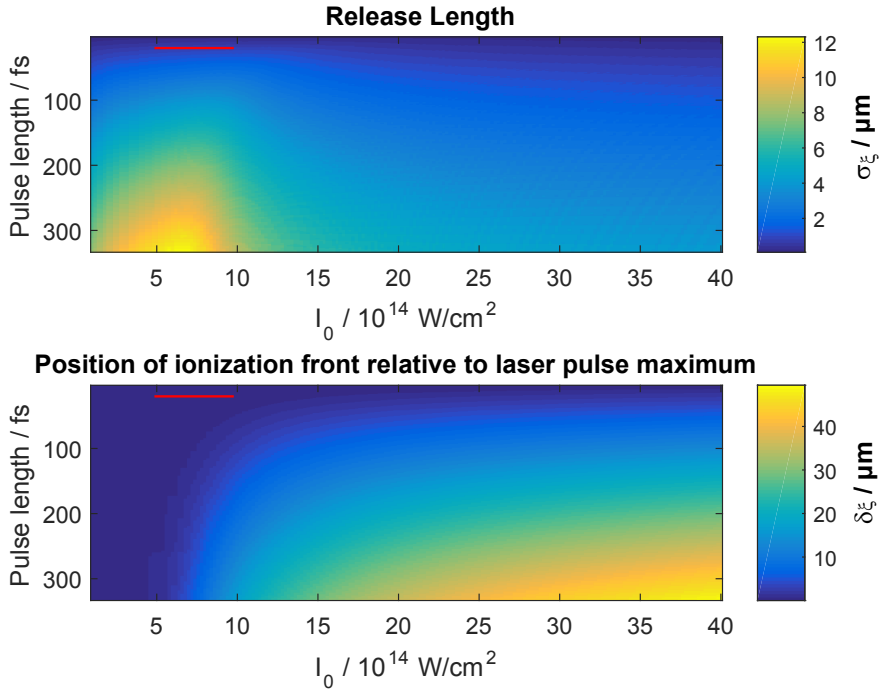

Figure 3.4: Variation of rms electron beam release length calculated from the derivative of the ionization front (a) and peak electron release position relative to peak laser intensity (b) as a function of laser peak intensity and FWHM pulse length. The red line shows the part of the intensity distribution of a Gaussian Laser Pulse with peak intensity $1 \times 10^{15}\,\mathrm{W/cm^2}$, $w_0 = 6\,\mu\mathrm{m}$ and pulse length of 20 fs that contributes to the witness-bunch charge.

pulse with $w_0 = 6\,\mu\mathrm{m}$, peak intensity of $1 \times 10^{15}\,\mathrm{W/cm^2}$ and pulse length of 20 fs is assumed. The red line marks those intensities that contribute at least 10 % of the total witness-bunch charge.

This analysis helps to choose the parameters of the Trojan Horse Injection laser. To optimize the laser parameters for short witness bunches, the length of the red line should overlap with low values for the release length in inset a) and overlap with a small range of values $\delta\xi$ in inset b). Both contour plots confirm that the choice of laser parameters is already well suited for minimizing initial phase spread and hence witness bunch length because the release length is comparatively small and there is little change in release position during the injection.

Another way to optimize Trojan Horse injection for short witness bunches is to generate a narrow intensity distribution during the injection process, which means a short red line in figure 3.4. While Gaussian focussing might be somewhat limited, this can be achieved by designing optical focusing elements that generate a line focus such as e.g. an axicon [97].

4

DOWNRAMP ASSISTED TROJAN HORSE PWFA

MOTIVATION FOR PHASE-VELOCITY RETARDATION

As discussed in section 2.8.5, the underdense photocathode or Trojan Horse PWFA is an exceptional method for generating short ultra-low-emittance high-brightness relativistic electron bunches. Such bunches, if transported without quality loss, can open up a variety of new applications. However, as for all ionization-injection schemes, witness-beam electrons are released in the wake at rest, which requires a trapping potential $\bar{\Psi} < -1$ (see section 2.7), so even in the blowout regime, very strong wakefields are required. This, in turn, needs a short electron drive bunch with a high peak current. As will be shown in section 10, for a FLASHForward-class electron drive bunch, a peak current of at least 6 kA is necessary to enable Trojan Horse Injection. On the other hand, in section 2.8.6 it is shown that a low peak-current can be advantageous to avoid dark current.

In table 4.1, a list of future PWFA facilities with expected beam specification is provided. All of the listed facilities plan to engage in Trojan Horse PWFA acceleration, but only FACET II will provide high-peak-current bunches. Hence, these facilities will have to investigate and invest in further compression of the drive bunch, or a solution from the plasma side needs to be found.

Facility	Energy (GeV)	Maximum beam charge (nC)	Peak current (kA)
FLASHForward	1.25	0.5	2.5
CLARA	0.25	0.1	1
FACET II	10	5	≤ 50
ATF II	0.5	0.3	>1.5

Table 4.1: List of upcoming PWFA research facilities and their electron beam specifications. Values are taken form references [78],[98],[99] and [100].

The aim of this chapter is to present a solution to the challenge of how a facility with a few-kA electron beam can conduct Trojan Horse PWFA research. We make a virtue out of necessity and start immediately with a driver with low peak current. In order to establish clean Trojan Horse Injection, an intermediate state needs to be found between a strong wake with a trapping potential $\bar{\Psi} < -1$ and a wake that is too strong, thereby ionizing He either from the drive beam or the wake.

Assuming a comparably weak drive bunch, the author presents an alternative approach, i.e. to

facilitate the trapping by changing the evolution of the accelerating field of the plasma wake. As presented in section 2.7, a decrease in wake phase velocity with gamma factor γ_ϕ leads to a trapping condition of the form

$$\Delta\Psi = \gamma_\phi^{-1} - 1. \tag{4.1}$$

In an infinite homogeneous plasma, the wake's phase velocity is equal to the drive-bunch velocity

$$\beta_\phi = \beta_{\text{beam}} \approx 1. \tag{4.2}$$

Beams with low momentum could be used to decrease the phase velocity, but such low-γ beams would be depleted or explode due to intra-beam Coulomb self fields before the witness bunch reaches relativistic energy due to the strong decelerating field in the plasma wake (see section 2.8.). Consequently, manipulation of the plasma response to the wake excitation is the best strategy to decrease the phase velocity. Fubiani et al. [101] have proposed a smooth density downramp, lowering the trapping threshold. The implications of this Downramp-assisted Trojan Horse (DTH) for the possible generated witness bunches is investigated in this chapter.

THE DOWNRAMP-ASSISTED TROJAN HORSE (DTH) SETUP

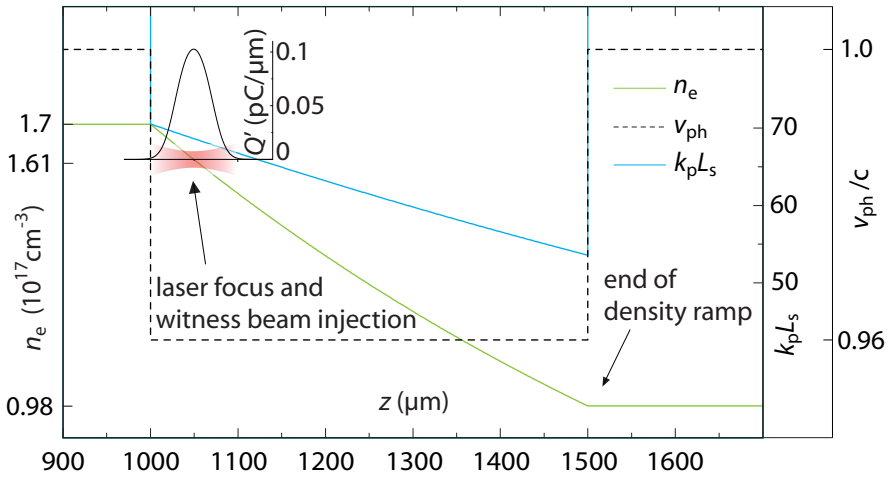

Figure 4.1: Suggested Injection method. A smooth exponential density downramp with $C_{\text{ramp}} = 1.1\,\text{mm}^{-1}$(green), the corresponding product of the inverse skin depth and the density transition scale length $k_\text{p}L_\text{s}$ (blue) and the phase velocity at $\xi_{\text{tr}} = -70\,\mu\text{m}$ behind the drive beam are plotted. The Trojan Horse injection laser is focused at $z = 1050\,\mu\text{m}$ and releases a longitudinal charge density Q' during the injection.

A possible hydrodynamic density downramp is shown in figure 4.1, which is also the guideline for the simulations. A smooth density downramp with a total length of $500\,\mu\text{m}$ decreases exponentially from an electron density $n_\text{e} = 1.7 \times 10^{17}\text{cm}^{-3}$ to $0.98 \times 10^{17}\text{cm}^{-3}$ in the direction of the electron-beam propagation, z. An exponential density profile (green) is chosen, because

of its similarity to realistic hydrodynamic shapes (superior to ramps assumed to be linear) and secondly, because analytic calculations become easier. On a density ramp with upper plateau plasma density n_e^i and ramp gradient constant C_{ramp}, the profile is

$$n_e(z) = n_e^i e^{-C_{ramp} z} \tag{4.3}$$

with a phase velocity according to equation 2.144

$$v_\phi(\xi) = c \left(1 + \frac{1}{2} C_{ramp} \xi\right)^{-1}. \tag{4.4}$$

The phase velocity expressed in terms of the relativistic gamma factor is

$$\gamma_\phi = \frac{1}{\sqrt{1-\beta_\phi}} = \left(\sqrt{1 - \left(\frac{1}{1 + (1/2) C_{ramp} \xi}\right)^2}\right)^{-1}. \tag{4.5}$$

Equation 4.5 depends only on ξ and not explicitly on z. In figure 4.1, this can clearly be seen in the graph depicting the phase velocity at $\xi_{tr} = -70\,\mu\mathrm{m}$ behind the drive beam. Also the product $k_p L_s$, with $L_s = n_e(z)/n_e'(z)$ is plotted and ranges between $50 - 70 \ll 1$. For such values, injection into the first bucket due to density-downramp injection should not be possible, which is also confirmed with PIC simulations (see figure 4.5).

Such smooth density downramps can be generated e.g. by a gas cell with a controlled flow [102, 103]. Particularly the option of controlling the downramp gradient mentioned by Kononenko et al. [102] is interesting as it can be used to remotely alter the phase velocity.

The described downramp and injection method was tested in a 3D PIC simulation. The driver bunch is assumed to be spatially Gaussian with a transverse rms size of $7\,\mu\mathrm{m}$ and an rms bunch length of $\sigma_z = 20\,\mu\mathrm{m}$. The laser is focused at the logitudinal position $z = 1050\,\mu\mathrm{m}$, where the resonance condition $k_p \sigma_z \approx \sqrt{2}$ is fulfilled. The energy is $W_d = 250\ \mathrm{MeV}$ and the energy spread is $\frac{\Delta W_d}{W_d} \approx 1\%$. The witness bunch should be injected after the driver is compressed due to the focusing wakefields because the increased charge density of the drive bunch leads to a stronger wake. The efficiency of this compression depends on the drive-bunch emittance (see section 2.8), which was set to $\epsilon_{n,rms}^d \approx 6.0 \times 10^{-6}\,\mathrm{mrad}$.

In a simulation study, a minimum drive-bunch charge of $Q_d = 500\ \mathrm{pC}$ at which reliable injection is still possible has been determined. This corresponds to a drive-bunch peak current of $I_d \approx 2\,\mathrm{kA}$ and a dimensionless beam charge $\tilde{Q} = 0.66$ at resonant electron density. We can reason that the driven wake is not strongly nonlinear because the condition for the blowout regime $\tilde{Q} > 1$ is not fulfilled. Snapshots of the simulation at these parameters are shown in figure 4.5.

The trapping potential is not exceeded either on the high-density plateau before the downramp (figure 4.5 a) with a minimum trapping potential of $\Delta\bar{\Psi}_{min} = -0.90$ or on the low-density plateau after the downramp (figure (4.5 c) at a minimum trapping potential of $\Delta\bar{\Psi}_{min} = -0.82$. This means that injection of laser-released witness beams as well as dark current from wake-

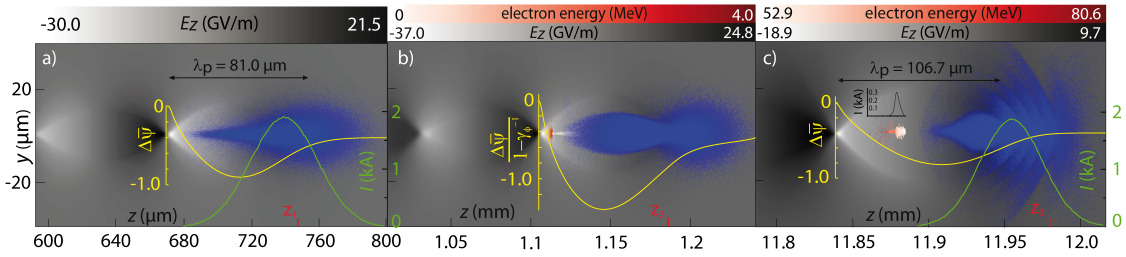

Figure 4.2: Snapshots of 3D PIC simulation at different time steps with a slice through the longitudinal electric field with the projected drive-bunch electrons (blue) and a central on-axis cut of the trapping potential (yellow) before the downramp (a), on the downramp (b) and after the downramp (c). The witness-bunch electron macro-particles injected on the downramp (b) are color-coded by their kinetic energy and remain trapped in the wake even after the downramp (c).

or beam-ionization is impossible outside the downramp region. Such a restriction is experimentally very valuable, because it ensures a clean injection. However, on the downramp the trapping potential

$$\Delta\bar{\Psi} = \sqrt{1 - \left(\frac{1}{1 + (1/2)C_{\mathrm{ramp}}\xi}\right)^2} - 1 \tag{4.6}$$

is significantly lowered to a minimum value of

$$\min\left(\frac{\Delta\bar{\Psi}}{1-\gamma_\phi^{-1}}\right) \approx -1.4 \tag{4.7}$$

so that the trapping condition is fulfilled (see figure 4.5 b). Figure 4.5 b) shows the simulation during the helium ionization by the laser pulse, and the trapping process. The injection laser pulse with a normalized vector potential $a_0 = 0.025$ and a pulse length $\tau = 40$ fs is defined in the envelope equation 2.51 and is sufficiently intense to ionize He. The released electrons are trapped if they reach the wake's phase velocity. During the continuous release of witness-bunch electrons, the trapping position ξ_{tr} keeps falling back in the co-moving frame due to the increasing longitudinal wake size.

To substantiate the claim of suppressed injection outside the downramp region, a simulation with a plasma at resonant density was performed. The result is shown in figure 4.3 and is unambiguous: all charge is lost without a density downramp and nearly all charge is trapped if injected on the downramp.

4.1 WITNESS-BUNCH EVOLUTION

Figure 4.4 shows the evolution of witness-bunch properties during its acceleration in the plasma wake. The snapshots of the PIC simulation shown in figure 4.2 are taken at different lab-frame

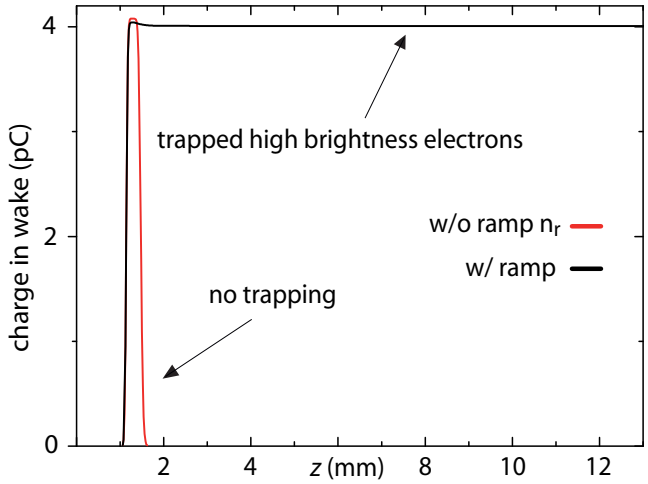

Figure 4.3: Charge inside plasma wake during propagation as calculated by PIC simulation of TH injection on a density downramp as described in figure 4.1 (black) and with a flat plasma profile at resonant density $n_e = 1.61 \times 10^{17}\,\mathrm{cm}^{-3}$ (red).

coordinates $z_1 - z_3$ marked in figure 4.4. After the downramp (green area) the wakefield does not continue to fall back in ξ with respect to the drive bunch and the witness bunch is accelerated by a constant mean electric field $E_z(\xi_{acc.}) \approx 5.8\,\mathrm{GV/m}$. In $z_{acc.} \approx 10\,\mathrm{mm}$, the witness beam gains energy from the wake to $W = q_e E_z(\xi_{acc.}) \approx 58\,\mathrm{MeV}$, with a relative rms energy spread of $\frac{\Delta W}{W} \approx 6.8\%$. The emittance and brightness evolution show signs of phase mixing and eventually reach values of $\epsilon_{n,rms} \approx 4.1 \times 10^{-8}\,\mathrm{m\,rad}$ and a peak brightness of $B = \frac{2I_p}{\epsilon_{n,rms}^2} \approx 3.2 \times 10^{17}\,\mathrm{Am^{-2}rad^{-2}}$. Even though the expanding wake promotes phase mixing, ultra-low emittance values $\epsilon_{n,rms} < 10^{-7}\,\mathrm{m\,rad}$, typical for the Trojan Horse injection are reached. The slightly lower brightness compared to conventional Trojan Horse PWFA simulations is solely due to the witness-beam elongation caused by the expanding wake.

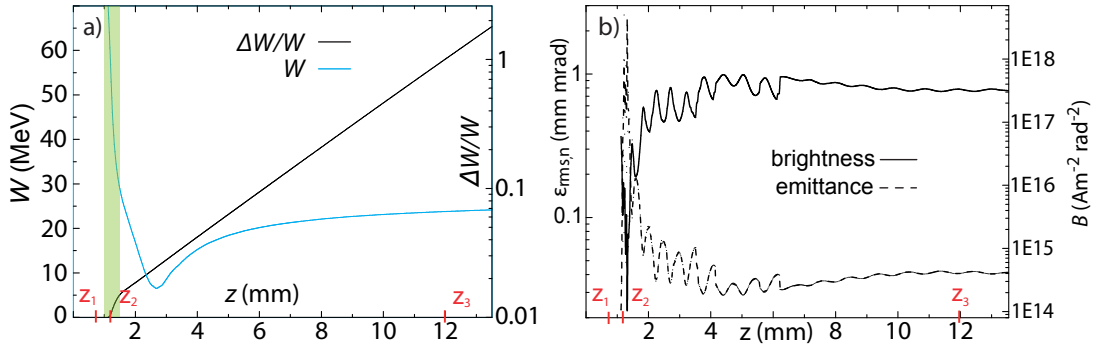

Figure 4.4: Evolution of witness-bunch parameters during acceleration in the plasma wake, plotted over acceleration length z. The witness-bunch energy (black), and energy spread (blue) are plotted in part a). The green area represents the extent of the density downramp. Normalized trace-space emittance (black, solid line) and brightness (black, dashed line) are plotted in part b). After initial phase mixing, the normalized trace-space emittance remains $< 10^{-7}$ m rad.

4.2 LONGITUDINAL PHASE SPACE

The witness bunch is not compromised by any kind of dark current. The drive-bunch electric fields and wakefields release a total charge of only 13 fC from helium, which is not even trapped. The suppression of dark current from downramp injection as indicated by the calculated high values of $k_p L_s$ (figure 4.1) is confirmed by PIC simulations. Figure 4.5 shows longitudinal phase-space scatter plots for the low-energy background plasma-electron macro particles (a) and the high-energy injected witness-bunch-electron macro particles (b) after $\approx$ 12 mm propagation in plasma.

The background plasma electron distribution has a typical form (compare e.g. reference [76]) with highest energies at the blowout vertex corresponding to a velocity of $\beta_\phi \approx 0.63$, far below the phase velocity. No high-energy electron population is visible which confirms that no charge has been accelerated from downramp injection. In contrast to the Trojan Horse scheme, in DTH, the continuous variation of the trapping position leads to a chirp so that the correlated energy spread is large. The uncorrelated slice-energy spread, however, is much smaller. Such energy spreads can be minimized by an advanced dechirping method that rotates the longitudinal phase space, such as the dechirper bunch concept presented in reference [104]. It suggests injecting a second high-charge bunch into the blowout that escorts the low-emittance witness bunch. The escort bunch loads the wake so strongly that the accelerating field flips sign and rotates the longitudinal phase space of the witness bunch such that its energy spread is minimized.

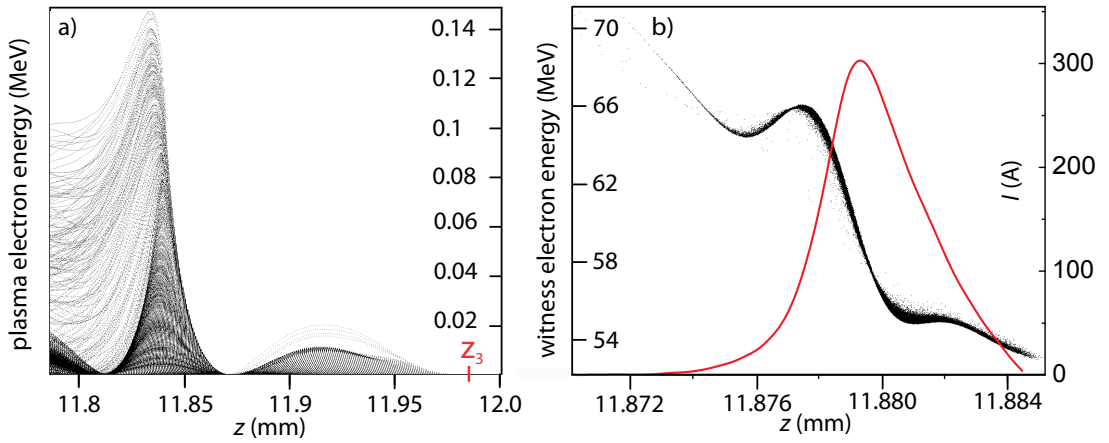

Figure 4.5: Scatter plots of longitudinal phase-space distribution after $\approx$ 10 mm witness-beam acceleration. The background plasma electron distribution (a) shows no sign of injected charge, which means that no downramp injection occurred. The laser-ionized electron bunch is elongated and shows an approximately Gaussian current distribution with 300 A peak current (b, red plot). The kinks in the longitudinal phase space of the witness bunch (b) are likely to originate from Numerical Cherenkov Radiation.

4.3 LONGITUDINAL WITNESS-BUNCH SHAPING

In the case of Trojan Horse Injection, the witness bunch can be of sub-μm-length, as described in section 3.1. The simulations show that the witness bunches generated with the DTH method, however, can be several μm long. While for TH the injection position and movement of the ionization front determine the bunch length, for DTH, the witness-bunch length is dominated by the expansion of the plasma wake on the density downramp. The continuous release of charge into an elongating wake results in an elongated electron bunch.

A detailed analysis of simulations reveals that electron macroparticles released first (before the laser focus) are trapped at higher ξ-values than electron macroparticles released later (e.g. after the laser focus). The bunch-lengthening effect by the wake expansion is described by the increase of the plasma wavelength between the starting point of the FWHM laser release z_1' and the end point z_2' with $\Delta z = z_2' - z_1'$. A Taylor series expansion around $\Delta z \ll 1$ brings about the scaling for the FWHM bunch length

$$\sigma_w \approx \Delta\lambda_p \approx (2\pi c/e)\sqrt{\epsilon_0 m_0/n_e}(C_r \Delta z). \tag{4.8}$$

The proportionality to the ramp constant C_{ramp} was tested systematically in simulations and the results are plotted in figure 4.6. A number of ramp profiles with different downramp constants (red, yellow, green, blue) and their density profiles are plotted in (a) and (b), which show the resulting witness-bunch current profiles in the same color coding. Additionally the

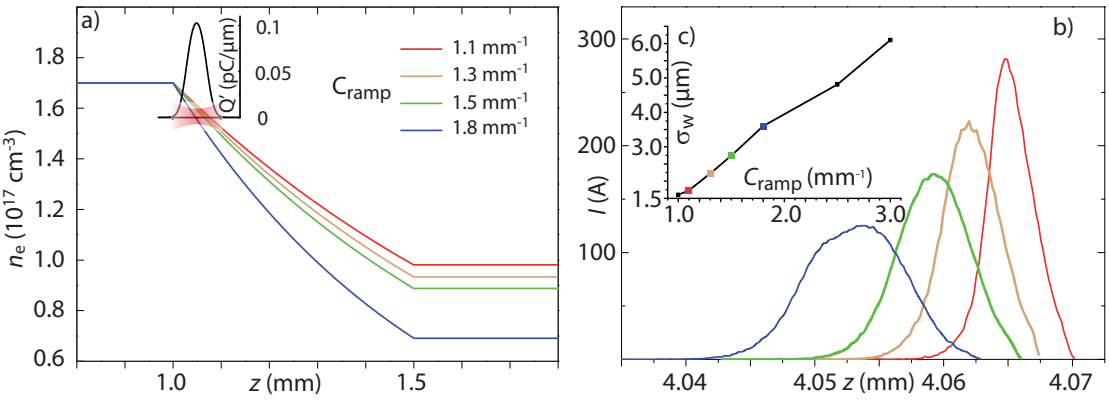

Figure 4.6: Control over Witness-bunch current profile via density-downramp gradient: DTH is simulated for downramps with different constants. a) shows the ramp density profiles and the longitudinally resolved charge release by the laser pulse. In b) the resulting witness-bunch profiles are shown. Inset c) confirms the linear dependence predicted by equation 4.8.

rms bunch-length values from the color coded ramps and other values are given as a function of C_{ramp} in (c), which confirms the linearity predicted by equation 4.8. The witness-bunch profile is a convolution of the longitudinal charge released during the laser focusing Q' and the trapping response function 3.11. For small values of C_{ramp}, the structure of the response function still has a visible effect, as for example can be seen in the case of $C_{\text{ramp}} = 1.1\,\text{mm}^{-1}$. This can be illustrated by comparing figure 4.6 b) with figure 3.2. For larger values such as $C_{\text{ramp}} = 1.8\,\text{mm}^{-1}$, the response function becomes effectively a delta function and the form of Q' dominates the form of the current profile.

Witness-bunch-length control over a range between $1.5\,\mu$m and $6.0\,\mu$m rms has been sucessfully demonstrated in simulations without electron-bunch quality loss in emittance, which means $\epsilon_{\text{n,rms}} < 10^{-7}\text{m rad}$ for all simulation results shown.

The witness bunch develops a Gaussian current profile, simply because the Gaussian focusing of the injection laser happens to produce a Gaussian-distributed charge release in z during the injection. However, a Gaussian focusing is only one among many possible methods of laser-focusing. In fact, it is possible with Fresnel plates to design a longitudinal intensity profile of choice and because the injection pulse only needs an energy of a few $100\,\mu$J, to a few mJ this can also be easily handled.

Simulations with alternative longitudinal peak-intensity profiles (figure 4.7 a) are applied in a simulation with $C_{\text{ramp}} = 1.1\,\text{mm}^{-1}$, so that the witness-bunch current profiles as calculated by simulation form a triangular shape. In figure 4.8 the same result is shown for a line focus with a transverse Gaussian profile of $w_0 = 3\,\mu$m. In agreement with the presented description, the trapped witness bunch develops a flat-top current profile during injection. Such laser foci are for example achievable with an axicon [97].

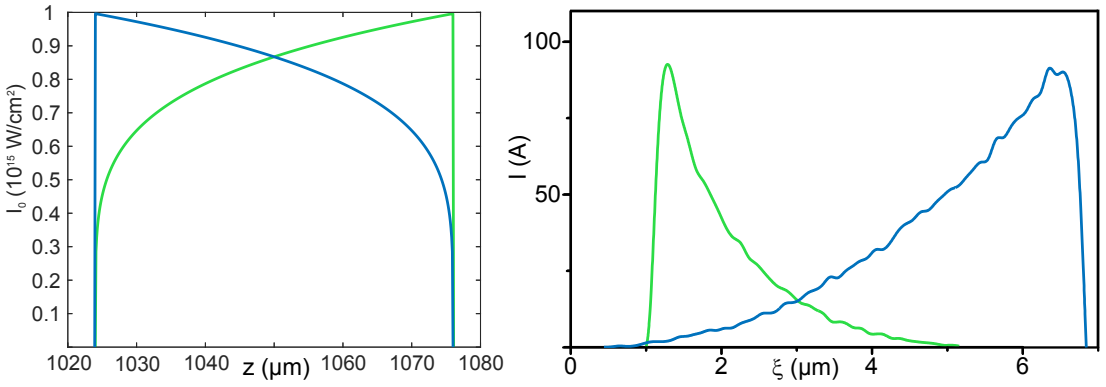

Figure 4.7: Current profiles from an injection laser with ramped intensity profile on density downramp.

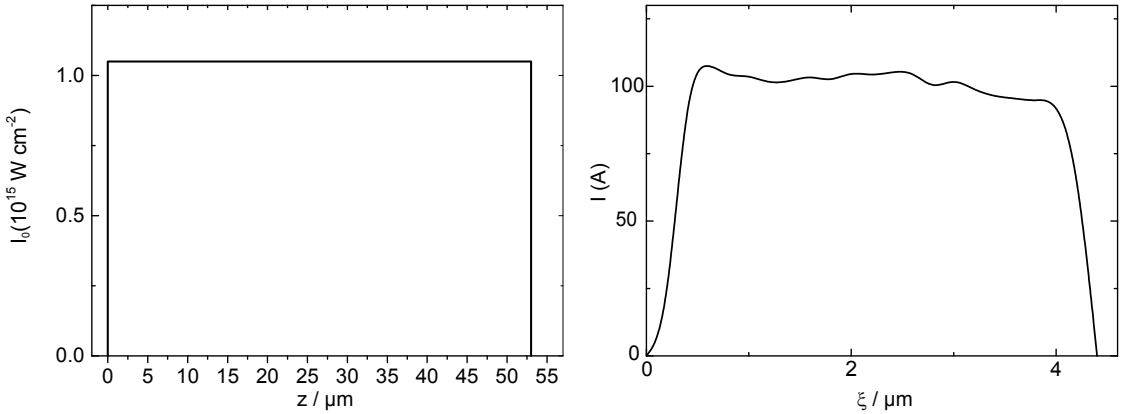

Figure 4.8: Current profile from line-focus injection on density downramp.

Controlling the density ramp to that degree is possible, even remotely controllable during accelerator beamtime, if specialized hydrodynamic gas cells[102] are utilized.
Trojan Horse Injection is a method that decouples the witness-bunch injection from the wake formation. Downramp-assisted Trojan Horse further decouples the bunch length, determined by the density ramp, from the witness-beam shape, which is determined by the longitudinal laser intensity profile.

5

THE E210 EXPERIMENTAL CAMPAIGN

In 2014, the experimental campaign for demonstrating the proof-of-concept of Trojan Horse injection (see 2.8.5), which is known as "E210: Trojan Horse PWFA" started at the Facility for Advanced Accelerator Experimental Tests (FACET) at the SLAC national laboratory. In this campaign, we worked in a collaborative effort with researchers from the University of Hamburg, University of California Los Angeles (UCLA), University of Strathclyde in Glasgow, the industry partners Radiabeam technology[1], Tech-X[2] and RadiaSoft[3] and with dedicated support from the SLAC personnel. All experiments that were conducted at FACET in overlapping beam-time periods had to be designed in a way that a change from one experiment to another can be accomplished remotely or with little effort. That way, in case one experiment needs maintenance, another can take over and continue measuring and no accelerator beam time is wasted. At FACET the different experimental setups had to pass several levels of maturity. This required constant adjustment of the overall FACET setup, which led to a fruitful joint learning process between several research groups.

It is fair to say that E210 was one of the most complex and most demanding experiments in terms of accuracy ever conducted at FACET [105]. Several steps were required to optimize the experimental setup until the experiment was eventually successful. The most crucial obstacles to overcome were timing and alignment between two laser arms and the electron beam. The timing requirements between the electron beam and the pre-ionization laser were rather undemanding as long as the pre-ionization occurred before the arrival of the electron beam, with a timing difference less then the recombination time (ps-ns range). However, proper control over the relative time-of-arrival (TOA) between the injection laser and the electron beam required - in principle - control over timing on the order of 10 fs. With an estimated timing jitter in the range of at least 73.2 fs rms (see section 7.1) sufficiently stable timing on a shot-to-shot basis was not possible. The best solution to cope with such a timing jitter was to accurately measure the relative time-of-arrival on every shot with electro-optical sampling (described in section 7.2) to determine the timing-dependent injection properties. To measure the synchronization (t_0) as well as fine alignment between the electron beam and the injection laser, a novel plasma-based method was developed, commissioned and applied. The method is based on plasma glow from recombination light as a result of the fs-scale-interaction signature and is described in section 7.3.

1 RadiaBeam Technologies, LLC www.radiabeam.com
2 Tech-X UK Ltd. www.txcorp.com
3 radiasoft.net

5.1 PWFA AT THE SLAC NATIONAL ACCELERATOR CENTER

Founded in 1962 as the Stanford Linear Accelerator Center and operational since 1966, SLAC has been ever since a landmark for excellence in science. The Nobel Prizes for 1976 for the discovery of the charm quark, for 1990 for the structure of quarks in protons and neutrons and for the discovery of the τ-Lepton in 1995 have been awarded for research conducted at the SLAC accelerators. In addition, a large variety of high-impact publications testify to the huge influence SLAC has on the research field of high-energy physics. In 2006, the Nobel Prize in Chemistry was awarded for "studies of the molecular basis of eukaryotic transcription" thanks to the data taken at the Stanford Synchrotron Radiation Lightsource (SSRL), a storage ring on the SLAC campus. The Nobel Prizes in Chemistry awarded in 2009 for deciphering the structure of the ribosome and in 2012 are also based on work that took place at the SSRL.

This shift of scientific success from high-energy physics to other fields of science was made possible due to the conversion of part of the SLAC Linac to a high-quality X-ray light source. The building of the Linear Coherent Light Source (LCLS), the world's first X-ray free-electron laser (FEL), emphasized this diversification of research focus. One third of the 3.2 km-long Linear Accelerator (Linac) tunnel of the Stanford Linear Collider (SLC) was converted to produce the LCLS electron beam, leaving room for the unique Facility for Advanced Accelerator Experimental Tests, FACET [72].

5.2 THE FACET LINEAR ACCELERATOR

The FACET accelerator from start of operation in 2011 until its end in 2016 made use of many SLC accelerator parts (see sketch figure 5.1[106]). The thermionic electron gun is such an example. It was developed for the SLC collider and can inject up to 5×10^{10} electrons ($\hat{=}8\,\mathrm{nC}$) into the Linac [107]. Thermionic guns have the disadvantage that they produce higher-emittance electron bunches than state-of-the-art photocathodes. As a countermeasure, the bunch is cooled down in the North Damping Ring (NDR) to a transverse emittance of $30 \times 3\,\mathrm{mm\,mrad}$ [74].

The electron bunch is then compressed to a length of $\approx 6\,\mathrm{mm}$ [108] and injected into the linac via the North Ring to Linac Chicane (NRTL). The phase at which the electron bunch is injected into the linac S-band RF period can be tuned to change the energy chirp in the beam to achieve optimal compression in the following chicanes. This parameter is called the *phase ramp* and is one of the most frequently used measures to maintain a stable bunch compression during beam operation. Since phase-ramp adjustments change the electron-bunch phase with respect to the RF phase, it also changes the relative timing between the master RF reference signal and the electron beam arrival at a given z-position along the linac.

This detail is of particular importance for the E210 experiment, because precise timing between the laser pulse, which is stabilized to the master RF reference, and the electron beam is

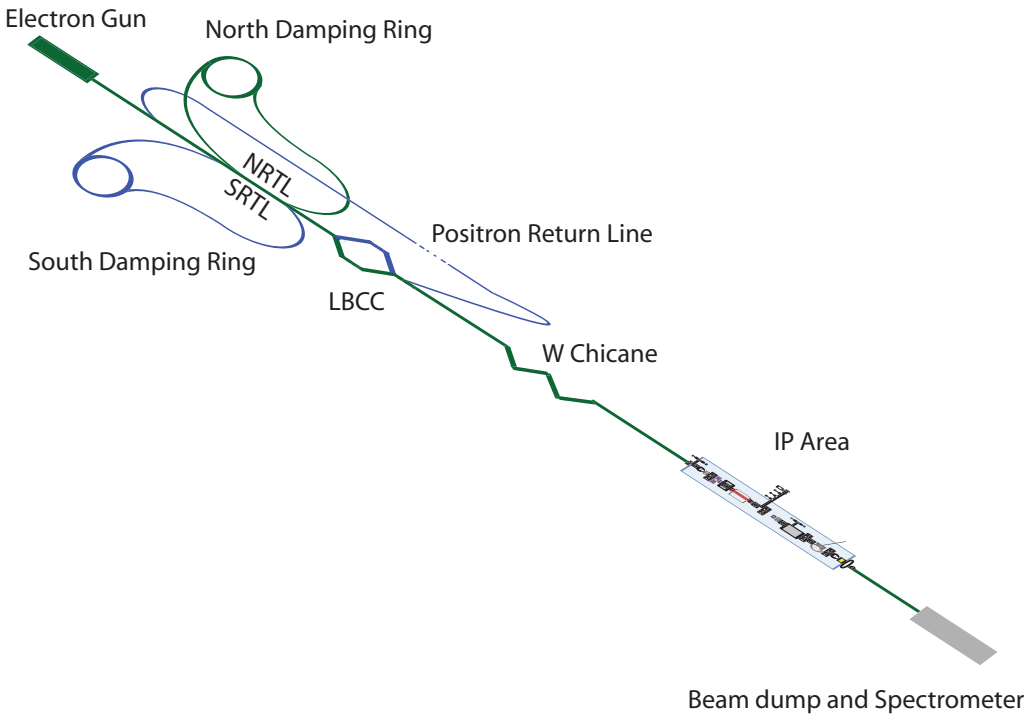

Figure 5.1: Schematic sketch of the FACET Linac beamline. Beamline components specific to positron acceleration are drawn in blue. Lengths are not to scale. A map of accelerator parts can be found in reference[106]. Image altered from an image by P. Scherkl.

required. The S-band frequency is 2.586 GHz, which corresponds to 1.0742 ps/° phase ramp. During the experimental campaign, the phase ramp required changes by only a few degrees and beam operators were asked to keep the phase ramp constant during data acquisition. The bunch when injected into the linac is approximately 1.5 mm rms long. It is accelerated to 9 GeV in the first 10 linac sectors and is then further compressed by the Linac Bunch Compressor Chicane (LBCC) in sector 10 to approximately 60 μm bunch length. In sector 11 to 20, the bunch is accelerated to its final energy of 20.35 GeV and then compressed a final time by the sector 20 *W-chicane* to a minimum bunch length of 20 μm rms length[4]. Subsequently, the final-focusing magnets in sector 20 compress the electron-bunch transversely, with typical values for $\beta_x^* = 0.25\,\mathrm{m}$ and $\beta_y^* = 1.0\,\mathrm{m}$ for the different transverse axes. The coordinate system convention at FACET is that z describes positions along the accelerator, y is the vertical axis and x the horizontal axis. The beam waist, which is the focal position of the electron bunch, was in most cases set to the start of the plasma, because one can expect that, after entering the plasma, the strong focusing forces of the blowout determine the transverse bunch behavior. It,

4 *W* refers to the shape of the sector 20 chicane. In the original FACET proposal a second part of the chicane was planned to simultaneously compress electron bunches and positron bunches. This plan is called the *sailboat chicane*.

therefore, makes sense to have the electron-bunch smallest when this sets in[5].

In the course of the E210 experiment, if not otherwise stated, we requested the full-charge, fully compressed standard FACET bunch with $30\,\mu\mathrm{m} \times 30\,\mu\mathrm{m} \times 30\,\mu\mathrm{m}$ bunch size. Depending on the overall machine condition, these target values were not always reached and drifted during the beam shift. The bunch was characterized at least once before and once after each shift. A wire scanner approximately 1 m upstream of the plasma section measured the transverse spot size, so bunch sizes might be a little bit under-estimated at the experimental focus. The bunch length was characterized by an X-band travelling-wave transverse-deflecting cavity (TCAV) [71, 109]. In contrast to an accelerating RF cavity, in a TCAV, the cavity structure resonates in a mode that transversely deflects the electron bunch. The deflecting wave co-propagates, synchronized with the electron bunch such that the electron bunch travels along at the zero-crossing of the sinusoidal amplitude of the deflection. Consequently, the beam electrons obtain a kick with a linear dependence on their longitudinal position. This kick relates the longitudinal ξ position of the beam electrons to a transverse position after free propagation, which is observed on a titanium optical-transition-radiation (OTR) screen downstream of the TCAV and allows for measurement of the bunch length.

The electron-beam characterization could not be done during the experiment. As long as the plasma section is filled with gas, the thin and sensitive wires of the wire scanner can be broken by plasma discharges. The same hazard applies to the integrity of OTR screens. Additionally, a deflected bunch cannot be used as a driver for the wake fields, so that during beam shifts the bunch length was monitored by a pyroelectric bunch-length monitor (BLM). The sector 20 BLM consists basically of an off-axis mirror that picks up the edge radiation from the electron bunch when exiting the magnetic field of the last chicane bend and reflects it into a pyroelectric detector[110]. The so-called *Pyro* Signal U_{PYRO} has been measured to depend on the total bunch charge Q_{b} and the longitudinal bunch length σ_z^{b} with the relation [111]

$$U_{\mathrm{PYRO}} \propto \frac{Q_{\mathrm{b}}^2}{\sigma_z^{\mathrm{b}}}. \tag{5.1}$$

Measuring the Pyro value is non-invasive to the electron bunch and was performed on a shot-to-shot basis for the sector 20 BLM, which was located downstream of the W-Chicane. The Pyro value does not come close to the accuracy of the TCAV measurements but it is a good feedback tool to monitor drifts in the linac that affect the final bunch length. The Pyro value can also be used in the post-processing of the data. During malfunctioning of a klystron or an alignment drift, the Pyro value can drop by more than half, indicating a weak compression or low charge. These shots then clearly stand out from the normal situation and can be omitted from further analysis.

After the final-focusing section, the electron bunch traversed the *interaction-point (IP) area*, where several different experiments were set up. The energy spectrum and emittance in the ho-

5 The FACET beam line also provided the option of accelerating positrons, which enabled it to measure positron-acceleration in plasmas. This is also an important and fascinating research topic, but for the experiments described in this work, only crucial in the sense that the start of the positron experiments set a definite end date to hydrogen-plasma experiments. For completeness, the positron beam optics are drawn in blue in figure 5.1.

rizontal x-plane can then be analyzed by the imaging spectrometer before the electron bunch's journey comes to an abrupt end in the beam dump at the end of sector 20.

5.3 THE FACET IMAGING SPECTROMETER

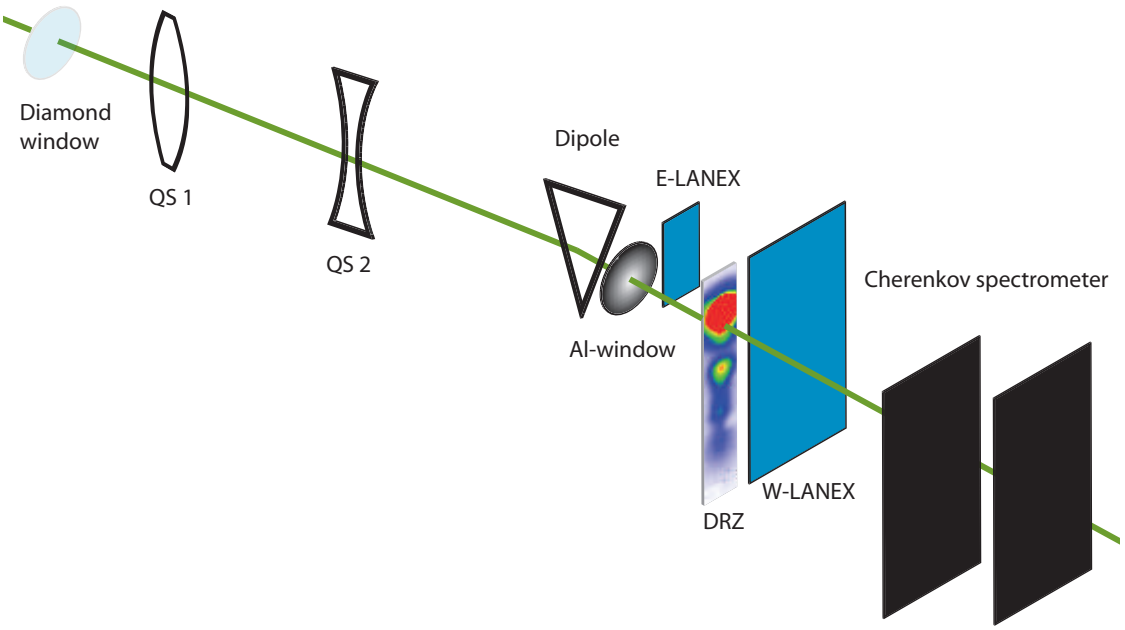

Figure 5.2: Sketch of FACET spectrometer setup: QS1 and QS2 set the focusing energy and the dipole deflects the electrons down (negative y direction). The electron beamline is separated from the screens by a diamond window and an aluminium window. Two LANEX screens are available to analyze the spectrum, the movable E-LANEX, and the larger W-LANEX. The spectrum can also be measured with a Cherenkov spectrometer.

The imaging spectrometer consists of three electromagnetic quadrupole magnets, QS0, QS1 and QS2 and an electromagnetic dipole. During the experimental campaign, only QS1 and QS2 were used; QS0 was switched off. The quadrupoles are arranged to first focus and then defocus the electrons (FODO arrangement). The combination of QS1 and QS2 focuses electrons and produces an image of the electron beam from an object plane of choice onto an image plane of choice. The focusing is sensitive to the electron energy, which therefore needs to be selected.

The dipole disperses the electrons in the vertical y plane, with the highest energies at the top. The resulting image on the screen is a butterfly-like image with a pinch at the energy chosen for the quadrupoles, which facilitates an energy calibration of the screens. The spectrum can be observed at three different locations: two scintillating screens and the Cherenkov spectrometer. Scintillating screens with a layer of phosphor – they go by their brand name *LANEX* – have been successfully applied as a standard diagnostic for electron beams for several years. The E-LANEX is the lanex screen closest to the end of the beamline. It can be moved up to analyze

drive-beam acceleration. The W-Lanex consists of two large screens to observe drive-beam deceleration or witness-bunches at lower energy than the drive-beam, one of which, the LANEX screen of the type DRZ [112] is more sensitive to low charge fluences, which is why during the campaign we used it for the witness-bunch analysis. The scintillation light is captured and observed by *PCO edge 5.5 CMOS* cameras [113].

The vacuum and plasma section is separated downstream by a 105 μm-thick diamond window, while the vacuum-to-atmosphere separation is sealed by a 5 mm aluminium window. The stopping power range of electrons in these thicknesses of material correspond to an electron-energy cutoff of 127 keV for the diamond window and 2.7 MeV for the aluminum window [114]. Most electrons below the cutoff energy will be stopped in the respective window.
For those electrons that reach the LANEX screen, it is possible to measure the charge (see calibration in section 8.1) and the energy spectrum of driver or witness bunch in the spectrometer.

From the shape of the butterfly on the spectrometer, it is additionally possible to determine the divergence of the witness bunch at the exit of the plasma, from which conclusions about the emittance can be drawn under the assumption of a particular β. This has been successfully applied by Vafaei-Najafabadi [115] for witness bunches at energies beyond 20 GeV. This method is more complex and less reliable for the witness bunches explored in this work because the generated witness bunches are accelerated up to only 3 GeV and have potentially very low emittance inside the plasma. For such low energies, scattering at the diamond window that separates the plasma section from the vacuum and the aluminum window that separates the vacuum from atmospheric pressure adds so much divergence to the bunch that such an analysis becomes complicated and goes beyond the scope of this work. The Cherenkov light spectrometer was not used by us during the experimental campaign. The interested reader can find a good description of it in reference [116].

5.4 THE FACET LASER

The FACET accelerator, including the E210 experiment in sector 20, is situated in a concrete tunnel 10 meters underground. Accelerator infrastructure, like klystrons that generate the accelerator RF signal and cabling for the main RF reference, are located at ground level. At ground level also most of the FACET laser system is built up. The FACET laser system provides laser pulses with a minimal pulse length of $\approx$ 25 fs FWHM at a maximum repetition rate of 10 Hz [117]. The optical medium used along the beamline to amplify the laser pulse is Ti:Sa [6].

Ti:Sa crystals are most efficiently pumped at a wavelength of $\approx$ 485 nm and in most applications lase at a wavelength of $\approx$ 800 nm. The laser beam line starts with a Vitara main oscillator by Coherent. The oscillator is locked to the master RF reference of the linac to ensure proper timing with respect to the electron bunch and mode-locked so that it provides 20 fs laser

6 It is conventional to write the bulk medium last and the dopant first. In this case, this means the optical medium is Sapphire (Sa) with a dopant of Titanium (Ti).

pulses at a repetition rate of 68 MHz. In a regenerative amplifier (Regen), the laser pulses are amplified to 3 mJ at 120 Hz. After the Regen, the laser pulse is stretched to apply chirped pulse amplification (CPA) [118]. The laser pulse has a wavelength of $800 \pm 60\,\mathrm{nm}$. A Pockel's Cell chooses laser pulses with the repetition rate of the electron beam - but at most at 10 Hz to protect the main amplifier - and sends them to the preamplifier. The preamplifier is traversed four times by the laser pulse and pumped by a Quantel CFR200 YAG laser. After the preamplifier, the laser pulse is at an energy of $\approx 30\,\mathrm{mJ}$. The main amplifier is also a four-pass amplifier that is pumped by two SAGA YAG lasers, which pump the crystal from opposite sides. The SAGA pump lasers themselves are pumped by flash lamps and are frequency doubled to 532 nm to ensure a good overlap with the absorption range of the Ti:Sa crystal. One of the pump lasers showed a rather rapid decay of the flash lamps during the campaign, which is why it was replaced by a Continuum YAG pump laser. Although the laser system was commissioned to deliver laser pulses at an energy of $\approx 1\,\mathrm{mJ}$ after the main amplifier, during the campaign it typically reached energies that varied between 500 mJ and 600 mJ as measured at the laser transport entrance. The 28 m-long transport beamline down to the IP area in sector 20 is evacuated to avoid plasma sparking. This would occur under atmospheric pressure because the relay imaging system included in the transport beamline focuses the laser down between the mirrors. The lenses of the relay imaging have the crystal surface of the main amplifier as object plane and the vacuum compressor as the image plane, which limits the propagation of unwanted structures in the transverse mode distribution of the laser. Before entering the vacuum compressor, the laser pulse was split by the *main sampler*, with 90 % of the energy being transmitted to the main laser and 10 % being reflected to the probe laser arm. The main laser was compressed in the vacuum compressor. Its FWHM pulse length was measured with a Single Shot Autocorrelator (SSA) to be 55 fs. The vacuum compressor gratings are motorized so that the main laser compression can be remotely altered. The probe laser pulse was compressed by an air compressor, which was not motorized. The probe pulse was measured to have an FWHM pulse length of 60 fs after the air compressor.

6

THE E210 EXPERIMENTAL SETUP

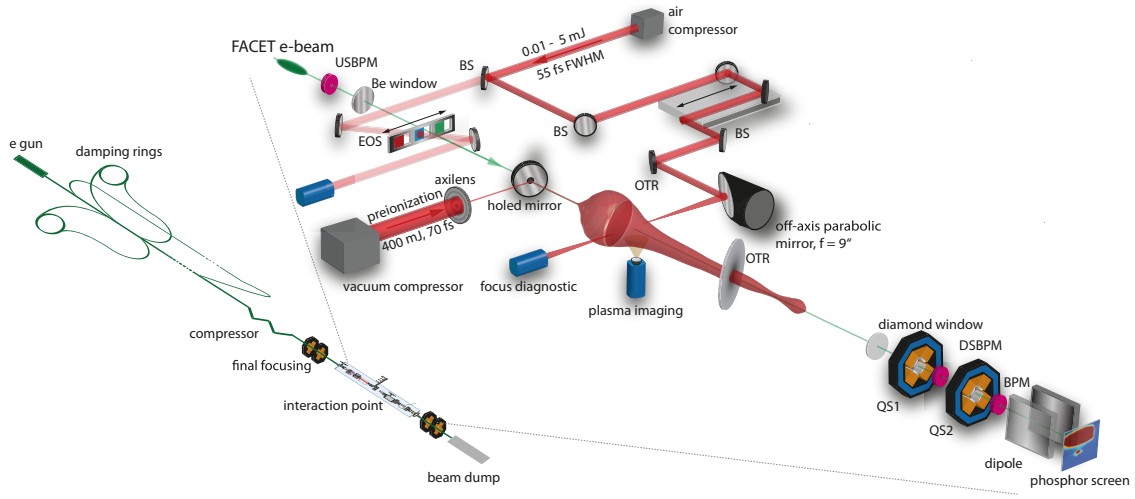

Figure 6.1: Sketch of the E210 experimental setup including the probe and main laser beamline. Image modified from an image by P. Scherkl.

The original purpose of the FACET laser was to ionize lithium or rubidium vapors for PWFA experiments conducted with an alkali gas oven as a plasma source. Eventually, the FACET laser system served several purposes. It was used to preionize gas and alkali vapors for PWFA, for injection as part of the plasma photocathode approaches, and for diagnostics such as probing in the E224 experiment.

At the *Advanced Accelerator Concepts (AAC) Workshop 2014*, several of the FACET experimental teams including that of the E210 experiment agreed on the wish to conduct experiments in hydrogen instead of lithium. Hydrogen in contrast to lithium is gaseous at room temperature and the pressures of interest. This made the plasma oven obsolete and allowed the plasma transverse to the electron beam axis to be accessed with laser arms or observed by cameras. The electron density could now be easily inferred by filling the entire plasma area with hydrogen and measuring the pressure.

Also, the main laser-to-e-beam alignment could now be improved. Several 6″ cubes with windows transverse to the electron-beam orbit allowed plasma recombination light to be observed and laser-to-e-beam alignment to be carried out using OTR screens. Figure 6.3 shows part of the hydrogen plasma line between cube 3 and cube 4 with the injection laser off-axis parabola (OAP) chamber attached to cube 3. OTR screens were attached to actuators on top of cube 3 as

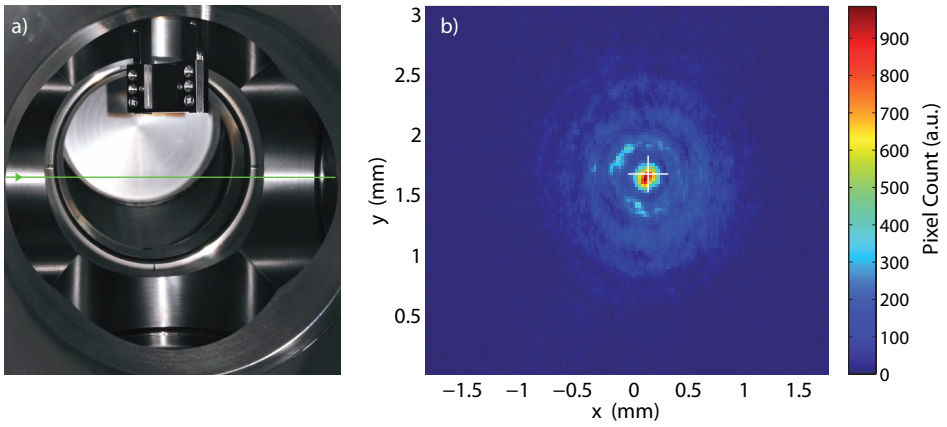

Figure 6.2: 500 μm thick titanium foil as optical transition radiation screen (OTR) to observe electron beam position as well as laser position(a) In the photograph it is lifted above the electron-beam orbit height, indicated by the green line. The screen needs to be at an 45 ° angle to reflect the signal light to the camera. Image (a) shows the OTR screen and image (b) shows the signal on the screen as obtained during the experiment. The attenuated laser, as well as the electron beam signal, can be observed at the same time. Image (b) shows good alignment between Bessel-function-like axilens laser-transverse intensity profile and the electron beam in the center.

well as cube 4. A photograph of a cube's interior including the OTR foil and the overlap between the electron beam and laser pulse can be seen in figure 6.2. To get a better understanding of the setup, figure 6.1 shows most of the parts used for the E210 experiments set up in sector 20 in a sketch[1]. Along the IP area, many CCD cameras were set up and were responsible for a variety of tasks. In general, mostly Manta GigE cameras [119] were used. Only the spectrometer was monitored by CMOS cameras.

A fraction of 10% of the pulse energy from the low-energy probe laser was coupled out by a beamsplitter for the electro-optical sampling (EOS) timing diagnostic, which is discussed in detail in section 7.2, to provide shot-by-shot timing information between laser pulse and electron beam prior to the plasma interaction. The high-energy part of the probe laser was then focused by a gold-coated 6" off-axis parabola with a focal length $f_{\mathrm{OAP}} = 9''$. The probe laser in the setup had to wrap once around the OAP chamber to ensure the correct laser path length and timing. This detail has been left out of the sketch for simplicity, but can be seen in figure 6.3. The linear motion of the OAP and the rotation around the axis of the incoming laser (roll) do not change the focal spot quality. These 4 degrees of freedom were used to align the OAP focus to the electron beam orbit under remote control. The focal spot was then monitored by the IPOTR3 camera, which also observed the electron orbit and the pre-ionization-laser position on the OTR screen (see figure 6.2 b). The focal quality and astigmatism were measured by the

1 Before reaching the OAP chamber, a small fraction of the probe laser was coupled out for plasma imaging experiments, performed by the E224 collaboration. This beamline is not shown as it is not part of the E210 setup.

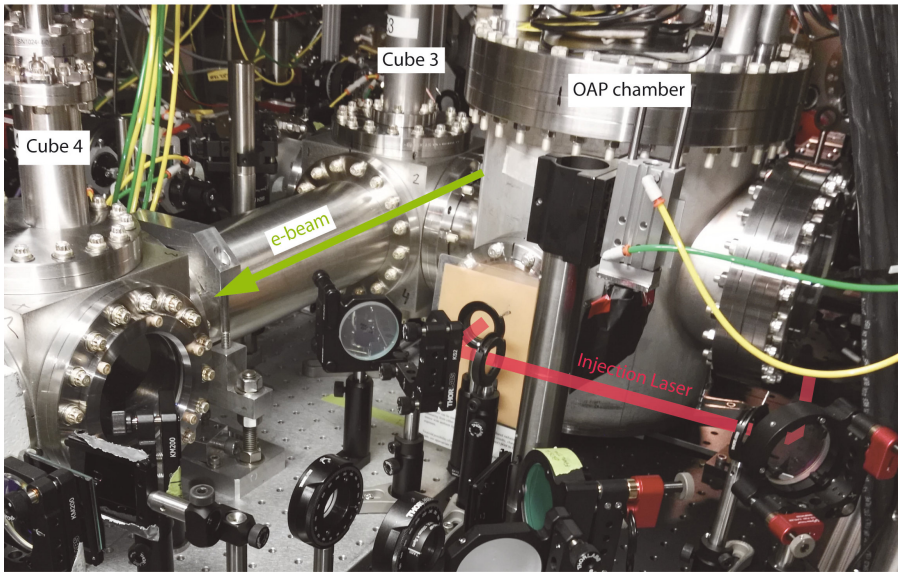

Figure 6.3: View on experimental setup from upstream to downstream. The 6″ Cube 3 with OAP chamber is shown on the right-hand side including the laser path to CaF_2 window (in this image covered by a fluorescent card). Cube 4 with a window is shown on the left-hand side. The distance between the center of both cubes is 50 cm. The plasma extended roughly between the upstream end of cube 3 and cube 4.

focus diagnostic, which contained a 2″ lens with a focal length of 300 mm and a camera, each mounted on linear stages. An image, taken by the focus diagnostic, can be found in figure 7.7. The *Cube3Vert* camera looked at the plasma through a window on the bottom of cube 3. Attached to it were 3 bandpass filters that could individually be flipped in or out to filter out laser light at 800 nm or to transmit the recombination light of H_2 at 589 nm or the recombination light of He at 656 nm. This diagnostic was key to the investigation of a novel plasma-based synchronization and alignment method as described in section 7.3. The preionization laser had a much larger portion of the total laser energy. After the vacuum compressor, it was focused by an axilens, developed by the E200 collaboration to produce ideally a 1 m-long and $\approx 88\,\mu$m FWHM-wide plasma channel. An axilens[120] was considered because of the experience gathered in the beamtime in the spring of 2015. The previously used axicon was able to generate a longer plasma channel, at the expense of the channel width. In Li, this is not so much of a problem because the electron-beam electric fields can ionize lithium, so that a small initial plasma-e-beam overlap can be sufficient to focus down the e-beam and keep a stable wake. Such an electron-beam ionization in hydrogen turned out to be extremely difficult to maintain stable from shot to shot and therefore was unviable for this application. However, the axilens turned out to be more sensitive to astigmatism, so that major transport beamline optimization work had to be done during the autumn run of 2015.

A calculation of the expected plasma size is shown in figure 6.4. The intensity distribution is calculated with a Matlab code [121] provided by S. Gessner, which was adjusted to meet the parameters for the axilens applied in the experiment and combined with an ionization routine

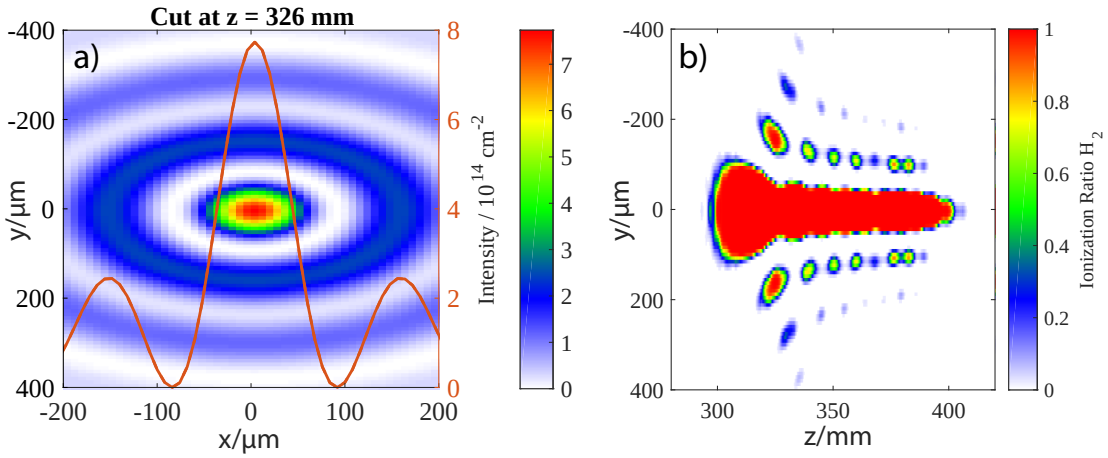

Figure 6.4: Calculation of transverse axilens intensity distribution at $z = 326\,\mathrm{mm}$ including the central lineout (a). The longitudinal cut of the ionization ratio for hydrogen ionization shows an expected plasma length of $\approx 1\,\mathrm{m}$ (b).

that resolves the ADK tunnel ionization of a temporal Gaussian-shaped laser pulse in envelope approximation. The mathematics behind the code can be found in the book by Goodman [122]. The code calculates the distortion of the laser wavefront during its propagation through the axilens material. A flat wavefront is assumed for the calculations discussed in this work. The distorted wave is then propagated to the focus position. This projection in Fraunhofer approximation can be reduced to a two-dimensional Fourier transformation[122], which is numerically evaluated with the Matlab Fast Fourier Transformation (FFT) package.

The calculated plasma length of $\approx 1\,\mathrm{m}$ was not achieved in the experiment. For many shots, no plasma or the end of the plasma was visible in cube 4 which is approximately 60 cm downstream of the start of the plasma at cube 3. The plasma could be shorter than expected due to the astigmatism in the laser or ionization defocusing [123], which is the effect of the plasma-density-dependent index of refraction distorting the laser phase front.

6.1 LASER ENERGY CALIBRATION

The laser energy available on target could be remotely modified at two positions in the laser beam line. Each of the two laser-energy attenuators consisted of a broadband polarizing beam splitter cube between two zero-order 808 nm half-wave plates. The half-wave plate, which was located further upstream in the laser beam line, was motorized, such that the amplitude of the attenuation could be remotely controlled. The beamsplitter cubes have a length of 12.7 mm. Traversing a glass material of this length with a compressed laser pulse means risking nonlinear effects such as self-focusing, which can damage the bulk material and distort the laser

pulse (see breakup integral equation 6.11). Therefore, the attenuators were situated upstream of the compressors.

The laser was split up by a beam splitter, the *main sampler*, right downstream of the laser transport beamline. The main sampler reflected 10 % of the laser energy into the so-called *probe laser* beam line and transmitted 90 % of the laser energy into the so-called *main laser* beam line. One of the attenuators, the *main energy wave plate* attenuator, was located upstream of the laser-transport beamline and therefore acted upon the entire laser energy being sent to the experiment.

The second laser-energy attenuator, the *probe energy wave plate* attenuator, was set up downstream of the main sampler in the sector 20 tunnel. This means that the laser energy available in the probe laser beam line was determined by a combination of both wave-plate settings, while the energy available on the axilens in the main laser beam line was set only by the main laser-energy wave plate. The typical shot-to-shot laser energy jitter is ≈ 5 % FWHM as measured by a power meter in the laser room.

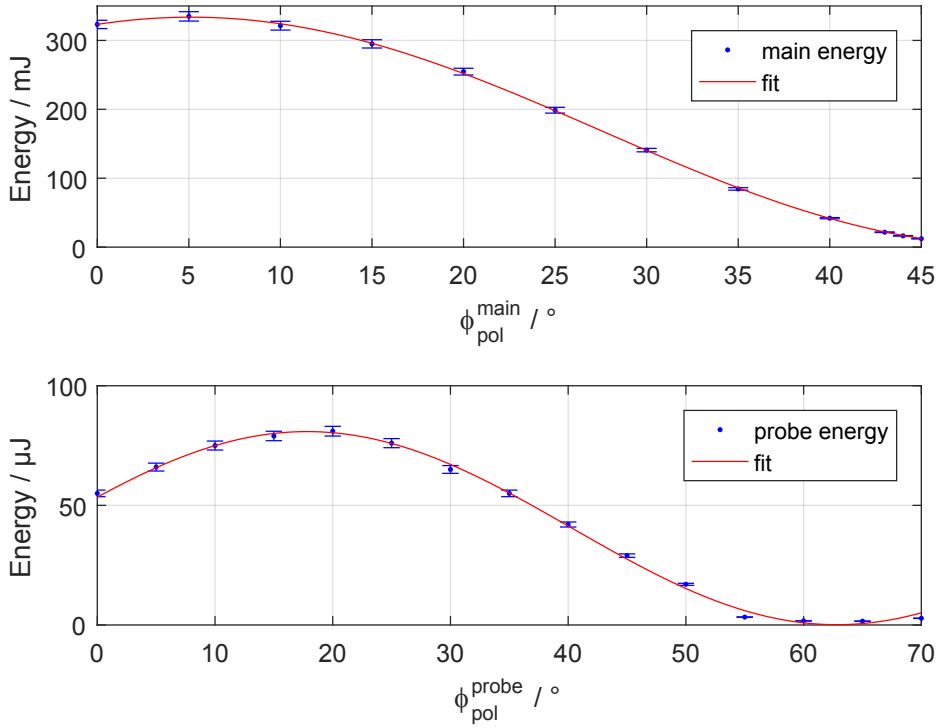

Figure 6.5: Laser energy calibration for main energy waveplate (upper plot) and probe energy waveplate (lower plot)

The laser beam line contained numerous optical elements that decreased the maximum available energy on target. All losses in optical components were measured. The total transmission values were integrated into the results of calibration measurements for the laser-energy attenu-

ators. The functions, fitted to the calibration data are plotted in figure 6.5. The calibration fit function including the measured transmission values for the energy available on the axilens is

$$W_{\text{Laser}}^{\text{Axilens}} = W_{\text{Laser}}^{\text{Laserroom}} \times 0.253 \tag{6.1}$$

$$\times \left(0.994 \cos^2((\phi_{\text{pol}}^{\text{main}} - 5.11^\circ)) + 6.16 \times 10^{-3}\right). \tag{6.2}$$

For the energy on the OAP, the function is

$$W_{\text{Laser}}^{\text{OAP}} = W_{\text{Laser}}^{\text{Laserroom}} \times 1.25 \times 10^{-2} \tag{6.3}$$

$$\times \left(0.994 \cos^2((\phi_{\text{pol}}^{\text{main}} - 5.11^\circ)) + 6.16 \times 10^{-3}\right) \tag{6.4}$$

$$\times \left(0.998 \cos^2((\phi_{\text{pol}}^{\text{probe}} - 17.8^\circ)) + 1.65 \times 10^{-3}\right). \tag{6.5}$$

This means that, for a typical laser energy output of 500 mJ, a maximum energy of 6.2 mJ is available on the OAP target and 125.9 mJ on the axilens.

6.2 PROBE LASER ENERGY LIMITATIONS

In the 2015 spring beamtime, we performed the first attempt to show Trojan Horse Injection. Due to the tight FACET schedule we chose a simple setup, in which the probe laser was focused by a $f = 200\,\text{mm}$ lens through a CaF_2 IR coated window. With this setup, we did not succeed in injecting electrons and did not observe ionization by the probe laser. Focusing through the window generated a secondary focal spot that was reflected by the window surface and damaged several optical elements. Moreover, the compressed probe-beam laser pulse traversed a few optical elements, which probably led to a lengthening of the pulse duration. For the fall beamtime, we altered the setup, according to the lessons learned. In the revised setup, the collimated probe laser entered the vacuum through a 3 mm-thick CaF_2 window. The laser was focused by an OAP, mounted in a specialized chamber shown in figure 6.3.
The applicable on-target laser energy in this setup was limited by the window damage threshold. We determined the limits in three parameters:

1. PEAK FLUENCE: Fluence F is the total laser energy applied per unit area. It is a better figure of merit for long laser pulses; most laser-induced damage threshold (LIDT) values given by the manufacturers are not measured for fs pulse lengths but for a ps- or ns-long pulse. Those values can be corrected by the engineering formula [124]

$$F_{\text{max}} = F_{\text{LIDT}} \sqrt{\frac{\lambda_{\text{exp.}}}{\lambda_{\text{LIDT}}}} \sqrt{\frac{\tau_{\text{exp.}}}{\tau_{\text{LIDT}}}}. \tag{6.6}$$

For a 190 fs-long laser pulse with a wavelength of 790 nm, the damage threshold is $2.70\,\text{J/cm}^2$ [125]. This means a fluence damage threshold of

$$F_{\text{max}} = 2.70 \sqrt{\frac{800\,\text{nm}}{790\,\text{nm}}} \sqrt{\frac{60\,\text{fs}}{190\,\text{fs}}}\,\text{J/cm}^2 \tag{6.7}$$

$$= 1.53\,\text{J/cm}^2. \tag{6.8}$$

2. NONLINEAR FOCUSING: The propagation of light inside a material is characterized by its dispersion relation $\omega(k)$, which can be calculated from the material's electronic response to the electric fields of the light. If the electronic displacement ceases to be small in comparison to the potential, the dispersion relation becomes dependent on the light's intensity I. This is implemented into the electric wave propagation by adding an intensity-dependent term η_2 to the index of refraction

$$Ee^{-i(\omega t-kx)} = Ee^{-i\omega(t-\frac{x}{c}(\eta_1+\eta_2 I))}. \tag{6.9}$$

The phase difference between a wave propagating in vacuum and in a medium of length L is then

$$\Delta\Phi = \frac{2\pi}{\lambda}\eta_1 L + \frac{2\pi}{\lambda}\int_0^L \eta_2 I(x')dx'. \tag{6.10}$$

The latter term of the sum is called the *Breakup Integral* or B-Integral

$$\widetilde{B} = \frac{2\pi}{\lambda}\int_0^L \eta_2 I(x')dx'. \tag{6.11}$$

These intensity-dependent changes in phase cause a focusing of high-intensity parts of the laser. The focusing increases the intensity which in turn increases the focusing again. This instability is called small-scale self-focusing (SSSF) [126] and can lead to structural damage in transmissive optical elements such as the window. Since the growth rate of the instability is proportional to $\exp(\widetilde{B})$[127], we chose the threshold of the B-Integral to

$$\widetilde{B} < 1 \tag{6.12}$$

to avoid damage.

3. PEAK INTENSITY: As a precautionary measure we additionally decided to limit the peak intensity at the window to

$$I_{\max} < 10^{12}\,\mathrm{Wcm^{-2}} \tag{6.13}$$

to avoid ionization.

SYMMARY OF DAMAGE THRESHOLD CONSIDERATIONS The window was constructed from CaF_2. The material was chosen because of its low nonlinear refractive index value of $\eta_2(CaF_2) = 1.26\times10^{-16}\,\mathrm{cm^2\,W^{-1}}$[128], so that the B-Integral can be kept at a low value. The transverse profile of the injection which was collimated while traversing the window can be approximated by a flat-top with a diameter of 10 mm. In this arrangement, $\widetilde{B} = 1$ corresponds to a fluence of $18.5\,\mathrm{mJ\,cm^{-2}}$ and an intensity of $3.4\times10^{11}\,\mathrm{W,cm^{-2}}$. This gives a limit of

$$W_{\text{probe}}^{\max} = 14.6\,\mathrm{mJ} \tag{6.14}$$

onto the CaF_2 window. $W_{\text{probe}}^{\max}$ is far above the maximum energy provided by the laser system, as demonstrated in section 6.1, so that in the modified setup, no window damage is expected.

7

LASER-TO-ELECTRON-BEAM SYNCHRONIZATION

In order to establish controlled injection of electrons into the wake, synchronization between electron beam and laser pulse to the order of 10 fs is desirable. In this chapter, our work addressing the relative time of arrival between electron bunch and laser pulse is presented. First in section 7.1 the timing jitter is estimated. The design and commissioning of an electro-optical sampling diagnostic are described in section 7.2, which includes a measurement of the timing jitter. In section 7.3 a novel plasma-based method to find synchronization is analyzed with measured data, theory, and simulations.

7.1 TIMING JITTER ESTIMATE

Two major contributors to the expected jitter in time of arrival between laser pulse and electron bunch could be identified, the jitter between laser pulse and RF master reference and the jitter between electron bunch and RF master reference.

The Vitara-T laser main oscillator is mode-locked to the radio-frequency (RF) master reference [117]. This lock has a timing jitter of [117]

$$\sigma_t^{\mathrm{RF,laser}} = 70\,\mathrm{fs}. \tag{7.1}$$

The electron bunch on the other hand has a timing jitter with respect to the RF, which can be estimated with the help of linear beam optics as described in section 2.6. Due to energy-dependent path lengths in the FACET W-chicane, as illustrated in figure 7.1, an electron-bunch mean energy devation from the design energy, δ_0, leads to a longitudinal offset

$$z_1 = z_0 + R_{56}\delta_0. \tag{7.2}$$

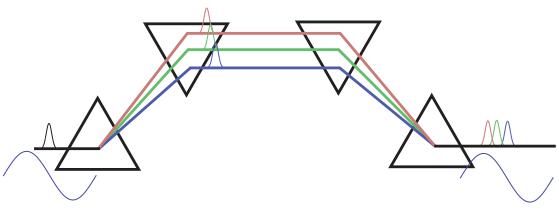

Figure 7.1: Sketch of a chicane with trajectories dependent on electron-bunch energy. Electron bunches at different energies, but at same time with respect to the RF master reference end up at different timing after the chicane.

The relative longitudinal offset between two bunches α and β can then be written as

$$\Delta z = z_0 - z_0 + R_{56}\delta_0^{\alpha} - R_{56}\delta_0^{\beta}. \tag{7.3}$$

This means, from the electron-beam energy jitter σ_W/W, one can deduce a jitter in time-of-arrival

$$\sigma_t^{\mathrm{e}^-,\mathrm{RF}} \approx \Delta z_{\mathrm{f}}/c \tag{7.4}$$

$$= \frac{1}{c} R_{56} \frac{\sigma_W}{W} \tag{7.5}$$

with respect to the RF signal, which runs at the velocity designed for the target electron-bunch energy. The sector 20 chicane R_{56} is typically set to $-7\,\mathrm{mm}$ to achieve maximum bunch compression and the rms energy jitter has been measured to be $\sigma_W/W = \frac{18.7\,\mathrm{MeV}}{20.35\,\mathrm{GeV}} = 9.2 \times 10^{-4}$[74] so that the rms jitter in the time of arrival of the electron beam with respect to the master RF reference can be estimated to be

$$\sigma_t^{\mathrm{e}^-,\mathrm{RF}} \approx 21.5\,\mathrm{fs}. \tag{7.6}$$

Additional laser time-of-arrival jitter due to pointing jitter is negligible. This leaves us with a total estimated jitter between the laser-pulse and electron-bunch time of arrival of

$$\sigma_t^{\mathrm{e}^-,\mathrm{laser}} = \sqrt{(\sigma_t^{\mathrm{e}^-,\mathrm{RF}})^2 + (\sigma_t^{\mathrm{RF,laser}})^2} = 73.2\,\mathrm{fs}. \tag{7.7}$$

One needs to keep in mind that this is a rather optimistic estimate. Small variations in the energy-dependent electron-beam orbit over several km of accelerator are completely ignored, because of lack of data. This might be a large effect. Furthermore, it is definitely advisable to be able to track timing variations from long-term drifts in order to compare datasets which are taken hours apart from each other or even on different days.

7.2 ELECTRO-OPTICAL SAMPLING (EOS)

Electro-optical sampling (EOS) is a standard method that is well suited for determining differences in arrival times between a laser pulse and a source of THz radiation, such as emitted by the FACET electron bunch. When the ultra-relativistic electron bunch passes the crystal, the THz radiation traverses the crystal and acts upon the crystal for the time of the passage of the electron bunch. The crystal transiently changes its optical properties and alters the polarization of the laser pulse, from which relative timing information can be obtained. The method has been previously shown to reliably measure the bunch length of sub-picosecond electron-bunches [129].

This method exploits the optical anisotropy of electro-optical crystals, which is altered by the external electric field from the electron bunch. Electromagnetic waves as from a laser pulse, propagating through an anisotropic crystal perceive a difference in dielectric permittivity, ϵ_{r},

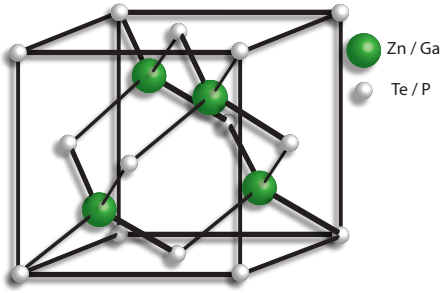

Figure 7.2: Unit cell of a ZnTe or GaP crystal structure.

depending on entrance angle and polarization of the wave, which is why the dielectric properties need to be addressed in a more general way with the dielectric permittivity tensor $\hat{\epsilon}$. This is equivalent to a polarization-dependent index of refraction, a property known as *birefringence*, which leads to a polarization-dependent phase velocity of light inside the crystal.

A laser at the correct incident angle with respect to the crystal's anisotropy samples a phase-shift between different planes of polarization which leads to an overall change in the laser polarization, depending on the phase-shift strength and the crystal size. Electro-optical crystals change the orientation of the dielectric permittivity tensor when an external electric field $\vec{E}_{\text{ext.}}$ is applied. The strength of this effect can be illustrated by a Taylor expansion of the impermeability tensor

$$\hat{\eta} = \hat{\epsilon}^{-1} \tag{7.8}$$

for small external electric fields $\vec{E}_{\text{ext.}}$ to

$$\eta_{ij} = \eta_{ij}(0) + r_{ijk}E_k + s_{ijkl}E_kE_l + \dots. \tag{7.9}$$

The linear dependence on the electric field strength is called the Pockels Effect, with r_{ijk} being the Pockels coefficient. The Kerr effect with the Kerr coefficient s_{ijkl} describes the quadratic dependence on the electric field.

In the context of the experiments described in this work, only two types of electro-optical crystals were used, gallium phosphide (GaP) and zinc telluride (ZnTe). Both crystals are packed in the so-called zincblende structure, as depicted in figure 7.2. In this structure, the Te (or P) ions are arranged in a face-centered cubic structure and the Zn or Ga ions are in the center of orthogonal sub cubes the size of a quarter of the unit cell. For crystals in zincblende structure, the Pockels coefficient dominates over the Kerr effect. For GaP and ZnTe, the order of magnitude of the Pockels coefficient is $r_{ijk} \approx 10^{-12}\,\text{mV}^{-1}$ and the order of magnitude of the Kerr coefficient $s_{ijkl} \approx 10^{-21}\,\text{m}^2\text{V}^{-2}$[130], so that the Kerr effect can be neglected[1].

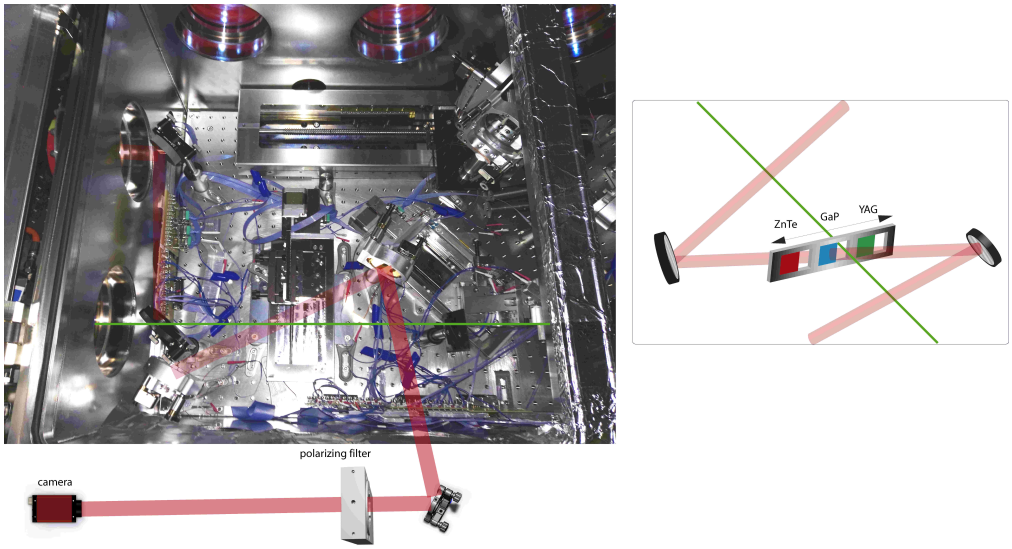

Figure 7.3: Setup of upstream electro-optical sampling inside the so-called "picnic basket" vacuum chamber. The electron-beam (green) and EOS laser (red) co-propagate at an angle of $\approx 45^\circ$ to each other.

Setup of the Electro-Optical Sampling

An electro-optical sampling (EOS) was set up as a non-destructive shot-by-shot diagnostic in order to measure the relative time of arrival between electron bunch and laser pulse as close to the interaction point in cube 3 where the witness bunch injection should occur. In this experiment, the EO crystals were located in close proximity (few mm distance) to the electron beam axis. Due to the high $\gamma_b \approx 42000$, the electric field of the FACET electron beam at the interaction point is strongly Lorentz contracted in the laboratory frame. Therefore, the THz radiation traversing the EO crystal can be assumed to have the same length as the electron bunch. The electric field applied to the crystal and with that, the induced birefringence is only active while the electron beam passes by the crystal.

Figure 7.3 depicts the setup with a photo and a 3D representation. The EOS ladder shown on the right-hand side of figure 7.3, supports an Yttrium aluminium garnet(YAG) crystal to find the electron beam axis, a 500 μm thick ZnTe crystal for broad timing scans and a GaP crystal with 100 μm thickness for fine resolution. The crystal surface was oriented perpendicular to the electron-beam orbit to minimize temporal overlap and cut in the right plane for the laser-propagation. The orientation of the crystal was tested by colleagues at UCLA.

In the EOS setup, a laser pulse (red) with linear polarization in the vertical plane, which was split off the probe laser-beam, traverses the EOS crystal at an angle of $\approx 45^\circ$ with respect to the electron beam axis (green). The laser beam was collimated with a transverse diameter of $\approx 1\,\mathrm{cm}$ and completely illuminated the crystal. For a better signal-to-noise ratio, an additional

1 A detailed description of the physics involved in the application of electro-optical crystals as TOA and bunch length diagnostic can be found in [130]

polarizing filter was installed in front of the "picnic basket" chamber. We placed a motorized polarizing filter after the chamber. If set to an orientation perpendicular to the laser polarization, the intensity of the laser pulse was attenuated such that it was barely visible on the camera. If set to an orientation horizontal to the laser polarization, the laser was seen by the camera. This setting was used to align the laser with the crystal.

If the relative timing between laser pulse and electron bunch was correct, a part of the laser perceived a rotation to horizontal polarization in the EO crystal due to the previously mentioned Pockel's effect. The transverse part of the laser with horizontal polarization was afterwards less attenuated by the motorized polarizing filter than the rest of the laser pulse. As a result, the signal has the form of a line as seen in figure 7.4 with a horizontal position linearly corresponding to the relative TOA.

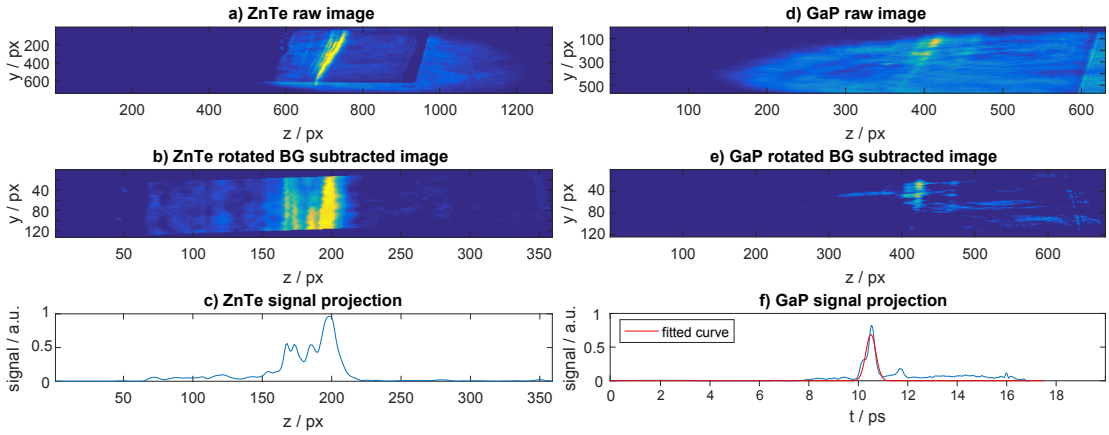

Figure 7.4: EOS signal post-processing for ZnTe crystal (l.h.s) and GaP crystal (r.h.s). A defined region of interest is background substracted with an image that shows laser-light but no EOS signal. The rotated and background-subtracted images(b,e) are projected in the y-plane. The resulting signal demonstrates how the ZnTe crystal can be used for rough alignment, while the GaP signal gives a clear peak which is then fitted. The ZnTe signal is plotted in units of pixels because the broad signal inhibits a reliable calibration.

Figure 7.4 also illustrates the post-processing procedure for the EOS signal. A small region of interest of the raw images (a,d) is rotated and the background is subtracted (b,e). As one can see, by comparing part (d) and (e), most of the background is laser light, which is not sufficiently attenuated by the polarizing filter. Since the laser profile, as seen by the camera, changes with alignment on a day-to-day basis, different background images are picked for every dataset. The image projection shows a strong but broad signal for the thick ZnTe crystal (c). This was intended since the purpose of the ZnTe crystal was only to find a broad timing range. A reliable calibration, however, is not possible with the given signal quality. The GaP signal, in contrast, is much cleaner. The maximum position, as well as a Gaussian fit, was calculated to determine the relative timing.

The EOS calibration was performed by changing the laser target time with respect to the RF main reference. For every time step, several shots were performed to take account of the timing jitter. There is a limit to the number of shots taken per dataset as for long data acquisition, drifts eventually start to become important. Frequent calibration is essential to take into account day-to-day changes in laser alignment. However, since timing scans were a common type of dataset during the experimental shifts, as will be seen in chapter 8, it was not necessary to take specific timing-calibration datasets on a regular basis.

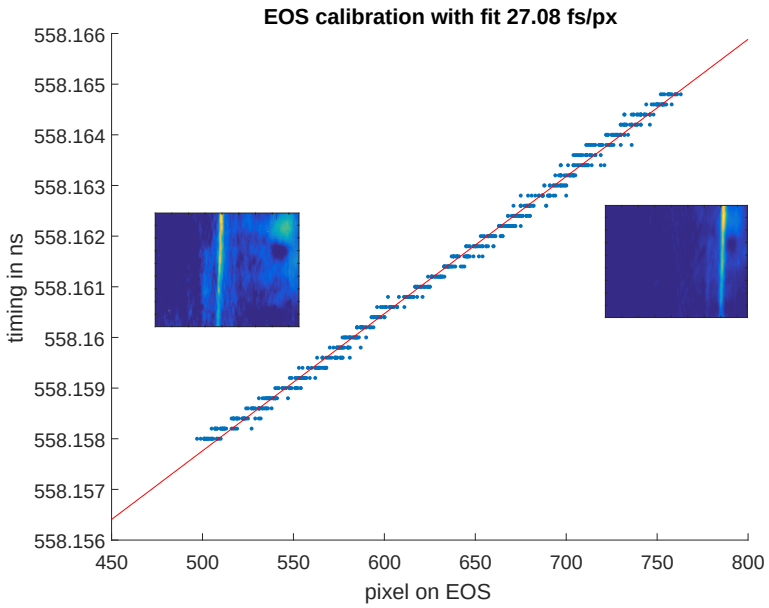

Figure 7.5: Typical EOS calibration. The peak position as seen in figure 7.3 f) is plotted versus the set timing difference. Insets show the signal homogeneity across the crystal.

An example of an EOS calibration is shown in figure 7.5 with a clear linearity between signal position and timing as well as a relatively narrow scattering of the datapoints around the mean step value. From several timing scans over several days, a mean calibration of

$$t_{\mathrm{EOS}}^{\mathrm{calib}} = 25.8 \pm 2.5\,\mathrm{fs/px} \tag{7.10}$$

was obtained.

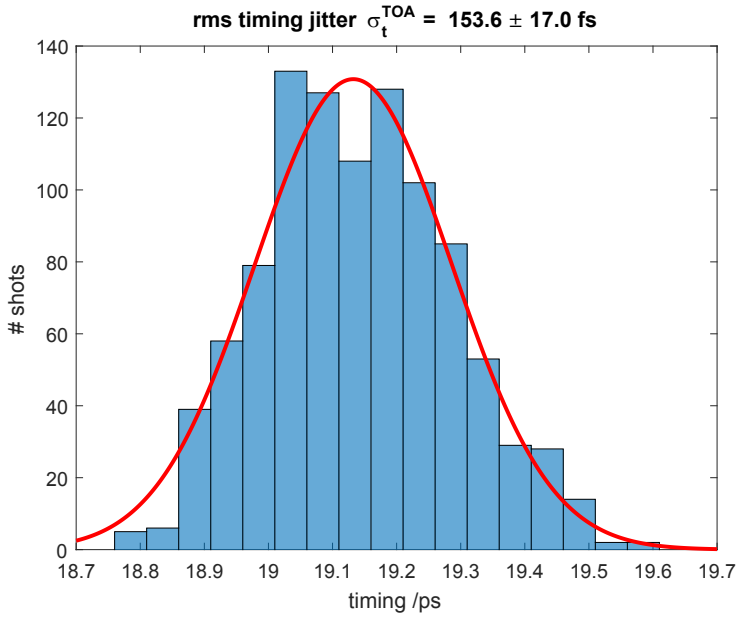

Figure 7.6: Histogram with fit of EOS data for 998 consecutive shots. The red curve shows a Gaussian fit to the taken jitter data.

With the calibrated EOS diagnostics, we determined the relative timing jitter between the electron beam and the laser pulse to compare it with our estimate. A total number of 998 consecutive shots were taken. A histogram of the timing data is plotted in figure 7.6. The rms width of a Gaussian curve, fitted to the distribution gives the timing jitter

$$\sigma_t^{\mathrm{TOA}} = 153.6 \pm 17.0\,\mathrm{fs}. \tag{7.11}$$

This result shows that the estimated timing jitter of 73.2 fs, was indeed much too optimistic and that implementing the EOS diagnostic is a crucial tool to determine the shot-by-shot relative timing.

Although this diagnostic can pin down precisely the most important contributor to the timing jitter, this was not done because this would have been a major machine-development task of unclear value and it was not essential to the success of a proof-of-principle. Instead, the EOS measured relative timing between electron beam and laser pulse shot-by-shot and non-invasively to the electron beam or laser pulse at the interaction point. This gives the freedom to sort the measured data by relative timing, as measured by the EOS in the post-processing without the need for low timing jitter. The EOS timing resolution varied over time due to alignment changes but stayed at resolution values of $\leq$ 30 fs, allowing phenomenona on time scales between 30 fs and 20 ps to be investigated.

Section 7.2 describes the EOS commissioning and demonstrates that it is excellently suited to measure the difference in arrival times between the electron beam and the laser pulse. Unfortunately, there is a distinct difference between relative timing and synchronization at the interaction point (IP). Given that the EOS crystal in the "picnic basket" chamber and the interaction point in cube 3 are several meters apart in laser path length, the timing offset remained unknown. Although the EOS measures a certain relative e-beam-to-laser-pulse timing, it still remained a crucial challenge to find an absolute reference.

The first attempt to address this problem was to send laser light from the EOS position downstream of the IP and set up an auto-correlator between both laser arms at the IP. This was eventually abandoned due to geometrical restrictions. The second idea was another EOS at the IP, with laser and electron beam in a 90° geometry. Besides the fact that the interpretation of the received signal was ambiguous, this setup also required change from a focused to a collimated injection laser by remote control, as well as a remote polarization and laser-energy control. This basically required a complete change between a high-energy laser with protection for cameras and crystal to a low-energy, high-quality laser with high sensitivity. Any mishandling of the settings during the shift led to inevitable and in practice frequent destruction of cameras or optical components.

Luckily it was observed before at FACET that the plasma light emission increased significantly if it was not only ionized by the laser but subsequently hit by the electron beam. This was used as a binary information for the long axicon-ionized plasma column whether or not the electron bunch arrived after the plasma generation. It was not known how accurately the synchronization between both could be achieved with this method or to what extent the phenomenon can be reproduced with a small plasma column, ionized by the injection laser. The combination of the EOS, a a camera to observe the injection-laser plasma and the focus diagnostic (see section 6) put us into a position to address these questions in a dedicated experiment.

The experimental setup was nearly identical to the one described in figure 6.1 with the small change that the pre-ionization laser was blocked so that only the injection laser ionized gas within a small filament around the electron-beam orbit.

The OAP focal spot and a longitudinal scan of the laser waist showing the astigmatism in the laser focusing is presented in figure 7.7. Although it was possible to reduce the focal spot size with the combination of OAP motorization and focus diagnostic, the measures had always to be weighed against other priorities crucial to the success of the experiment. For example, reduction of astigmatism in the injection laser could be reduced by optimizing the alignment of the OAP, but large movement of the OAP motors increased the risk of them getting stuck. While this may be considered a small problem in a laser lab that allows for easy hands-on access to the equipment, in combination with the FACET accelerator, such an access required an expensive shut-down of the accelerator of at least a day. Another possibility to reduce astig-

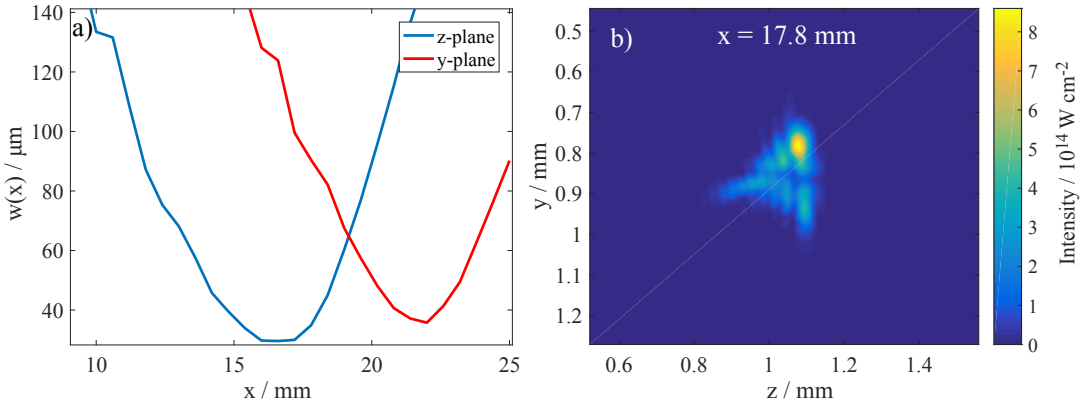

Figure 7.7: Focus diagnostic analysis of injection laser spot. A longitudinal intensity waist scan reveals strong evidence of astigmatism (a), which can also be seen by imaging the focus (b). Nevertheless, for 5 mJ on target, the He ionization threshold is easily surpassed.

matism was to slightly alter the laser-alignment into the transport beamline. Such changes, however, also impacted the quality of the pre-ionization laser focus. Finally, we decided that residual astigmatism and the asymmetrical focal spot illustrated in figure 7.7 were acceptable as long as the injection laser was able to ionize helium.

One huge advantage of the hydrogen FACET setup compared to the oven setup was that it allowed the plasma to be monitored at several view ports so that it was not only possible to make sure that He could be ionized, but also to observe the beam-plasma interaction. We set up a camera, viewing cube 3 (Cube3Vert) from the bottom, imaging the plane of the electron-beam orbit and attached two band-pass filters on remote-controlled flippers in front of it, one for $656 \pm 10\,\mathrm{nm}$ [131] and one for $589.3 \pm 10\,\mathrm{nm}$ [131], corresponding to He and H_2 recombination-light lines. The injection laser was remotely aligned to the electron-beam orbit by observing its transition radiation from a titanium foil in the beamline, while the laser was blocked (see "+"-beam mark in figure 6.2). After retracting the OTR foil from the electron-beam orbit, we attenuated the injection laser to an intensity at which it would not damage the camera and aligned its focus to the previously saved pixel position. The Cube3Vert camera takes an integrated image over several μs, a time window much larger than the plasma recombination time of typically a few ns. The EOS then allows these images to be sorted by TOA and the time scales to be measured precisely, so that we obtained an image that shows an integrated image over the radiated plasma recombination light, depending on the relative difference of the arrival time between the electron beam and the laser.

The compelling difference in signal can be seen in figure 7.8. a) shows the image as taken by the Cube3Vert camera for a relative timing with the laser being ahead of the electron beam at timing value $-2.216\,\mathrm{ps}$ and c) shows the opposite case at timing value $1.60\,\mathrm{ps}$ relative to the turning point of the fitted sigmoid function, respectively. The images were taken in a 50:50 He to H_2 mixture at $\approx 4\,\mathrm{torr}$ gas pressure, with the bandpass filter for the He recombination light inserted. Image (a) looks the same if the electron beam is not transported to the IP, which

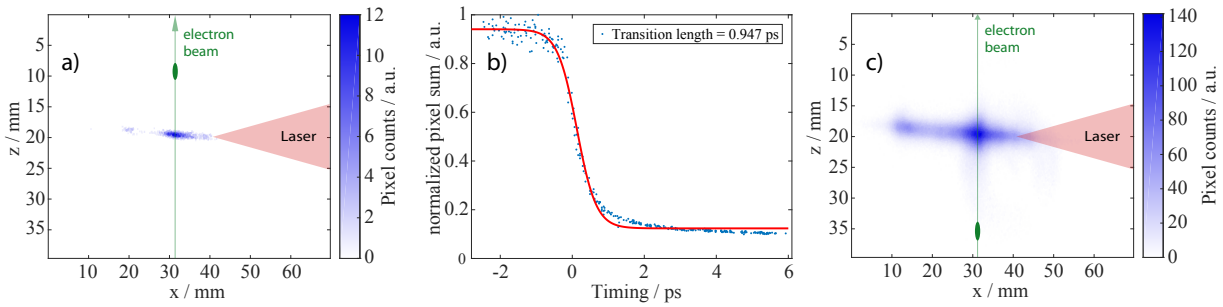

Figure 7.8: Scan of relative timing between electron beam and injection laser. Two Cube3Vert example images at timing $t = -2.216\,\mathrm{ps}$ (a) and at timing $t = 1.60\,\mathrm{ps}$ (c) are shown. The green arrow sketches the electron-beam axis and the red triangle indicates the propagation direction of the ionizing laser. Panel (b) shows the sum of pixel counts measured by the cube 3 vertical camera with a $656 \pm 10\,\mathrm{nm}$ band-pass filter are sorted by the EOS measured timing. $t = 0$ is defined as the turning point of the fitted sigmoid function.

indicates that the electron-bunch itself does not ionize H_2 or He significantly, compared to the laser pulse. We confirmed this by taking images while the laser pulse was blocked and the electron bunch was focused onto the interaction point. In this case, the Cube3Vert camera did not observe any plasma light. This observation also confirmed the decision not to rely on electron-beam ionization for the injection experiments described in chapter 8. In b) the normalized total pixel sum as counted by the camera is plotted versus the relative difference between the timing of the laser pulse and the electron beam as measured by the EOS. Thanks to the EOS sorting, the transition between both states is very clean and a sigmoid function can be fitted to it to determine the transition length. This length is defined as the width between the points at which the derivative of the sigmoid function has a value of 1/e of its maximum value and is

$$\tau_{\mathrm{trans}} = 0.947\,\mathrm{ps}. \tag{7.12}$$

Without sorting the data by the EOS, a transition length on the time scale of $\approx 1\,\mathrm{ps}$ can still be analyzed, but the data is much less clean as it is blurred by a timing jitter which is around 153.6 fs, as described in section 7.2.

During the data acquisition, the electron beam charge was $3.1 \pm 0.17\,\mathrm{nC}$ and the electron-beam dimensions during the shift were $29.2\,\mu\mathrm{m} \times 17.9\,\mu\mathrm{m} \times 35\,\mu\mathrm{m}$ rms. The energy of the injection laser pulse was $\approx 5\,\mathrm{mJ}$.

The effect of increased plasma glow is stronger with better overlap between electron beam orbit and plasma and can therefore be used for transverse alignment. Figure 7.9 shows the result of a transverse-alignment scan, obtained by rolling the OAP. The roll of the OAP is the rotation around the axis of the incoming laser. It leaves the focus quality intact and merely steers the focus in the y-direction so that a scan across the beam orbit can be done without additionally changing the plasma size. The vertical focus position is evaluated by the focus diagnostic. The

image shows how the light from the plasma can give important information about alignment to an accuracy of $\approx 100\,\mu$m.

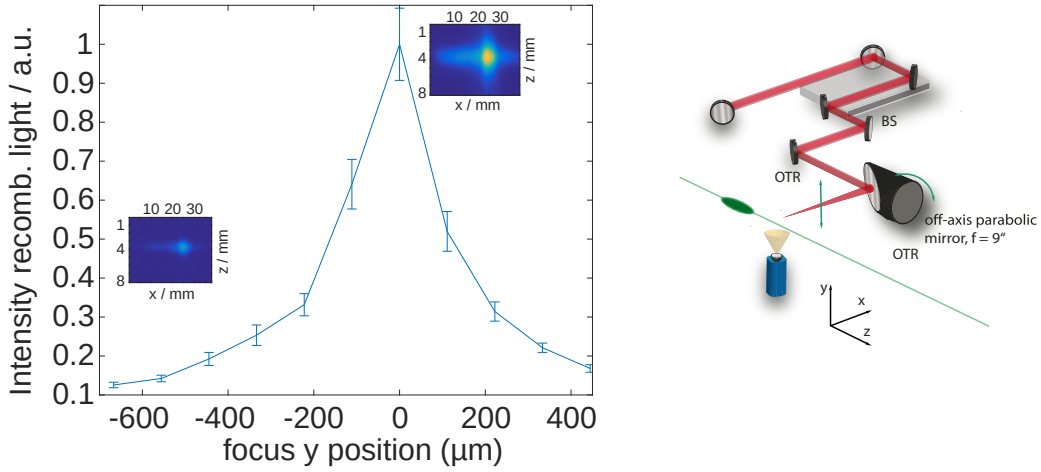

Figure 7.9: Plasma glow in 7.8 torr H_2 ($n_e = 5 \times 10^{17}\,\mathrm{cm}^{-3}$) measured by vertical camera in cube 3. The injection laser off-axis parabola roll is scanned. The vertical plasma position is evaluated by the focus diagnostic.

Three hypotheses can be made in order to explain the differences in plasma light emission:

- The additional plasma light is predominantly recombination light and due to additional ionization.

This hypothesis is supported by the fact that inserting a band-pass filter with the right wavelength for the recombination light of hydrogen or helium was beneficial for the image quality.

- The additional ionization is not an effect of the electron-beam ionization.

This is backed by observation because little to no change in plasma light emission was observed between the laser-after-e-beam case and a measurement without electron beam at the IP.

- The electron beam heats up the plasma and the plasma electrons further ionize nearby gas via collision ionization.

Confirmation of this hypothesis needs some detailed analysis and is tested in this section with simulation and theory.

The Lotz equation [132]

$$\sigma_{CS} = a_{CS}\frac{\ln(W_e/\xi_{ion})}{W_e\xi_{ion}}\left[1 - b_{CS}\exp\left(-c_{CS}\left(\frac{W_e}{\xi_{ion}} - 1\right)\right)\right] \tag{7.13}$$

describes the collision-ionization cross section of electron-ion collisions, depending on the electron energy W_e. It has three parameters: a_{CS}, b_{CS} and c_{CS}, that need to be fitted to experimental data for any given atom, ion or molecule with ionization energy ξ_{ion}. The data for He is already given in the original paper. Schram et al.[133] have measured the ionization cross sections for molecular H_2, from which the Lotz parameters can be obtained. The derived ionization cross sections depending on the electron energy are plotted in figure 7.10 a). The cross section approaches 0 for high electron energies and has its peak at a few keV above the ionization energy. No collision ionization occurs for electron energies W_e smaller than the ionization energy ξ_{ion}. Figure 7.10 b) is a histogram of the plasma-electron kinetic energy 5.6 ps after the electron-beam impact, as calculated in a PIC simulation with VSim. To obtain this result, a 3 nC FACET-like electron-beam was simulated with 15 μm radial and 20 μm longitudinal rms size interacting with a plasma filament as generated with the injection laser for the experimental described in section 7.3. The simulated density spike has a 25 μm flat region with a 50 μm cosine-shaped upramp and downramp. It is rotationally symmetric in the x-axis, transverse to the electron beam orbit and has a peak electron density of $n_{top} = 1.3 \times 10^{17}\,\mathrm{cm}^{-3}$. The volume around the density spike is assumed to be in vacuum.

A comparison between the spectrum of the expelled plasma-electron macroparticles and the cross section shows a large region of overlap. The lower graph compares the product of the charge in each plasma-electron bin and the cross section at that particular energy. The same product is shown for an electron-beam spectrum at a mean energy of 20.3 GeV in figure 7.11.

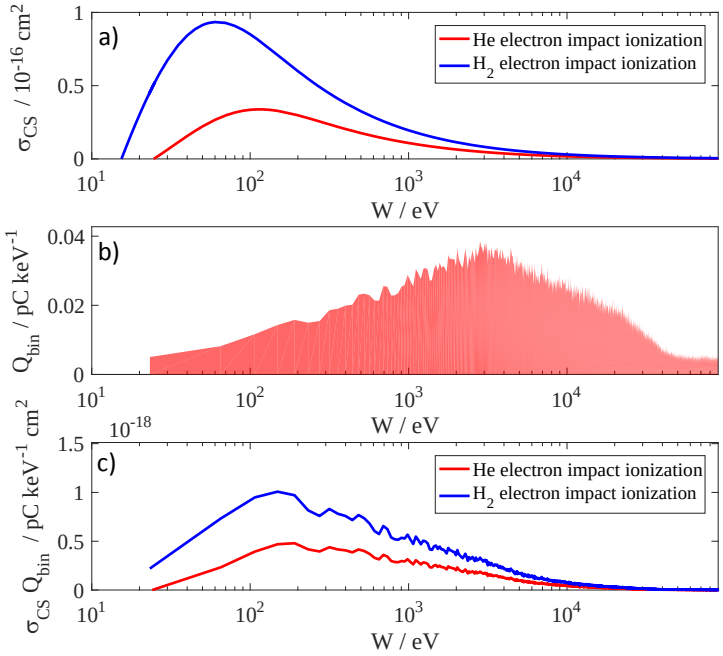

Figure 7.10: Electron impact ionization rates of He and H_2 fitted to data from reference [132, 133] as a function of electron energy (a). Plasma-electron spectrum from PIC simulation 5 ps after collision between a FACET-like electron bunch and laser-generated plasma (b). Binned product of both, proportional to impact ionization probability (c).

Comparing the values with those in figure 7.10, one can see that they differ by several orders of magnitude. The integral over energy of the product of the ionization cross section (equation 7.13) and the charge spectrum of the plasma electrons or beam electrons is proportional to the total ionization probability, under the assumption that the volume that can be ionized by the electron bunch is comparable to the volume that can be ionized by the scattered plasma electrons. Both integrals are evaluated as discrete sums because the spectra are obtained from PIC simulations. The ratio of the result of these sums for electron-bunch ionization and plasma-electron ionization for hydrogen is

$$\frac{\sum_{i\in\text{bins}} Q^i_{\text{plasma}}\sigma^i_{\text{CS}}(\text{H}_2)}{\sum_{i\in\text{bins}} Q^i_{\text{bunch}}\sigma^i_{\text{CS}}(\text{H}_2)} = 2.8\times 10^{11}. \tag{7.14}$$

For He the value is

$$\frac{\sum_{i\in\text{bins}} Q^i_{\text{plasma}}\sigma^i_{\text{CS}}(\text{He})}{\sum_{i\in\text{bins}} Q^i_{\text{bunch}}\sigma^i_{\text{CS}}(\text{He})} = 2.58\times 10^{11}. \tag{7.15}$$

The ratio is very large, confirming the experimental observation that the electron bunch does not considerably ionize hydrogen or helium. It also confirms the previously mentioned hypothesis that the plasma electrons which are kicked by the electron-beam driver have a much better ability to ionize additional electrons by collision ionization than the electron beam. The simulation and theoretical analysis show that the plasma electrons accelerated by the electron drive beam in transverse direction are in the right range of energy to cause substantial additional ionization and could be responsible for the ionization effect. The electron spectrum does not

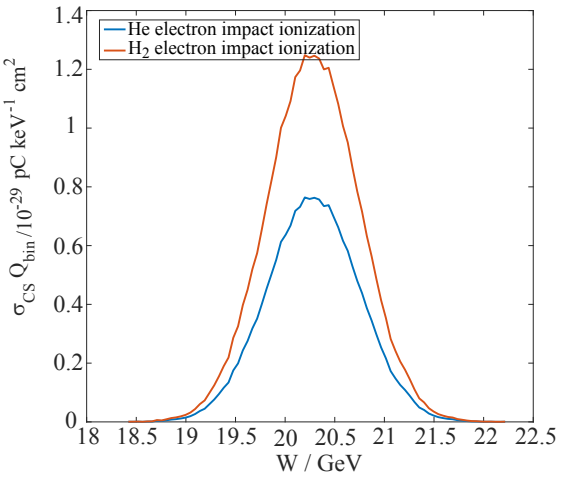

Figure 7.11: Product of FACET-beam-like electron spectrum with mean energy at 20.35 GeV with the ionization injection cross section for He (blue curve) and for H (red curve). At such high electron momenta, the cross section is approximately constant over several GeV, so that the graph resembles the momentum distribution of the electron-bunch. The values are many orders of magnitude smaller than those for the plasma electrons shown in figure 7.10, which explains the low ionization capability of the electron bunch.

overlap perfectly with the maximum of the ionization cross sections, but due to thermalization the plasma-electron spectrum shifts to lower energies over time.

This also means that the method can work with lower peak-current electron beams with lower radial electric fields, which makes this an important technique with potential applicability for a wide range of accelerator systems.

8

RESULTS OF INJECTION EXPERIMENTS

The experimental program conducted by the E210 collaboration at FACET demonstrated controlled injection of electron bunches into a plasma wake via two methods, the Plasma Torch Injection and the Trojan Horse Injection. In this chapter, the analysis and discussion of the obtained data are presented. First, a calibration for the two charge-measuring devices, the BPMs and the DRZ screen is presented in section 8.1. Then, the results for the Plasma Torch Injection are discussed in section 8.2. Finally, section 8.3 presents the transition between the Plasma Torch Injection and the Trojan Horse Injection regime.

8.1 CHARGE CALIBRATION

The witness-beam charge is measured with two different methods: by measuring the difference between the charge before and after the plasma section and by observing the electron-bunch on a scintillating screen. Several devices were available to measure the charge propagating in the electron beam-line. Toroidal Current Monitors (toroids) before and after the plasma section are the typical diagnostic tool to measure the bunch charge in the accelerator. There are two reasons, however, why we decided to rely on the charge difference measured by the beam position monitors (BPMs) instead.

The first reason is that the toroid after the plasma section turned out to be vastly over-estimating the additional charge. For example, it measured up to several nC of excess charge. PIC-simulations imply that the injection of a witness-bunch charge that exceeds the drive-bunch charge is unlikely. For the same shots, the BPMs obtained much more consistent values. Our interpretation was that toroids respond with too strong a signal to a direct hit by electrons that leave the plasma section with a high divergence. The BPMs apparently have not been affected by such effects, which could be due to the larger aperture of the BPMs compared to that of the toroids.

The second reason to choose the BPM charge data over the toroid charge data is a more scientifically profound one. In order to compare the charge before and after the interaction, the charge-measuring devices should balance the excess charge to $\Delta Q = 0$ in vacuum, or show an offset since no drive-beam charge should be lost in vacuum. This offset must be constant and should not vary too much over several days. Figure 8.1 a) shows the offset between the charge measured by the BPMs nearest to the interaction point upstream (USBPM) and downstream (DSBPM) of it. Each scatter point shows the mean and the standard deviation of the charge

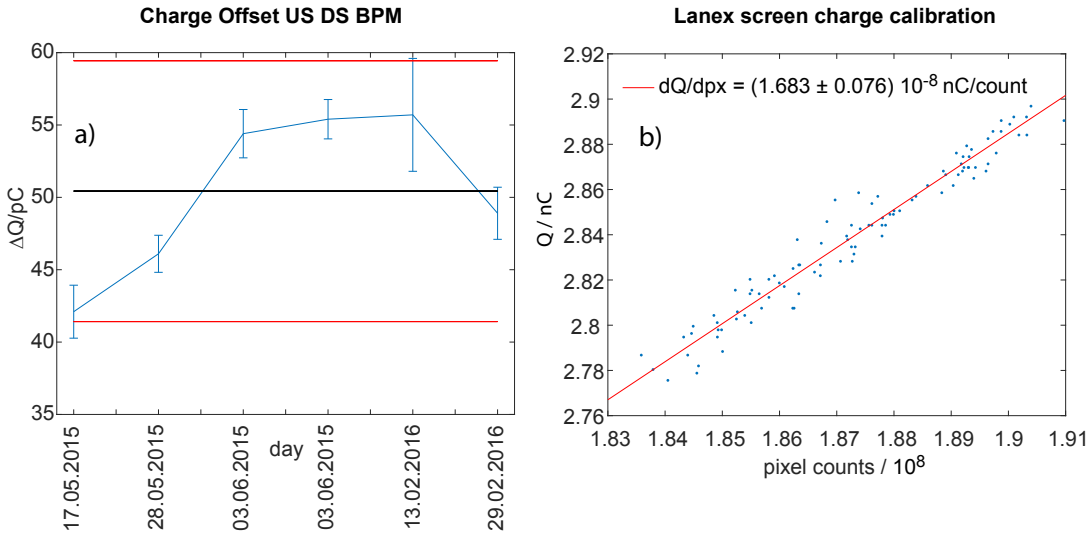

Figure 8.1: Calibration for both ways of charge measurement. The statistical offset between USBPM and DSBPM as measured on different days spread over 9 months (a) shows good stability for a mean value of 50.4 pC. A confidence interval of ±9 pC is chosen to make datasets on different days comparable, which is clearly much larger than the dataset rms deviation. (b) shows the pixel-count-to-charge calibration on the DRZ lanex screen with an Neutral Density ND2 filter inserted in front of the camera to attenuate the scintillating light, which would otherwise overexpose the camera.

difference between USBM and DSPM of one dataset with at least 100 taken shots. The black line depicts the long-term mean of

$$\Delta Q^{\text{offset}} = 50.4 \pm 9.0\,\text{pC}. \tag{8.1}$$

The long-term confidence interval is indicated by the red lines. Among all possible combinations of charge-measuring devices, the difference between the charged measured by USBPM and DSBPM showed the most stable long-term offset and least variation per dataset. Therefore, for the analysis discussed in this work, USBPM and DSBPM were applied to determine the excess charge.

The second method to measure the witness-bunch charge is to observe it on the scintillating screen of the spectrometer where the drive bunch and the witness bunch are transversely separated due to their different energies. LANEX screens are an advantageous material as a diagnostic for electron bunches because of their good radiation hardness and their linear scintillation-light response to charge over a large range of electron energies and charge densities [134]. For laser-driven accelerators, the charge calibration of LANEX screens can be a difficult task, because a reference signal is required. In PWFA experiments, a well-understood electron beam is conveniently available as a reference. In the experiment, a LANEX screen of the type DRZ [112] was used.

Figure 8.1 b) shows the analysis of the charge calibration. If no precautionary measure is taken, the scintillation signal of the full charge $\approx 3\,\mathrm{nC}$ FACET electron bunch on the DRZ screen saturates the CMOS camera. Therefore, the electron bunch was scattered at a thin foil to broaden the signal. In addition, a neutral density ND 2 filter with a broadband transmission of $T = 0.01$ was inserted in front of the camera. After background subtraction, the image was cleaned of additional signal from X-rays with a morphological opening filter. In figure 8.1 b), the sum of the pixel counts of the post-processed image is plotted against the charge measured by a toroid upstream of the IP area. The linear dependence between charge and scintillation light is expected and indicates that scintillation-light triggered by secondary radiation such as bremsstrahlung did not distort the signal in a measurable manner. In contrast to the electron drive bunch, many of the low-charge witness bunches could not be detected by the DRZ screen when the ND 2 filter was inserted in front of the camera. Therefore, these images were taken with the ND filter retracted, which is why the charge calibration for witness-bunch measurement on the DRZ screen is corrected by the transmission of the ND filter to

$$Q_{\mathrm{calib.}}^{\mathrm{DRZ}} = (1.683 \pm 0.076) \times 10^{-6}\,\mathrm{pC/count}. \tag{8.2}$$

8.2 EXPERIMENTAL RESULTS FOR THE PLASMA TORCH INJECTION

The Physics of Plasma Torch injection is described with theory and simulations in section 2.8.3. In the course of the experimental campaign, we studied the feasibility of the injection mechanism and demonstrated the first laser-controlled witness-bunch injection in PWFA. As described in section 2.8.3, simulations show that electron-bunches can be injected and accelerated by the Plasma Torch density spike, even in the absence of a pre-ionized plasma.

In this case, the electron drive bunch ionizes the gas and drives a wake in the generated plasma. Of course, this depends heavily on the drive-bunch focusing and emittance. Judging by the cameras which observed the recombination light in cube 3 and cube 4, beam-ionized hydrogen and subsequent PWFA rarely occurred as the result of the beam fields operating at about the hydrogen ionization threshold and was certainly not stable over a sequence of shots. It is possible that the light emitted by such a small plasma volume as generated by the electron bunch

is below the detection threshold of the cameras[1]. To test whether charge can be accelerated by the Plasma Torch Injection method, the roll-scan that was conducted for the data shown in figure 7.9 was further analyzed. For that dataset, the focus of the OAP was scanned over the electron-beam orbit. The optimum alignment could be determined from the intensity of the light emitted by the plasma (see section 7.3). In figure 8.2, the excess charge as measured by the BPMs, corrected by the constant offset, is plotted over the OAP focus position, as determined by the focus diagnostic. The zero position is determined by the enhanced recombination light method described in section 7.3. Comparing the data points for good alignment and off-

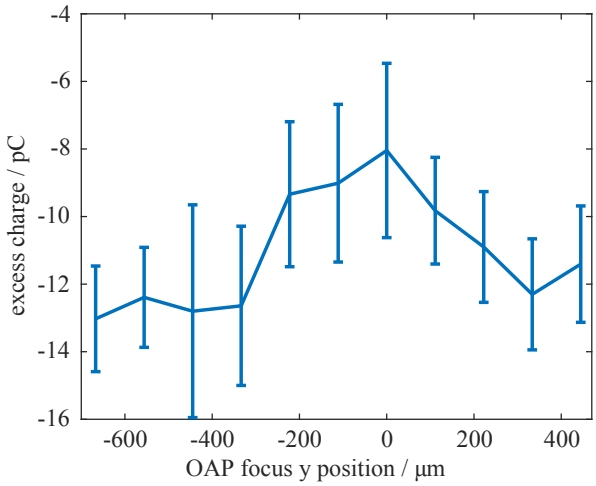

Figure 8.2: Charge difference between DSBPM and USBPM versus focal position. The data is taken from the same dataset as the one shown in image 7.9. The zero-position is determined by the maximum of the recombination light.

alignment between electron beam and injection-laser focus, a charge difference of $\approx 6\,\mathrm{pC}$ was measured. Although the long-term confidence interval is slightly larger than the measured charge difference (see figure 8.1 a), the standard deviation in a single dataset on a given day is smaller so that we can conclude an indication of Plasma Torch injected charge.
However, in the case of a pre-ionized plasma, the effect of the injection laser is much stronger due to longer acceleration lengths and a more stable wake. In figure 8.3, histograms of excess charge are plotted for pre-ionized datasets. They clearly show more accelerated charge for the data with the injection laser switched on (red bars) compared to the data with the injection laser switched off (blue bars). Plot (a) shows all measured shots while (b) shows only shots with a witness bunch detected as an electron population distinct from the drive-bunch energy on the spectrometer. Such a signal on the spectrometer is not only a confirmation of witness-bunch injection, it is also a quality indicator of the witness bunch. The energy spread and divergence

1 It should be noted that, during the hydrodynamic density-downramp injection experiments, the E215 collaboration achieved a stable beam-ionized plasma including the observation of drive-beam deceleration. However, this was only possible by a very strong compression of the electron beam to $\approx 20\,\mu\mathrm{m}$ rms bunch length and stronger focusing with the waist set to $\approx 1\,\mathrm{m}$ upstream of cube 3.

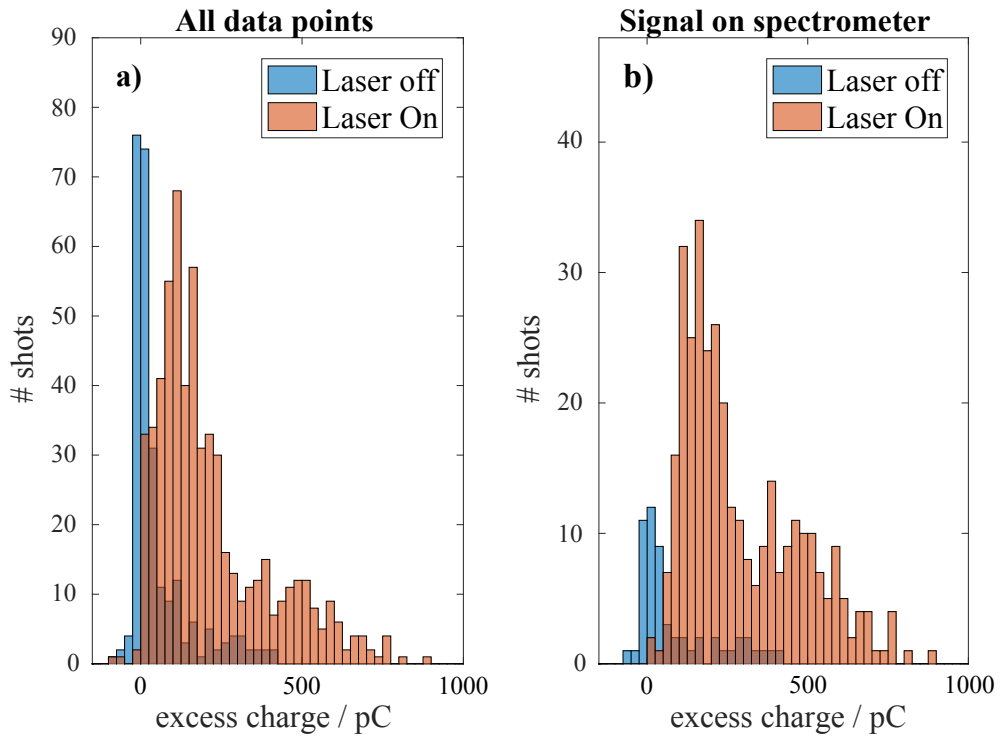

Figure 8.3: Charge statistic comparison between laser on and laser off cases. The excess charge is the charge difference measured by USBPM and DSBPM. All data points (a) are compared to data points with a witness bunch detected on the WLANEX spectrometer screen (b). The bars are plotted partly transparent, which leads to a dark red area for overlapping histogram bars.

of the witness bunch needs to be small enough to be transported by the quadrupoles QS1 and QS2 to the DRZ screen[2]. Applying the condition that a witness bunch needs to be identified by the spectrometer data clearly sharpens the difference between the Laser-On and Laser-Off data. Interestingly, the Laser-On data seems to consist of two populations, one with a peak at 165 pC and one with a peak at 465 pC. Before the data was taken, the electron-bunch rms sizes were measured to be $28.1\,\mu\text{m} \times 28.4\,\mu\text{m} \times 21.6\,\mu\text{m}$ in x, y, z respectively and the laser delivered ≈ 650 mJ laser energy measured in the laser room.

Timing-dependent Plasma Torch injection

The availability of precise laser-to-electron-bunch timing information by the EOS gave us the possibility to scan the TOA of the injection laser with respect to the TOA of the electron bunch to study the time dependence of the Plasma Torch Injection mechanism. A very interesting dataset, 20319, is analyzed in this section. This dataset was taken about two weeks after the On/Off scans shown in figure 8.3. During these weeks, one of the Saga pump lasers for the main laser amplifier had been replaced by a continuum pump-laser, because the flash-lamps of the

2 Quantitative evaluation of the spectrometer and of cut-off values that would lead to the witness-bunch being lost in the beam line to the spectrometer, are beyond the scope of this work, but will be further analyzed in the future.

Saga pump-laser kept failing. This brought the laser energy back to 500 mJ at the transport beamline entrance, but changed the form of the transverse laser modes, which had an influence on the focus intensity distribution of the axilens and of the OAP. The axilens focusing was also altered because a different axilens had been installed. The 4-1 axilens which provides a design line focus of 1 m starting 4 m downstream of the axilens surface had to be replaced with a 3-1 axilens with a design line focus of 1 m starting 3 m downstream of the axilens surface. In order to ensure the correct starting position of the plasma, the axilens was also moved downstream by 1 m. These changes altered the quality of the plasma in such a way that the data taken shown in figure 8.3 only allows for a qualitative comparison. The x, y, z electron-bunch size

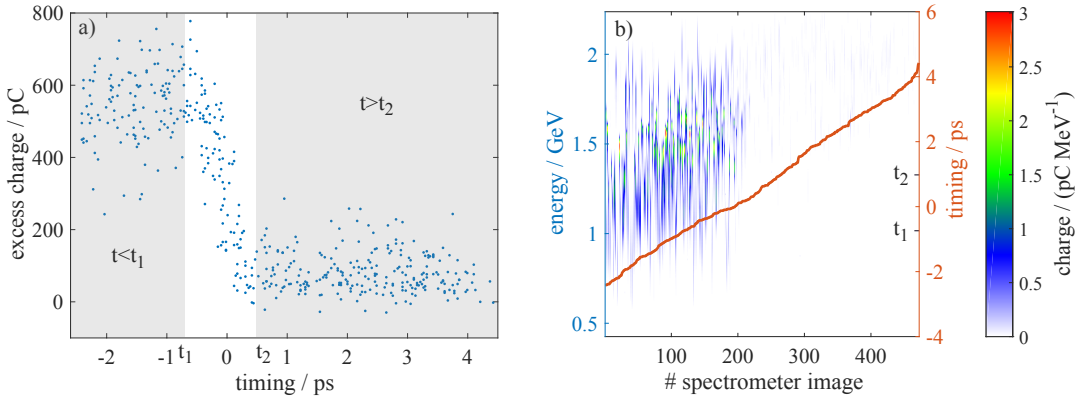

Figure 8.4: Difference in charge measured by USBPM and DSBPM plotted over relative laser to electron-bunch TOA, which was measured by the EOS (a). The waterfall plot of the witness-beam spectrum sorted by EOS timing shows a lower energy at higher charge densities in the region with laser coming clearly earlier then the electron beam($t < t_1 = -0.75\,\mathrm{ps}$) compared to the laser-after-electron-bunch cases ($t > t_2 = 0.5\,\mathrm{ps}$).

was measured at the beginning of the shift to be $26.9\,\mu\mathrm{m} \times 18.3\,\mu\mathrm{m} \times 27.5\,\mu\mathrm{m}$ and to be $32\,\mu\mathrm{m} \times 45\,\mu\mathrm{m} \times 27\,\mu\mathrm{m}$ at the end of the shift at 10 am the next morning.

Figure 8.4 shows a scatter plot of excess charge as measured by the BPMs around the plasma section plotted against timing as measured by the EOS. The scan over relative timing is set by changing the delay between the laser oscillator and the main RF reference. The pre-ionization laser arm was set up to arrive at the IP at least $1,\mathrm{ns}$ ahead of the electron bunch. The data points in figure 8.4 a) can be divided into three different timing regimes. Timing values $t < t_1$ correspond to a situation in which the injection laser arrives at its focus earlier than the electron beam. Timing values $t > t_2$ correspond to the electron beam arriving earlier than the laser pulse. These two regimes, as regards Plasma Torch injection, are effectively identical to the previously measured Laser-On-Off datasets with the difference that additionally the transition between $t_1 < t < t_2$ was measured. A waterfall-plot of the witness-bunches, measured at the spectrometer and sorted by EOS timing is shown in figure 8.4 b). The spectrometer data confirms the BPM measurement, showing low injected charge in the dark-current parameter

regime and high charge injected in the Plasma Torch Injection regime. It also reveals an interesting detail: the Plasma-Torch-injected witness bunches reach lower energies than the dark current. A statistical analysis of both data populations is presented in figure 8.5. The average

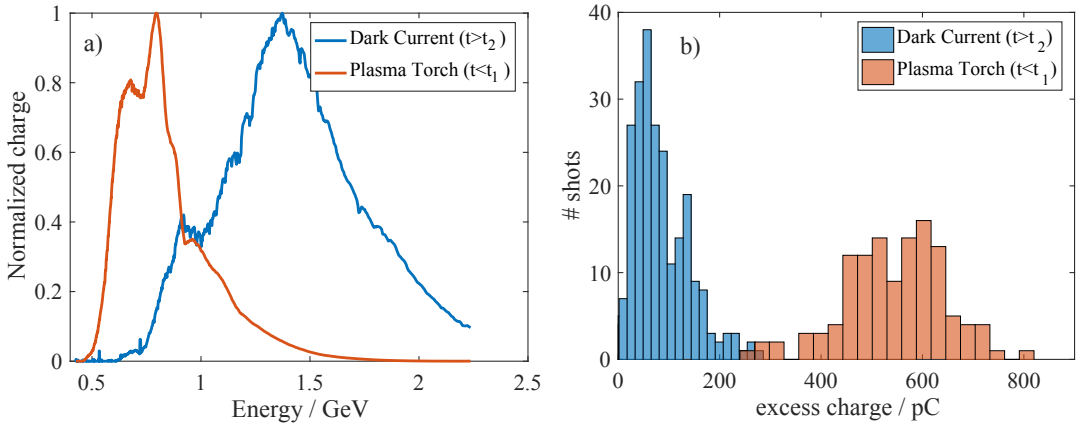

Figure 8.5: Normalized mean spectrum of injected electron bunches for Plasma Torch injection timing regime and for the laser arriving after the electron bunch (a) and histogram of charge for the same populations (b). The timing regions are illustrated in figure 8.4.

spectrum shown in figure 8.5 a) is a normalized mean over 120 data points for $t < t_1$ and 240 data points for $t > t_2$, which corresponds to a timing regime for Plasma Torch Injection and a low-charge dark-current regime with unknown injection mechanism. The analysis shows for the Plasma Torch regime a peak energy at

$$W_{\text{peak}}^{\text{PlaTo}} = 0.79\,\text{GeV}. \tag{8.3}$$

The dark-current energy peak is measured at

$$W_{\text{peak}}^{\text{DC}} = 1.37\,\text{GeV} \tag{8.4}$$

and shows a broader distribution. The spectrometer in its current configuration cannot deliver reliable quantitative information about energy spread. Since the witness-bunch energies are very low compared to the design parameters of $\approx 20\,\text{GeV}$, divergence either inherent to the witness bunch after the plasma or due to scattering at the diamond window blurs out the spectrometer image. However, the energy spread is least blurred out at the pinch set by the quadrupole, which was 1.7 GeV while taking this dataset. This means that the energy spread is more over-estimated for the Plasma Torch data then for the dark-current data. Since the energy spread as measured by the spectrometer is smaller for the witness bunches injected in the Plasma Torch Injection timing regime than in the dark-current timing regime it can be concluded that the energy stability and energy spread should be qualitatively smaller for the witness bunches injected by the Plasma Torch injection mechanism. PIC simulations show that due to the linear accelerating field in the blowout regime, the witness bunches injected by the Plasma Torch Injection method accumulate a negative energy chirp with the electrons at the

back of the witness bunch at highest energy. Such a negative chirp would mean a correlation $\xi \propto -W$ between energy W and longitudinal position ξ such that the longitudinal current profile would look like the red graph shown in figure 8.5 a) when flipped along the energy axis. Figure 8.5 b) compares the BPM excess charge histograms. As already expected from figure 8.4 a), the Plasma Torch injected electron population shows a much larger charge with a mean value of

$$< Q_{\mathrm{PlaTo}} >= 545.0 \pm 102.2\,\mathrm{pC}. \tag{8.5}$$

The measured dark-current charge is smaller, having a mean charge of

$$< Q_{\mathrm{DC}} >= 81.8 \pm 56.8\,\mathrm{pC}, \tag{8.6}$$

which qualitatively confirms the result of the analysis comparing Laser-On-data to Laser-Off-data.

The finding that the dark current has lower charge but higher energy compared to the witness bunches injected in the Plasma Torch Injection timing regime can be explained in several ways.

The difference in spectra can arise from different **acceleration lengths**, **trapping positions** or from **beam-loading effects**. Simulations can give a better insight into a possible interpretation. Figure 8.6 shows a 3D PIC simulation snapshot after a propagation of 11 cm in a plasma column at a plasma density of $n_{\mathrm{e}} = 1.7 \times 10^{17}\mathrm{cm}^{-3}$. The driver bunch is compressed by the wake fields and drives a blowout with peak accelerating fields of $67\,\mathrm{GV/m}$.

A difference in acceleration length, which means that the dark current was injected at an earlier z position than the Plasma Torch injected witness bunches is possible, because an energy deviation of $\Delta W = 0.58\,\mathrm{GeV}$ does require an offset in z injection position of only a few cm. It is not precisely known at which z position the plasma starts or how long it was because scanning the plasma length was risky for the integrity of the diamond window. It is believed that the plasma started a few cm upstream of the OAP focus. However, this explanation requires the additional assumption that the injection of dark current only happens upstream of the OAP focus, which cannot be proven right nor wrong by the experimental data.

Different trapping positions in the co-moving frame ξ for witness bunches from Dark Current and injected with Plasma Torch can be an explanation, taking the large accelerating fields from simulations shown in figure 8.6 into consideration. The length of the plasma per shot is not exactly known, but laser-pulse parameter jitter did result in large changes of the plasma length. It can be estimated from cameras that imaged the plasma light to be at least 10 cm long. For such an acceleration length, a trapping position difference of $\Delta\xi_{\mathrm{trap}} \approx 3\,\mu\mathrm{m}$ corresponds to a deviation in accelerating field by $\Delta E_{\mathrm{z}} = \frac{\Delta W}{0.1\,\mathrm{m}} = 5.8\,\mathrm{GeV/m}$ according to PIC simulations. This is already sufficient to explain ΔW.

On top of these effects, beam loading, the suppression of accelerating field by the witness beam's space charge, may also have played a role, given the large charges involved and the fact that the witness bunches with the largest charge are accelerated to lower energy. Even though the difference in energy and charge can be explained by a few physical effects, beam

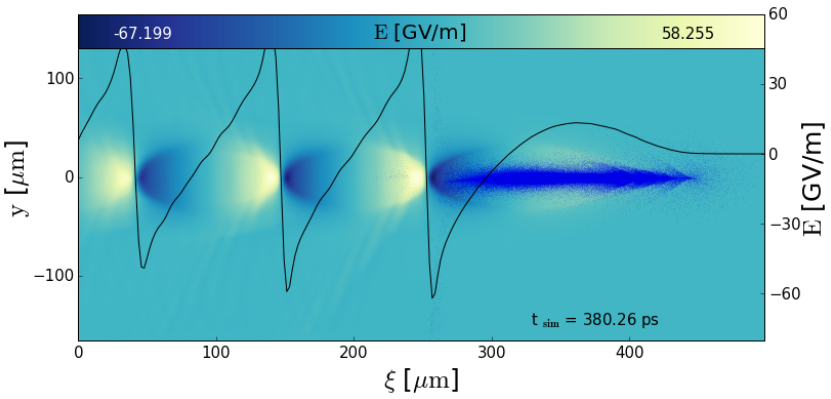

Figure 8.6: Snapshot of PIC simulation of PWFA after 31.4 cm of propagation through plasma with plasma density $n_e = 1.7 \times 10^{17}\,\mathrm{cm}^{-3}$ and an Gaussian electron-bunch with sizes as measured during the shift. A cut through the on-axis accelerating electric field E_z (black line) is shown. The simulation was conducted by T. Heinemann and analyzed by the author.

loading is an effect that also explains the low energy spread of the witness bunches injected via the Plasma Torch.

8.3 EXPERIMENTAL RESULTS FOR THE TROJAN HORSE INJECTION

For Trojan Horse Injection, the injection-laser pulse needs to have the correct timing to release electrons inside the plasma wake trailing the drive electron-bunch. It is easier to inject into the first wake because it has the strongest fields and is the most stable with regards to transverse fluctuations of the wake excitation. Therefore, the correct relative timing between electron bunch and laser pulse for Trojan Horse Injection should be found in the vicinity of the transition shown in figure 8.4, which marks the time frame in which electron bunch and laser pulse overlap. Unfortunately, figure 8.4 a) does not reveal any sign of Trojan Horse Injection, but this data was taken with the injection laser at full energy, i.e. 5 mJ on target, which is much more energy than simulations predicted to be necessary for a successful Trojan Horse Injection. We assumed that there are two possible reasons why no evidence of Trojan Horse Injection up to that point was seen. Either there is a mixed regime in which both Plasma Torch Injection and Trojan Horse Injection is possible but the Trojan Horse Injection cannot be identified in the data because the injected charge is dominated by the Plasma Torch injected electrons, or the laser pulse released too much charge inside the volume of the plasma wake so that the space charge inhibits trapping[3].

Either explanation implied that lowering the energy of the injection laser should reveal Trojan Horse injected witness beams in the timing scans. This strategy was as simple as it was experimentally challenging.

3 Simulations carried out after the experimental campaign confirm the existence of such a mixed regime.

The minimum requirement to take a sequence of timing scans with different injection laser-pulse energies was an experimental shift without dark current. This depended a lot on the drive-beam quality. It had to be sufficiently symmetric and could not be compressed too strongly or else the beam electric fields would ionize helium and inject it. Nevertheless, the compression needed to be strong enough to reliably excite a strong plasma wake. The electron-bunch orbit additionally needed to be stable over several hours so that enough datasets could be taken. Thanks to the great work of Nate Lipkowitz, who wrote an orbit stabilization tool and commissioned it in only a few days, drifts in the electron-beam orbit, which built up over tens of minutes, could be effectively minimized. The second major device that needed increased stability was the laser. We had to keep three laser arms aligned, the EOS, the pre-ionization laser and the injection laser.

The EOS was the least troublesome of the laser arms. After its commissioning in dedicated shifts, its preparation eventually became routine alignment work that took around half an hour at the beginning of each shift.

The alignment of the injection laser was done with the help of OTR screens as described in section 6 and then monitored by the enhanced recombination light diagnostic described in section 7.3, which saved hours of re-alignment during the shifts. The alignment of the pre-ionization laser however, also needed continuous attention. An alignment of the pre-ionization laser required pumping the hydrogen and helium gas out of the vacuum chambers, alignment of the laser to the electron-beam signal on the OTR screens and then venting the chambers again with hydrogen and helium gas. This procedure took at least 20 minutes, but more often several hours, during which no data could be taken. To maximize the duration between repeating this time-consuming procedure, we relied on plasma-electron-beam interaction.

It can be assumed that in the case of a perfect plasma-to-orbit alignment, the electron beam would not feel any transverse kicks from the wake field. In the case of a transverse misalignment, however, the transverse wakefield is asymmetric and alters the trajectory of the electrons at the tail of the bunch. These kicks can be measured by the BPMs downstream of the plasma section. The procedure consisted of the following steps: First, we turned off the quadrupoles of the imaging spectrometer and blocked the laser. Then, we took the angle of the electron bunch without any plasma interaction as measured by the BPMs downstream of the plasma section as a reference. To address short-term jitter in alignment, a mean over 10 consecutive shots was taken. After that, we unblocked the pre-ionization laser and ionized the plasma. In case of a good plasma-to-orbit alignment, the BPMs measured a similar angle. In the case of small angular misalignment, the pre-ionization laser was then adjusted until no kick was observable anymore. The physics of transverse kicks in PWFA was also studied by Adli et al. [135].

With an optimized procedure, we could maintain conditions stable over several hours. The drive electron-bunch rms size before the shift was measured to be $27.9\,\mu\mathrm{m} \times 10.2\,\mu\mathrm{m} \times 34.3\,\mu\mathrm{m}$ and after the shift in the early morning these values were $24.3\,\mu\mathrm{m} \times 19.8\,\mu\mathrm{m} \times 37.6\,\mu\mathrm{m}$. The result of this beam shift is condensed into figure 8.7. Several timing-scan datasets were taken

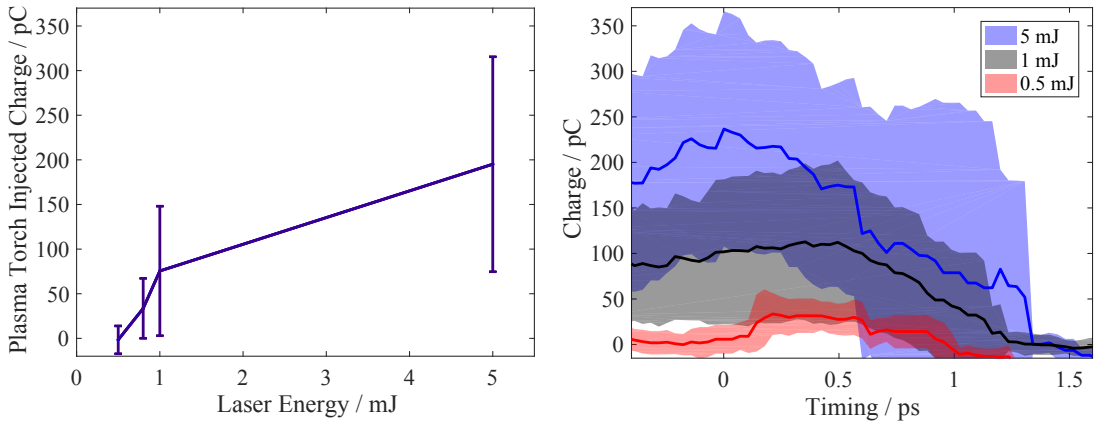

Figure 8.7: Mean excess charge measured by BPMs with signal on spectrometer and for timing values $t < 0$ (a). Timing scan for different injection laser energies (b). Only datapoints showing a witness beam on the spectrometer are counted. The moving average over charge measured by BPMs is shown, revealing the transition from Plasma Torch Injection to Trojan Horse Injection.

and evaluated with 0.5 mJ, 0.8 mJ, 1 mJ and 5 mJ laser energy. Inset (a) shows a plot of the mean excess charge measured by the BPMs over data points with timing $t < 0$ with the standard deviation as error bars plotted over the energy of the injection laser. The timing value $t = 0$ is defined by the plasma recombination light diagnostic, described in section 7.3 and corresponds to a timing regime in which only Plasma Torch Injection can be expected. Only data points for which a clear proof of a witness-beam injection is given by the spectrometer are taken into account for inset (a) and (b). The curve shows that the Plasma Torch-injected charge decreases with decreasing laser energy, as expected. Inset (b) shows the running average of the excess charge taken over 6 EOS pixel positions, which corresponds to averaging over a relative timing of 150 fs for each EOS pixel. The data with 5 mJ injection laser energy clearly shows a behavior that fits the Plasma Torch Injection, with a transition from no injection, in the case of the laser pulse incident after the electron beam ($t > 1.4\,\mathrm{ps}$) to injection, which occurs for small timing values. The 1 mJ data shows a transitional behavior between the 5 mJ case and the 0.5 mJ case. At 0.5 mJ injection laser energy, a hump with 0.6 ps FWHM length can be seen. This is equal to the expected values given a plasma wavelength of 93 μm$\hat{=}$309 fs, a minimum FWHM laser focal spot size of 94 μm$\hat{=}$313 fs and a laser pulse length of 60 fs, which is evidence for Trojan Horse Injection, a laser-triggered ionization injection into a Plasma wake in the blowout regime.

9

SUMMARY

The work presented in this thesis is a major step towards controlled witness-bunch injection in PWFA and contains experimental, numerical and theoretical results. It comprises experimental achievements obtained jointly with the colleagues in the E210 collaboration including my Ph.D. colleagues from University of Hamburg and Strathclyde such as Oliver Karger, Thomas Heinemann and Paul Scherkl.

Several novel results have been obtained within the E210 collaboration. Enabling techniques for spatio-temporal alignment of up to 2 laser beams to the SLAC electron beam have been developed. Among those, a novel plasma-based laser-to-electron-bunch synchronization method was developed, analyzed and sub-ps synchronization was established. We expect that the synchronization can be further improved in a geometry in which electron-bunch and laser-pulse trajectories are parallel and not perpendicular. The method could in future be useful not only for any kind of PWFA experiment that relies on laser synchronization but also for synchronization in pump-probe experiments for example at experiments including a free-electron laser. A second technique which enhanced state-of-the-art diagnostics at FACET with plasma-based response signals was the alignment between preionization laser and electron-beam driver, which utilized the transverse plasma kick in case of misalignment. Both methods have proven to be essential for the success of E210, as they enabled alignment, accelerated the alignment procedures and have demonstrated a robustness and sensitivity which rivals those of the current methods. Several injection mechanisms could be demonstrated in this work. The Plasma Torch injection is a very important tool now available to the PWFA community. Evidence of Plasma Torch injection is not only proof for density downramp injection in PWFA, it is also possible now to build a PWFA setup in which witness-bunch injection can reliably be switched on and off by the laser. This gives the option to work on tailored laser-controlled plasma shapes that enable control over witness-bunch parameters such as charge and peak current.
The proof-of-principle demonstration of Trojan Horse injection is clearly the most important experimental result presented in this thesis. Experimental evidence for ionization injection triggered by a laser opens up a multitude of applications that benefit from ultra-low emittance electron bunches such as photon sources. In this work, no precise measurement of the expected ultra-low emittance as anticipated by simulations is presented. A refined analysis of the data with a focus on the emittance goes beyond the scope of this work but will be addressed in the future. Future experiments, continuing the research on Trojan Horse Injection, should work in a co-propagating geometry between electron bunch and injecting laser pulse to realize ultra-low emittances and high brightness values. Gradual improvement in the accuracy and stability

of the electron accelerator and laser system will also greatly benefit control over the injection. One lesson learned from many of the beam shifts was that for a driver beam with up to 17 kA peak current such as the FACET beam, unwanted dark current could easily appear. Therefore, techniques to mitigate dark current have been developed. One result is to mitigate dark current by lowering the peak current of the driver bunches.

The development of the downramp-assisted Trojan Horse injection with simulation and theory is a core part of this work and presents a viable solution to realize Trojan Horse Injection with these low-current driver bunches. Since it is more difficult for weaker driver-bunches to trigger injection, the injection can be limited to a region with reduced phase velocity such as on a hydrodynamic density downramp. The witness bunches with ultra-low emittance values that can be generated by this method as well as advanced control over the witness-bunch length and its longitudinal current profile are key advantages that can make it particularly interesting for future applications.

10

OUTLOOK

We will now take a glimpse into the future and describe some of the near- and longer-term prospects.

FACET II

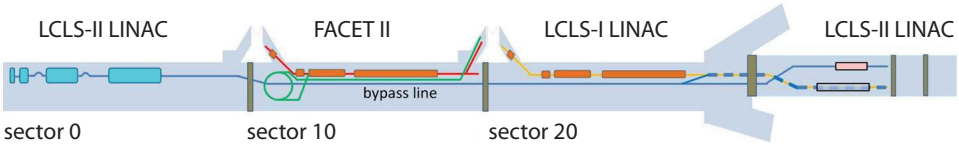

Figure 10.1: Sketch of planned FACET-II and LCLS-II beamline. Image is post-processed from reference [99].

In 2016, FACET stopped its experimental operation and is currently being upgraded to FACET II [99]. FACET II will operate at 10 GeV, half of the FACET beam energy. The smaller FACET II beamline will make room for the LCLS II beamline. FACET II will have a photocathode that is expected to give a much better timing stability so that timing-sensitive experiments such as Trojan Horse Injection will become easier. It can also be expected that the FACET II electron beam will have lower emittance than the FACET beam. This will give the option to focus more tightly and stabilize the orbit so that a faster preparation of the accelerator before each shift can be expected. While beam time can be expected to become of better quality and more frequently available in comparison to FACET, the access time for maintenance will more strongly depend on the LCLS maintenance plan, which may lead to less available maintenance time. With lower total energy and a better control over electron beam orbit and laser system, FACET II will have the potential for groundbreaking results such as the demonstration of bunch depletion from electron bunch to positron bunches, or FEL radiation from injected witness bunches.

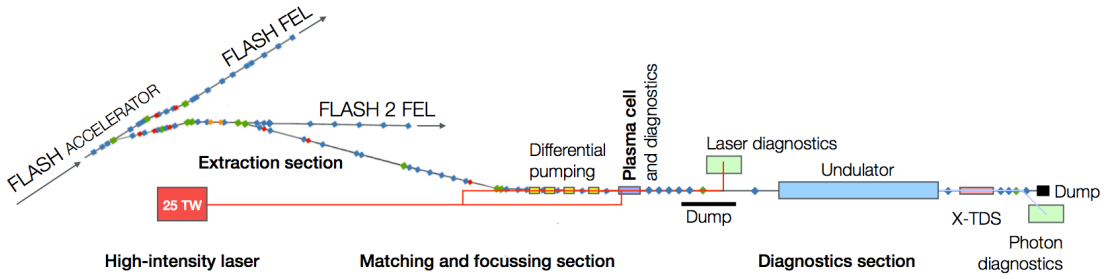

Figure 10.2: Sketch of planned FLASHForward beamline. Electron bunches are extracted from the FLASH2 beamline. Image is post-processed from reference [136].

A PWFA laboratory on the verge of starting operation in 2017 is the *Future-oriented wakefield accelerator research and development at FLASH* (FLASHForward) [78] located at the FLASH accelerator at DESY in Hamburg. The FLASHForward facility is part of the FLASH accelerator as can be seen from the sketch in figure 10.2. Single electron bunches will be extracted from the bunch train in the FLASH 2 arm of the accelerator. Therefore, the experimental operation will mostly happen parasitically to FLASH II operation. At FLASH, electron bunches are generated on a CsTe photocathode and injected by an L-band (1.3 GHz) RF gun. The bunches are accelerated to 150 MeV and then compressed in a chicane to ca. 2 mm bunch length. After further acceleration to 450 MeV, the bunches are compressed a second time to approximately 20 μm FWHM and then further accelerated. At the extraction section, where the bunches are kicked into the FLASH, FLASH 2 and FLASHForward beamlines, the electron bunches are at the final energy of 1.25 GeV. Due to the very low energy-jitter and a well-developed timing system, FLASH provides a few-fs synchronization between electron bunch and laser pulse [137]. The peak current expected to be available at FLASHForward is 2.5 kA. The fact that the FLASH accelerator is a super-conducting linac leads to stringent vacuum requirements at FLASHForward. Therefore, FLASHForward will not operate with a filled gas volume but with a constant-flow gas cell. The upstream accelerator will be protected by a differential pumping system, which, in contrast to a window, does not spoil the electron-bunch emittance. An advantage of constant-flow gas cells compared to a filled gas volume is that gas density profiles can be altered remotely, which makes FLASHForward the perfect laboratory for the realization of a downramp assisted Trojan Horse Injection as described in chapter 4.

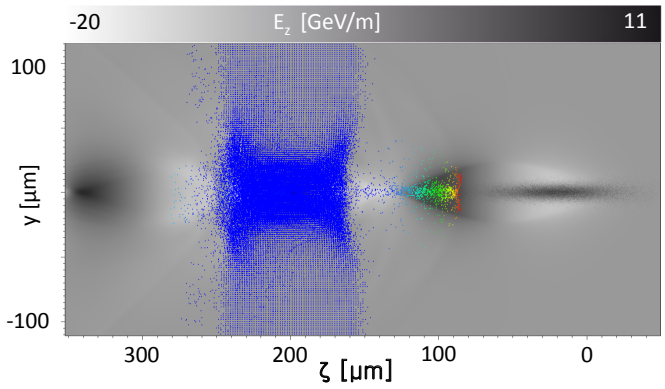

Figure 10.3: 3D PIC simulation result for a drive bunch with FLASHForward parameters and 2.5 kA peak current. The image shows a snapshot of the simulation shortly after the passage through the Plasma Torch Injection density spike. A slice through the longitudinal electric field (gray) and the injected electron macro-particles show the nature of the injection method.

Drive beam peak current (kA)	Witness beam charge (pC)
2.5	78.9
2.0	34.7
1.5	24.3
1.0	0

Table 10.1: Table of trapped witness-bunch charge as a function of drive-bunch peak current. The latter is varied by charge only and not by spatial dimension to compare identical resonant wake excitation. No witness bunch was trapped below 1.5 kA Peak current.

Plasma Torch Injection at FLASHForward

For facilities with a drive beam at a rather low peak current such as the FLASHForward facility, Plasma Torch injection is an interesting option for witness-bunch injection. Figure 10.3 shows a snapshot of a PIC simulation for a FLASHForward drive bunch during Plasma Torch Injection. The colored macro particles represent the laser-ionized He electron macro particles forming the density spike. The parameters of the 500 pC drive bunch are set to a peak current of 2.5 kA and a trace space emittance of 2×10^{-6} m rad. The bunch is $\sigma_z = 24\,\mu$m rms long and $\sigma_r = 5\,\mu$m wide. The plasma density is $n_e = 4 \times 10^{16}\,\mathrm{cm}^{-3}$. The injection laser has a focal spot size of $w_0 = 60\,\mu$m at normalized peak intensity $a_0 = 0.03$ and laser pulse length typical for the FLASHForward laser of 25 fs FWHM. The peak current that can be reached at FLASHForward is a crucial value and stable parameters are yet to be experimentally determined. Table 10.1 compares injected witness electrons for drive-bunch peak currents in the range of $2.5 - 1.0$ kA. The currents were decreased by decreasing the charge, leaving all else equal. A successful witness-bunch injection is possible until 1.5 kA. These results suggest that Plasma

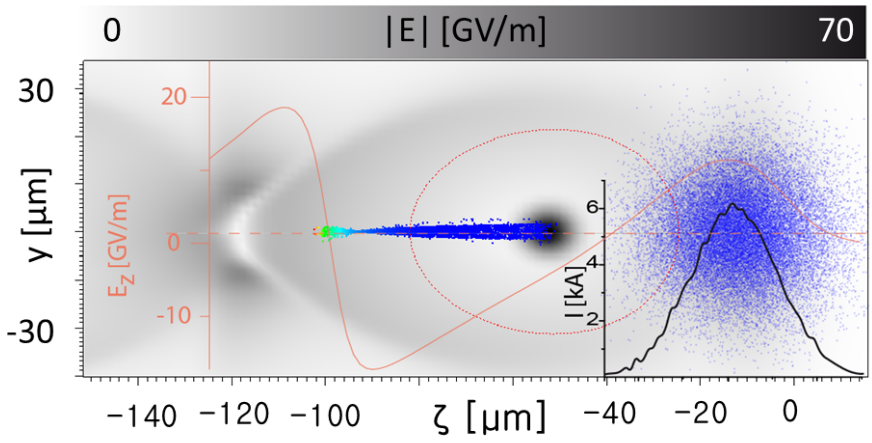

Figure 10.4: Simulation of Trojan Horse Injection for a FLASHForward-class driver beam at 6 kA peak current during injection. The red circle frames the volume from which the wake potential allows for trapping of released electrons.

Torch Injection experiments can indeed be conducted at the FLASHForward facility and several 10 pC witness bunches can be expected.

Trojan Horse Injection at FLASHForward

FLASHForward has access to very precise synchronization between laser pulse and electron bunch, which makes the facility a perfect candidate for advanced studies with the Trojan Horse Injection method. Parameter scans with 3D PIC simulations show that, for the standard 2.5 kA FLASHForward bunch, straightforward Trojan Horse Injection is not possible, because the wake potential is too shallow. A peak current of at least 6 kA is required in order to generate ultra-low-emittance witness bunches with the Trojan Horse mechanism. A snapshot of the simulation with 6 kA peak current during injection can be seen in figure 10.4. The witness bunch has a charge of only 3.2 pC, but it has a short bunch length of $\sigma_z = 0.2\,\mu\text{m}$ and a peak current of 1.5 kA. The emittance after phase mixing is ultra low with 1.4×10^{-8} mrad and the energy spread is 1.1 %. Such a drive electron bunch will need to be compressed to $\sigma_z^{\text{d}} \approx 10\,\mu\text{m}$ rms. In chapter 4 it is shown that only 2 kA drive-bunch peak-current is sufficient to enable the downramp-assisted Trojan Horse Injection, which could be an easier way to go. Since FLASHForward is not commissioned yet, it is difficult to be certain what can or cannot be done. It will depend on the measurements and experiences obtained in the fall of 2017 to determine which of the presented laser-triggered injection methods will be plausible for future investigation at FLASHForward.

An all-optical hybrid LWFA-to-PWFA accelerator

A long-term prospect of plasma wakefield acceleration is the hybrid use of LWFA and PWFA technology, which means that electrons, accelerated by means of LWFA drive a plasma wake in a second plasma source. This allows for injection methods like Trojan Horse injection or downramp-assisted Trojan Horse Injection. Hybrid LWFA-to-PWFA accelerators can have a very small footprint compared to conventional accelerators and a naturally synchronized laser system, because the injection laser can be a split off the accelerating LWFA laser-arm. In experiments at the JeTi laser at the institute for quantum optics (IOQ) in Jena, we have successfully demonstrated that passive plasma lenses cause a reduction of the divergence of LWFA-generated electron bunches [138]. A similar result has been obtained by Thaury et al. with the Salle Jaune laser at the Laboratoire d'Optique Appliquee[139]. Not only passive plasma lenses are considered in the field of PWFA and LWFA. Active plasma lenses that generate a focusing magnetic field due to the currents in a plasma discharge have recently become more attractive because they have strong transverse focusing fields with low chromaticity. Van Tilborg et al. measured that such active plasma lenses are feasible with only a few cm focal length[140]. Steinke et al. showed staging in LWFA, by combining an LWFA stage with an active plasma lens and a second LWFA stage[141, 142].
Another crucial step towards an all-optical LWFA-to-PWFA accelerator is the deceleration of the LWFA-generated electron bunches in a second plasma stage, which has recently been demonstrated[143]. The next important step to be addressed in the future will be to generate a witness bunch in a wake driven by an LWFA electron bunch.

BIBLIOGRAPHY

[1] John N Galayda et al. The lcls-ii project. *Proceedings of IPAC 2014*, 2014.

[2] Siegfried Schreiber and Bart Faatz. First lasing at flash2. In *Proc. FEL*, 2014.

[3] Massimo Altarelli, R Brinkmann, M Chergui, W Decking, B Dobson, S Düsterer, G Grübel, W Graeff, H Graafsma, J Hajdu, et al. The european x-ray free-electron laser. *Technical Design Report, DESY*, 97:1–26, 2006.

[4] BD Patterson, R Abela, HH Braun, U Flechsig, R Ganter, Y Kim, E Kirk, A Oppelt, M Pedrozzi, S Reiche, et al. Coherent science at the swissfel x-ray laser. *New Journal of Physics*, 12(3):035012, 2010.

[5] B. Aune, R. Bandelmann, D. Bloess, B. Bonin, A. Bosotti, M. Champion, C. Crawford, G. Deppe, B. Dwersteg, D. A. Edwards, H. T. Edwards, M. Ferrario, M. Fouaidy, P.-D. Gall, A. Gamp, A. Gössel, J. Graber, D. Hubert, M. Hüning, M. Juillard, T. Junquera, H. Kaiser, G. Kreps, M. Kuchnir, R. Lange, M. Leenen, M. Liepe, L. Lilje, A. Matheisen, W.-D. Möller, A. Mosnier, H. Padamsee, C. Pagani, M. Pekeler, H.-B. Peters, O. Peters, D. Proch, K. Rehlich, D. Reschke, H. Safa, T. Schilcher, P. Schmüser, J. Sekutowicz, S. Simrock, W. Singer, M. Tigner, D. Trines, K. Twarowski, G. Weichert, J. Weisend, J. Wojtkiewicz, S. Wolff, and K. Zapfe. Superconducting tesla cavities. *Phys. Rev. ST Accel. Beams*, 3:092001, Sep 2000. doi: 10.1103/PhysRevSTAB.3.092001.

[6] S Aderhold, A Gössel, J Iversen, S Karstensen, D Kostin, G Kreps, A Matheisen, WD Möller, D Reschke, F Schlander, et al. Update on large grain cavities with 45 mv/m in a nine-cell cavity at desy, 2011.

[7] B. Hidding, G. Pretzler, J. B. Rosenzweig, T. Königstein, D. Schiller, and D. L. Bruhwiler. Ultracold electron bunch generation via plasma photocathode emission and acceleration in a beam-driven plasma blowout. *Phys. Rev. Lett.*, 108:035001, Jan 2012. doi: 10.1103/PhysRevLett.108.035001.

[8] G Wittig, O Karger, A Knetsch, Y Xi, A Deng, JB Rosenzweig, DL Bruhwiler, J Smith, GG Manahan, Z-M Sheng, et al. Optical plasma torch electron bunch generation in plasma wakefield accelerators. *Physical Review Special Topics-Accelerators and Beams*, 18(8):081304, 2015.

[9] G Wittig, O S Karger, A Knetsch, Y Xi, A Deng, J B Rosenzweig, D L Bruhwiler, J Smith, Z-M Sheng, D A Jaroszynski, et al. Electron beam manipulation, injection and acceleration in plasma wakefield accelerators by optically generated plasma density spikes. *Nuclear*

Instruments and Methods in Physics Research Section A: Accelerators, Spectrometers, Detectors and Associated Equipment, 2016.

[10] G. G. Manahan, A. Deng, O. Karger, Y. Xi, A. Knetsch, M. Litos, G. Wittig, T. Heinemann, J. Smith, Z. M. Sheng, D. A. Jaroszynski, G. Andonian, D. L. Bruhwiler, J. B. Rosenzweig, and B. Hidding. Hot spots and dark current in advanced plasma wakefield accelerators. *Phys. Rev. Accel. Beams*, 19:011303, Jan 2016. doi: 10.1103/PhysRevAccelBeams.19.011303.

[11] Gregor Hurtig. Free-electron-laser driven by high-brightness and low-emittance electron bunches. Master's thesis, University of Hamburg, 2017.

[12] Alexander Knetsch, Oliver Karger, Georg Wittig, Henning Groth, Yunfeng Xi, Aihua Deng, James Benjamin Rosenzweig, David Leslie Bruhwiler, Johnathan Smith, Dino Anthony Jaroszynski, et al. Downramp-assisted underdense photocathode electron bunch generation in plasma wakefield accelerators. *submitted*, 2017.

[13] J Clerk Maxwell. A dynamical theory of the electromagnetic field. *Philosophical transactions of the Royal Society of London*, 155:459–512, 1865.

[14] John David Jackson. *Classical Electrodynamics*. John Wiley & Sons, Inc., 3rd edition, 1998.

[15] Francsis F. Chen. *Introduction to Plasma Physics and Controlled Fusion*, volume 1. Plenum Press New York and London, 1974.

[16] Peter Mulser and Dieter Bauer. *High power laser-matter interaction*, volume 238. Springer Science & Business Media, 2010.

[17] LV Keldysh. Ionization in the field of a strong electromagnetic wave. *Sov. Phys. JETP*, 20 (5):1307–1314, 1965.

[18] AM Perelomov, VS Popov, and MV Terent'ev. Ionization of atoms in an alternating electric field. *Sov. Phys. JETP*, 23(5):924–934, 1966.

[19] Farhad HM Faisal. Multiple absorption of laser photons by atoms. *Journal of Physics B: Atomic and Molecular Physics*, 6(4):L89, 1973.

[20] Gennady L Yudin and Misha Yu Ivanov. Nonadiabatic tunnel ionization: Looking inside a laser cycle. *Physical Review A*, 64(1):013409, 2001.

[21] Vladimir Stepanovich Popov. Tunnel and multiphoton ionization of atoms and ions in a strong laser field (keldysh theory). *Physics-Uspekhi*, 47(9):855–885, 2004.

[22] M.V Ammosov, N.B Delone, and V. Krainov. Tunnel ionization of complex atoms and of atomic ions in an alternating electric field. *Sov. Phys. JETP*, 64:1191, 1986.

[23] E. E. Serebryannikov, A. J. Verhoef, A. Mitrofanov, A. Baltuška, and A. M. Zheltikov. Signatures of attosecond electron tunneling dynamics in the evolution of intense few-cycle light pulses. *Phys. Rev. A*, 80:053809, Nov 2009. doi: 10.1103/PhysRevA.80.053809.

[24] D Bauer. Ejection energy of photoelectrons in strong-field ionization. *Physical Review A*, 55(3):2180, 1997.

[25] Robin Shakeshaft, RM Potvliege, Martin Dörr, and WE Cooke. Multiphoton processes in an intense laser field. iv. the static-field limit. *Physical Review A*, 42(3):1656, 1990.

[26] David L Bruhwiler, DA Dimitrov, John R Cary, Eric Esarey, Wim Leemans, and Rodolfo E Giacone. Particle-in-cell simulations of tunneling ionization effects in plasma-based accelerators. *Physics of Plasmas (1994-present)*, 10(5):2022–2030, 2003.

[27] R.L. Kelly. *Atomic and ionic spectrum lines below 2000A: hydrogen through argon*. Oct 1982. doi: 10.2172/6644558.

[28] Yiming Zhang, Julian RG Evans, and Shoufeng Yang. Corrected values for boiling points and enthalpies of vaporization of elements in handbooks. *Journal of Chemical & Engineering Data*, 56(2):328–337, 2011.

[29] T Tajima and JM Dawson. Laser electron accelerator. *Physical Review Letters*, 43(4):267, 1979.

[30] W Horton and T Tajima. Pump depletion in the plasma-beat-wave accelerator. *Physical Review A*, 34(5):4110, 1986.

[31] C Joshi and Paul J Channell. The plasma beat wave accelerator-i experiments. In *AIP Conference Proceedings*, volume 91, pages 28–42. AIP, 1982.

[32] NE Andreev. Resonant excitation of wakefields by a laser pulse. *JETP lett*, 55(10), 1992.

[33] E. Esarey, C. B. Schroeder, and W. P. Leemans. Physics of laser-driven plasma-based electron accelerators. *Rev. Mod. Phys.*, 81:1229–1285, Aug 2009. doi: 10.1103/RevModPhys.81.1229.

[34] Patric Muggli, Alexander Pukhov, Edda Gschwendtner, Allen Caldwell, Matthew Wing, Konstantin Lotov, Olaf Reimann, Chiara Bracco, Ans Pardons, Roxana Tarkeshian, et al. Physics of the awake project. 2013.

[35] Sébastien Corde, E Adli, JM Allen, W An, CI Clarke, CE Clayton, JP Delahaye, J Frederico, S Gessner, SZ Green, et al. Multi-gigaelectronvolt acceleration of positrons in a self-loaded plasma wakefield. *Nature*, 524(7566):442–445, 2015.

[36] B Hidding, JB Rosenzweig, Y Xi, B O'Shea, G Andonian, D Schiller, S Barber, O Williams, G Pretzler, T Königstein, et al. Beyond injection: Trojan horse underdense photocathode plasma wakefield acceleration. In *Advanced Accelerator Concepts: 15th Advanced Accelerator Concepts Workshop*, volume 1507, pages 570–575. AIP Publishing, 2012.

[37] Pisin Chen. A possible final focusing mechanism for linear colliders. *Part. Accel*, 20(3-4): 171–182, 1987.

[38] W Lu, C Huang, MM Zhou, WB Mori, and T Katsouleas. Limits of linear plasma wakefield theory for electron or positron beams. *Physics of Plasmas*, 12(6):063101, 2005.

[39] W. K. H. Panofsky and W. A. Wenzel. Some considerations concerning the transverse deflection of charged particles in radio-frequency fields. *Review of Scientific Instruments*, 27 (11):967–967, 1956. doi: 10.1063/1.1715427. URL http://dx.doi.org/10.1063/1.1715427.

[40] J. B. Rosenzweig. *Fundamentals of Beam Physics*. Oxford: Oxford University Press, 2003.

[41] JB Rosenzweig, N Barov, MC Thompson, and RB Yoder. Energy loss of a high charge bunched electron beam in plasma: Simulations, scaling, and accelerating wakefields. *Physical Review Special Topics-Accelerators and Beams*, 7(6):061302, 2004.

[42] Nick Barov, JB Rosenzweig, MC Thompson, and RB Yoder. Energy loss of a high-charge bunched electron beam in plasma: Analysis. *Physical Review Special Topics-Accelerators and Beams*, 7(6):061301, 2004.

[43] W. Lu, C. Huang, M. Zhou, M. Tzoufras, F. S. Tsung, W. B. Mori, and T. Katsouleas. A nonlinear theory for multidimensional relativistic plasma wave wakefields. *Physics of Plasmas*, 13(5):056709+, 2006. doi: 10.1063/1.2203364.

[44] John M. Dawson. Particle simulation of plasmas. *Rev. Mod. Phys.*, 55:403–447, Apr 1983. doi: 10.1103/RevModPhys.55.403.

[45] Chet Nieter and John R Cary. Vorpal: a versatile plasma simulation code. *Journal of Computational Physics*, 196(2):448–473, 2004.

[46] Kane Yee. Numerical solution of initial boundary value problems involving maxwell's equations in isotropic media. *IEEE Transactions on Antennas and Propagation*, 14(3):302–307, May 1966. ISSN 0018-926X. doi: 10.1109/TAP.1966.1138693.

[47] The Vorpal and Composer Teams. Vsim in depth. Technical report, Tech-X, 2014.

[48] Jean-Pierre Berenger. A perfectly matched layer for the absorption of electromagnetic waves. *Journal of computational physics*, 114(2):185–200, 1994.

[49] Richard Courant, Kurt Friedrichs, and Hans Lewy. On the partial difference equations of mathematical physics. *IBM journal*, 11(2):215–234, 1967.

[50] Ian Blumenfeld, Christopher E Clayton, Franz-Josef Decker, Mark J Hogan, Chengkun Huang, Rasmus Ischebeck, Richard Iverson, Chandrashekhar Joshi, Thomas Katsouleas, Neil Kirby, et al. Energy doubling of 42 gev electrons in a metre-scale plasma wakefield accelerator. *Nature*, 445(7129):741–744, 2007.

[51] Helmut Wiedemann. *Particle Accelerator Physics*, volume 3. Springer-Verlag, 2007.

[52] Karl L Brown. A first-and second-order matrix theory for the design of beam transport systems and charged particle spectrometers. Technical report, SLAC, 1972.

[53] E.D Courant and H.S Snyder. Theory of the alternating-gradient synchrotron. *Annals of Physics*, 3(1):1 – 48, 1958. ISSN 0003-4916. doi: http://dx.doi.org/10.1016/0003-4916(58)90012-5.

[54] Klaus Floettmann. Some basic features of the beam emittance. *Phys. Rev. ST Accel. Beams*, 6:034202, Mar 2003. doi: 10.1103/PhysRevSTAB.6.034202.

[55] Simone Di Mitri. On the importance of electron beam brightness in high gain free electron lasers. In *Photonics*, volume 2, pages 317–341. Multidisciplinary Digital Publishing Institute, 2015.

[56] Wei Lu. *Nonlinear Plasma Wakefield Theory and Optimum Scaling for Laser Wakefield Accelerator (LWFA) in the Blowout Regime.* PhD thesis, UCLA, 2006.

[57] A. Martinez de la Ossa, C. Behrens, J. Grebenyuk, T. Mehrling, L. Schaper, and J. Osterhoff. High-quality electron beams from field-induced ionization injection in the strong blow-out regime of beam-driven plasma accelerators. *Nuclear Instruments and Methods in Physics Research Section A: Accelerators, Spectrometers, Detectors and Associated Equipment*, 740:231 – 235, 2014. ISSN 0168-9002. doi: http://dx.doi.org/10.1016/j.nima.2013.10.016. Proceedings of the first European Advanced Accelerator Concepts Workshop 2013.

[58] A. Pak, K. A. Marsh, S. F. Martins, W. Lu, W. B. Mori, and C. Joshi. Injection and trapping of tunnel-ionized electrons into laser-produced wakes. *Phys. Rev. Lett.*, 104:025003, Jan 2010. doi: 10.1103/PhysRevLett.104.025003.

[59] Arthur Pak. *Injection of Tunnel Ionized Electrons into Laser-Produced Wakes.* PhD thesis, University of California, 2010.

[60] KV Lotov. Blowout regimes of plasma wakefield acceleration. *Physical Review E*, 69(4):046405, 2004.

[61] S. G. Anderson, P. Musumeci, J. B. Rosenzweig, W. J. Brown, R. J. England, M. Ferrario, J. S. Jacob, M. C. Thompson, G. Travish, A. M. Tremaine, and R. Yoder. Velocity bunching of high-brightness electron beams. *Phys. Rev. ST Accel. Beams*, 8:014401, Jan 2005. doi: 10.1103/PhysRevSTAB.8.014401.

[62] L Serafini and M Ferrario. Velocity bunching in photo-injectors. In *AIP conference proceedings*, pages 87–106. IOP INSTITUTE OF PHYSICS PUBLISHING LTD, 2001.

[63] Pisin Chen, J. J. Su, J. M. Dawson, K. L. F. Bane, and P. B. Wilson. Energy transfer in the plasma wake-field accelerator. *Phys. Rev. Lett.*, 56:1252–1255, Mar 1986. doi: 10.1103/PhysRevLett.56.1252.

[64] KL Bane, Perry B Wilson, and T Weiland. Wake fields and wake field acceleration. In *AIP Conf. Proc.*, volume 127, pages 875–928, 1984.

[65] KA Marsh, CE Clayton, DK Johnson, C Huang, C Joshi, W Lu, WB Mori, M Zhou, CD Barnes, F-J Decker, et al. Beam matching to a plasma wake field accelerator using a ramped density profile at the plasma boundary. In *Particle Accelerator Conference, 2005. PAC 2005. Proceedings of the*, pages 2702–2704. IEEE, 2005.

[66] J Krall and G Joyce. Transverse equilibrium and stability of the primary beam in the plasma wake-field accelerator. *Physics of Plasmas*, 2(4):1326–1331, 1995.

[67] SZ Li, E Adli, RJ England, J Frederico, SJ Gessner, MJ Hogan, MD Litos, DR Walz, P Muggli, W An, et al. Head erosion with emittance growth in pwfa. In *AIP Conference Proceedings*, volume 1507, pages 582–587. AIP, 2012.

[68] Ian Blumenfeld, CE Clayton, FJ Decker, MJ Hogan, C Huang, R Ischebeck, RH Iverson, C Joshi, T Katsouleas, N Kirby, et al. Scaling of the longitudinal electric field and transformer ratio in a nonlinear plasma wakefield accelerator. *Physical Review Special Topics-Accelerators and Beams*, 13(11):111301, 2010.

[69] James Benjamine Rosenzweig, DB Cline, B Cole, H Figueroa, W Gai, R Konecny, J Norem, P Schoessow, and J Simpson. Experimental observation of plasma wake-field acceleration. *Physical review letters*, 61(1):98, 1988.

[70] H Figueroa, W Gai, R Konecny, J Norem, A Ruggiero, P Schoessow, and J Simpson. Direct measurement of beam-induced fields in accelerating structures. *Physical review letters*, 60(21):2144, 1988.

[71] CI Clarke, FJ Decker, RJ England, R Erikson, C Hast, MJ Hogan, SZ Li, M Litos, Y Nosochkov, J Seeman, et al. Facet: Slacs new user facility. *SLAC PUB*, 23:20, 2012.

[72] MJ Hogan, TO Raubenheimer, A Seryi, P Muggli, T Katsouleas, C Huang, W Lu, W An, KA Marsh, WB Mori, et al. Plasma wakefield acceleration experiments at facet. *New Journal of Physics*, 12(5):055030, 2010.

[73] M Litos, E Adli, W An, CI Clarke, CE Clayton, Sébastien Corde, JP Delahaye, RJ England, AS Fisher, J Frederico, et al. High-efficiency acceleration of an electron beam in a plasma wakefield accelerator. *Nature*, 515(7525):92–95, 2014.

[74] Spencer Gessner. *Demonstration of the Hollow channel Plasma Wakefield Accelerator*. PhD thesis, Stanford University, 2016.

[75] S. Bulanov, N. Naumova, F. Pegoraro, and J. Sakai. Particle injection into the wave acceleration phase due to nonlinear wake wave breaking. *Phys. Rev. E*, 58:R5257–R5260, Nov 1998. doi: 10.1103/PhysRevE.58.R5257.

[76] Hyyong Suk, Nick Barov, James Benjamine Rosenzweig, and E Esarey. Plasma electron trapping and acceleration in a plasma wake field using a density transition. *Physical review letters*, 86(6):1011, 2001.

[77] RJ England, JB Rosenzweig, and N Barov. Plasma electron fluid motion and wave breaking near a density transition. *Physical Review E*, 66(1):016501, 2002.

[78] A. Aschikhin, C. Behrens, S. Bohlen, J. Dale, N. Delbos, L. di Lucchio, E. Elsen, J.-H. Erbe, M. Felber, B. Foster, L. Goldberg, J. Grebenyuk, J.-N. Gruse, B. Hidding, Zhanghu Hu, S. Karstensen, A. Knetsch, O. Kononenko, V. Libov, K. Ludwig, A.R. Maier, A. Martinez de la Ossa, T. Mehrling, C.A.J. Palmer, F. Pannek, L. Schaper, H. Schlarb, B. Schmidt, S. Schreiber, J.-P. Schwinkendorf, H. Steel, M. Streeter, G. Tauscher, V. Wacker, S. Weichert, S. Wunderlich, J. Zemella, and J. Osterhoff. The {FLASHForward} facility at {DESY}. *Nuclear Instruments and Methods in Physics Research Section A: Accelerators, Spectrometers, Detectors and Associated Equipment*, 806:175 – 183, 2016. ISSN 0168-9002. doi: http://dx.doi.org/10.1016/j.nima.2015.10.005.

[79] J Grebenyuk, A Martinez de la Ossa, T Mehrling, and J Osterhoff. Beam-driven plasma-based acceleration of electrons with density down-ramp injection at flashforward. *Nuclear Instruments and Methods in Physics Research Section A: Accelerators, Spectrometers, Detectors and Associated Equipment*, 740:246–249, 2014.

[80] C. G. R. Geddes, K. Nakamura, G. R. Plateau, Cs. Toth, E. Cormier-Michel, E. Esarey, C. B. Schroeder, J. R. Cary, and W. P. Leemans. Plasma-density-gradient injection of low absolute-momentum-spread electron bunches. *Phys. Rev. Lett.*, 100:215004, May 2008. doi: 10.1103/PhysRevLett.100.215004.

[81] Karl Schmid, Alexander Buck, Christopher MS Sears, Julia M Mikhailova, Raphael Tautz, Daniel Herrmann, Michael Geissler, Ferenc Krausz, and Laszlo Veisz. Density-transition based electron injector for laser driven wakefield accelerators. *Physical Review Special Topics-Accelerators and Beams*, 13(9):091301, 2010.

[82] AJ Gonsalves, Kei Nakamura, Chen Lin, Dmitriy Panasenko, Satomi Shiraishi, Thomas Sokollik, Carlo Benedetti, CB Schroeder, CGR Geddes, Jeroen Van Tilborg, et al. Tunable laser plasma accelerator based on longitudinal density tailoring. *Nature Physics*, 7(11): 862–866, 2011.

[83] Alexander Buck, Johannes Wenz, Jiancai Xu, Konstantin Khrennikov, Karl Schmid, Matthias Heigoldt, Julia M Mikhailova, M Geissler, B Shen, Ferenc Krausz, et al. Shock-front injector for high-quality laser-plasma acceleration. *Physical review letters*, 110(18):185006, 2013.

[84] Karl Schmid, Alexander Buck, Christopher MS Sears, Julia M Mikhailova, Raphael Tautz, Daniel Herrmann, Michael Geissler, Ferenc Krausz, and Laszlo Veisz. Density-transition

based electron injector for laser driven wakefield accelerators. *Physical Review Special Topics-Accelerators and Beams*, 13(9):091301, 2010.

[85] Cédric Thaury, E Guillaume, Agustin Lifschitz, K Ta Phuoc, Martin Hansson, G Grittani, J Gautier, J-P Goddet, A Tafzi, Olle Lundh, et al. Shock assisted ionization injection in laser-plasma accelerators. *Scientific reports*, 5, 2015.

[86] N. Vafaei-Najafabadi, K. A. Marsh, C. E. Clayton, W. An, W. B. Mori, C. Joshi, W. Lu, E. Adli, S. Corde, M. Litos, S. Li, S. Gessner, J. Frederico, A. S. Fisher, Z. Wu, D. Walz, R. J. England, J. P. Delahaye, C. I. Clarke, M. J. Hogan, and P. Muggli. Beam loading by distributed injection of electrons in a plasma wakefield accelerator. *Phys. Rev. Lett.*, 112: 025001, Jan 2014. doi: 10.1103/PhysRevLett.112.025001.

[87] A. Martinez de la Ossa, J. Grebenyuk, T. Mehrling, L. Schaper, and J. Osterhoff. High-quality electron beams from beam-driven plasma accelerators by wakefield-induced ionization injection. *Phys. Rev. Lett.*, 111:245003, Dec 2013. doi: 10.1103/PhysRevLett.111.245003.

[88] F Li, JF Hua, XL Xu, CJ Zhang, LX Yan, YC Du, WH Huang, HB Chen, CX Tang, W Lu, et al. Generating high-brightness electron beams via ionization injection by transverse colliding lasers in a plasma-wakefield accelerator. *Physical review letters*, 111(1):015003, 2013.

[89] Y Wan, CJ Zhang, F Li, YP Wu, JF Hua, CH Pai, W Lu, YQ Gu, XL Xu, C Joshi, et al. Colliding ionization injection in a plasma wakefield accelerator. *Plasma Physics and Controlled Fusion*, 58(3):034015, 2016.

[90] CB Schroeder, J-L Vay, Eric Esarey, SS Bulanov, C Benedetti, L-L Yu, M Chen, CGR Geddes, and WP Leemans. Thermal emittance from ionization-induced trapping in plasma accelerators. *Physical Review Special Topics-Accelerators and Beams*, 17(10):101301, 2014.

[91] B Hidding, GG Manahan, O Karger, A Knetsch, G Wittig, DA Jaroszynski, ZM Sheng, Y Xi, A Deng, JB Rosenzweig, et al. Ultrahigh brightness bunches from hybrid plasma accelerators as drivers of 5th generation light sources. *Journal of Physics B: Atomic, Molecular and Optical Physics*, 47(23):234010, 2014.

[92] XL Xu, JF Hua, F Li, CJ Zhang, LX Yan, YC Du, WH Huang, HB Chen, CX Tang, W Lu, et al. Phase-space dynamics of ionization injection in plasma-based accelerators. *Physical review letters*, 112(3):035003, 2014.

[93] Michael E Durst, Guanghao Zhu, and Chris Xu. Simultaneous spatial and temporal focusing for axial scanning. *Optics express*, 14(25):12243–12254, 2006.

[94] Y Xi, B Hidding, D Bruhwiler, G Pretzler, and JB Rosenzweig. Hybrid modeling of relativistic underdense plasma photocathode injectors. *Physical Review Special Topics-Accelerators and Beams*, 16(3):031303, 2013.

[95] Wolfgang Demtroeder. *Experimentalphysik Elektrizität und Optik*. Springer-Verlag, 1 edition, 19999.

[96] K Kim, I Alexeev, and H Milchberg. Single-shot measurement of laser-induced double step ionization of helium. *Optics express*, 10(26):1563–1572, 2002.

[97] Jixiong Pu, Huihua Zhang, Shojiro Nemoto, Weibin Zhang, and Wenzhen Zhang. Annular-aperture diffractive axicons illuminated by gaussian beams. *Journal of Optics A: Pure and Applied Optics*, 1(6):730, 1999.

[98] JA Clarke, D Angal-Kalinin, N Bliss, R Buckley, S Buckley, R Cash, P Corlett, L Cowie, G Cox, GP Diakun, et al. Clara conceptual design report. *Journal of Instrumentation*, 9 (05):T05001, 2014.

[99] Vitaly Yakimenko, Yunhai Cai, Christine Clarke, Selina Green, Carsten Hast, Mark Hogan, Nate Lipkowitz, Nan Phinney, Greg White, and Gerald Yocky. Facet-ii accelerator research with beams of extreme intensities. In *7th International Particle Accelerator Conference (IPAC'16), Busan, Korea, May 8-13, 2016*, pages 1067–1070. JACOW, Geneva, Switzerland, 2016.

[100] Brookhaven National Laboratory. Upgrade and operate the accelerator test facility. Technical report, Brookhaven National Laboratory, 2014.

[101] G. Fubiani, E. Esarey, C. B. Schroeder, and W. P. Leemans. Improvement of electron beam quality in optical injection schemes using negative plasma density gradients. *Phys. Rev. E*, 73:026402, Feb 2006. doi: 10.1103/PhysRevE.73.026402.

[102] O Kononenko, NC Lopes, JM Cole, C Kamperidis, SPD Mangles, Z Najmudin, J Osterhoff, K Poder, D Rusby, DR Symes, et al. 2d hydrodynamic simulations of a variable length gas target for density down-ramp injection of electrons into a laser wakefield accelerator. *Nuclear Instruments and Methods in Physics Research Section A: Accelerators, Spectrometers, Detectors and Associated Equipment*, 2016.

[103] Lucas Schaper, Lars Goldberg, Tobias Kleinwächter, Jan-Patrick Schwinkendorf, and Jens Osterhoff. Longitudinal gas-density profilometry for plasma-wakefield acceleration targets. *Nuclear Instruments and Methods in Physics Research Section A: Accelerators, Spectrometers, Detectors and Associated Equipment*, 740:208–211, 2014.

[104] GG Manahan, AF Habib, P Scherkl, P Delinikolas, A Beaton, A Knetsch, O Karger, G Wittig, T Heinemann, ZM Sheng, et al. Single-stage plasma-based correlated energy spread compensation for ultrahigh 6d brightness electron beams. *Nature Communications*, 8: 15705, 2017.

[105] Michael Litos. private communication.

[106] Selina Li. Slac linac map. URL http://www.slac.stanford.edu/~selina/FACET/facet.html.

[107] R Koontz, R Miller, T McKinney, and A Wilmunder. Slac collider injector, rf drive synchronization and trigger electronics and 15 amp thermionic gun development. *IEEE Transactions on Nuclear Science*, 28(3):2213–2215, 1981.

[108] Nate Lipkowitz. private communication.

[109] R Akre, L Bentson, Paul Emma, and P Krejcik. Bunch length measurements using a transverse rf deflecting structure in the slac linac. In *Proc. EPAC 2002 Conference*, 2002.

[110] H Loos, T Borden, P Emma, J Frisch, and J Wu. Relative bunch length monitor for the linac coherent light source (lcls) using coherent edge radiation. In *Particle Accelerator Conference, 2007. PAC. IEEE*, pages 4189–4191. IEEE, 2007.

[111] N Lipkowitz, FJ Decker, J Sheppard, S Weathersby, U Wienands, M Woodley, and GS Yocky. Longitudinal beam tuning at facet. *TUPPC052, these proceedings*, 2012.

[112] MCI Optonix LLC. URL http://www.mcio.com/Products/drz-screens.aspx.

[113] pco.edge family user manual. URL https://www.pco.de/de/support/handbuecher/scmos-kameras/pcoedge-55/.

[114] National Institute of Standards and Technology. Stopping-power and range tables for electrons, Feb 2017. URL http://physics.nist.gov/PhysRefData/Star/Text/ESTAR.html.

[115] Navid Vafaei-Najafabadi. *Experimental Investigations of Beam Driven Plasma Wakefield Accelerators*. PhD thesis, UCLA, 2016.

[116] Erik Adli, SJ Gessner, Sébastien Corde, MJ Hogan, and HH Bjerke. Cherenkov light-based beam profiling for ultrarelativistic electron beams. *Nuclear Instruments and Methods in Physics Research Section A: Accelerators, Spectrometers, Detectors and Associated Equipment*, 783:35–42, 2015.

[117] S Z Green, E Adli, C I Clarke, S Corde, S A Edstrom, A S Fisher, J Frederico, J C Frisch, S Gessner, S Gilevich, P Hering, M J Hogan, R K Jobe, M Litos, J E May, D R Walz, V Yakimenko, C E Clayton, C Joshi, K A Marsh, N Vafaei-Najafabadi, and P Muggli. Laser ionized preformed plasma at facet. *Plasma Physics and Controlled Fusion*, 56(8):084011, 2014.

[118] Donna Strickland and Gerard Mourou. Compression of amplified chirped optical pulses. *Optics communications*, 55(6):447–449, 1985.

[119] *Manta G-125 Data sheet*. Allied Vision. URL https://www.alliedvision.com/en/products/cameras/detail/Manta/G-125.html.

[120] N Davidson, AA Friesem, and E Hasman. Holographic axilens: high resolution and long focal depth. *Optics letters*, 16(7):523–525, 1991.

[121] S. Gessner. github.com/aard-pwfa.

[122] Joseph W Goodman. *Introduction to Fourier optics*. Roberts and Company Publishers, 2005.

[123] SC Rae. Ionization-induced defocusing of intense laser pulses in high-pressure gases. *Optics communications*, 97(1-2):25–28, 1993.

[124] Roger M Wood. *Laser-induced damage of optical materials*. CRC Press, 2003.

[125] H. Varel, D. Ashkenasi, A. Rosenfeld, R. Herrmann, F. Noack, and E. E. B. Campbell. Laser-induced damage in sio2 and caf2 with picosecond and femtosecond laser pulses. *Applied Physics A*, 62(3):293–294, 1996. ISSN 1432-0630. doi: 10.1007/BF01575098.

[126] Anthony J Campillo. Small-scale self-focusing. In *Self-focusing: Past and Present*, pages 157–173. Springer, 2009.

[127] Rudolf Kingslake. *Applied optics and optical engineering*, volume 6. Elsevier, 2012.

[128] Robert Adair, L. L. Chase, and Stephen A. Payne. Nonlinear refractive index of optical crystals. *Phys. Rev. B*, 39:3337–3350, Feb 1989. doi: 10.1103/PhysRevB.39.3337.

[129] X. Yan, A. M. MacLeod, W. A. Gillespie, G. M. H. Knippels, D. Oepts, A. F. G. van der Meer, and W. Seidel. Subpicosecond electro-optic measurement of relativistic electron pulses. *Phys. Rev. Lett.*, 85:3404–3407, Oct 2000. doi: 10.1103/PhysRevLett.85.3404.

[130] Bernd Richard Steffen. *Electro-Optic Methods for Longitudinal Bunch Diagnostics at FLASH*. PhD thesis, University of Hamburg, 2007.

[131] Andover Corporation. Andover corporation catalogue: Optical coatings & filters. www.andovercorp.com, 2017.

[132] Wolfgang Lotz. An empirical formula for the electron-impact ionization cross-section. *Zeitschrift für Physik*, 206(2):205–211, 1967.

[133] BL Schram, FJ De Heer, MJ Van der Wiel, and J Kistemaker. Ionization cross sections for electrons (0.6–20 kev) in noble and diatomic gases. *Physica*, 31(1):94–112, 1965.

[134] Alexander Buck, K Zeil, Antonia Popp, Karl Schmid, A Jochmann, SD Kraft, B Hidding, T Kudyakov, CMS Sears, Laszlo Veisz, et al. Absolute charge calibration of scintillating screens for relativistic electron detection. *Review of Scientific Instruments*, 81(3):033301, 2010.

[135] E Adli, C A Lindstrom, J Allen, C I Clarke, J Frederico, S J Gessner, S Z Green, M J Hogan, M D Litos, B O'Shea, V Yakimenko, W An, C E Clayton, K A Marsh, W B Mori, C Joshi, N Vafaei Najafabadi, S Corde, and W Lu. Long range attraction of an ultrarelativistic electron beam by a column of neutral plasma. *New Journal of Physics*, 18(10):103013, 2016.

[136] Jens Osterhoff. private communication.

[137] Sebastian Schulz, Ivanka Grguraš, C Behrens, Hubertus Bromberger, JT Costello, MK Czwalinna, M Felber, MC Hoffmann, M Ilchen, HY Liu, et al. Femtosecond all-optical synchronization of an x-ray free-electron laser. *Nature communications*, 6, 2015.

[138] S. Kuschel, D. Hollatz, T. Heinemann, O. Karger, M. B. Schwab, D. Ullmann, A. Knetsch, A. Seidel, C. Rödel, M. Yeung, M. Leier, A. Blinne, H. Ding, T. Kurz, D. J. Corvan, A. Sävert, S. Karsch, M. C. Kaluza, B. Hidding, and M. Zepf. Demonstration of passive plasma lensing of a laser wakefield accelerated electron bunch. *Phys. Rev. Accel. Beams*, 19:071301, Jul 2016. doi: 10.1103/PhysRevAccelBeams.19.071301.

[139] Cédric Thaury, Emilien Guillaume, Andreas Döpp, Remi Lehe, Agustin Lifschitz, K Ta Phuoc, Julien Gautier, Jean-Philippe Goddet, Amar Tafzi, Alessandro Flacco, et al. Demonstration of relativistic electron beam focusing by a laser-plasma lens. *Nature communications*, 6, 2015.

[140] J Van Tilborg, S Steinke, CGR Geddes, NH Matlis, BH Shaw, AJ Gonsalves, JV Huijts, K Nakamura, J Daniels, CB Schroeder, et al. Active plasma lensing for relativistic laser-plasma-accelerated electron beams. *Physical review letters*, 115(18):184802, 2015.

[141] S Steinke, J Van Tilborg, C Benedetti, CGR Geddes, CB Schroeder, J Daniels, KK Swanson, AJ Gonsalves, K Nakamura, NH Matlis, et al. Multistage coupling of independent laser-plasma accelerators. *Nature*, 530(7589):190–193, 2016.

[142] Sven Steinke, Jeoren van Tilborg, Carlo Benedetti, CGR Geddes, J Daniels, KK Swanson, AJ Gonsalves, K Nakamura, BH Shaw, CB Schroeder, et al. Staging of laser-plasma accelerators. *Physics of Plasmas*, 23(5):056705, 2016.

[143] S. Chou, J. Xu, K. Khrennikov, D. E. Cardenas, J. Wenz, M. Heigoldt, L. Hofmann, L. Veisz, and S. Karsch. Collective deceleration of laser-driven electron bunches. *Phys. Rev. Lett.*, 117:144801, Sep 2016. doi: 10.1103/PhysRevLett.117.144801.

ACKNOWLEDGMENTS

Eine Promotion ist eine eigenständige wissenschaftliche Arbeit, jedoch wurde sie erst möglich durch die Menschen, die positiv auf mein Leben einwirken. Dieser Teil ist den Menschen gewidmet, die zum erfolgreichen Abschluss der Promotion beigetragen haben.

Ein besonderer Dank geht an Bernhard Hidding. Er hatte stets Vertrauen in meine Arbeit und gab mir Anleitung und die Freiheit, meine Fähigkeiten zu entwickeln und mein Verständnis für die wichtigen Details zu schulen. Als ich ihn kennenlernte, sagte er mir, ich könne mich darauf einstellen, viel zu reisen. Geblendet von diesen Aussichten war mir (und ihm vermutlich auch) nicht klar, welches Ausmaßdies einnehmen sollte, sodass ich 2015 mehr Zeit an Laboren und in Konferenzen ausserhalb von Hamburg verbracht habe, als zu Hause. Für diese Erfahrung bin ich dankbar und möchte sie, obwohl sie mit Anstrengungen verbunden war, in keinem Fall missen. Ich durfte verschiedenste Labore kennenlernen, jede mit ihren eigenen Randbedingungen und Arbeitsweisen. Dabei hatte ich das Glück mit einem ganz besonderem Team zusammen zu arbeiten. Kollegen und Freunde wie Oliver Karger, Thomas Heinemann, Paul Scherkl und Grace Manahan, die in der Lage sind, professionell an sich ständig ändernde Herausforderungen heranzugehen und dabei die für Experimente nötige Frustrationstoleranz mit Galgenhumor und stets guter Laune zu kombinieren. Georg Wittig, Fahim Habib und Gregor Hurtig, mit denen ich faszinierende Diskussionen häufig auch über Physik führen durfte.

Brian Foster möchte ich dafür danken, die Qualität in Inhalt und Sprache, die dieser Arbeit angemessen ist einzufordern und für die Geduld, die er dabei mit mir hatte.

Die experiemtellen Ergebnisse dieser Arbeit wären nicht möglich gewesen ohne das ausserordentliche Engagement der Kollegen, mit denen ich am FACET arbeiten durfte. Menschen wie Mike Litos, Mark Hogan, Vitaly Yakimenko, Christine Clarke, Selina Green, Brendan O'Shea, Spencer Gessner, Rafal Zgadzaj, Carl Lindstrøm und Navid Vafaei haben mit ihrer Hingebung, Motivation und Fachkenntnis das Labor erst zu dem besonderen Ort gemacht, der er ist. Marc Wenskat möchte ich herzlich für seine Hilfe in den letzten Wochen vor der Disputation danken.

Ganz besonders möchte ich auch meiner Familie, meinen Eltern und meiner Schwester, für ihre Unterstützung danken. Aus mir unerfindlichen Gründen haben sie nie an mir gezweifelt und waren mir stets ein Refugium, wenn die Aufgaben mich zu überwältigen drohten.
Muito obrigado à Theresa, o anjo que me acalmou e suportou nos meses passados.

DECLARATION

I hereby declare, on oath, that I have written the present dissertation by my own and have not used other than the acknowledged resources and aids.

Hamburg, 13.06.2017

Alexander Knetsch